Terrestrial Water Budgeting using Multi-source Remote Sensing Data in Poorly Gauged River Basins

Thesis submitted in partial fulfilment of the
requirements for the award of the degree of

Doctor of Philosophy

in

Civil Engineering

by

Suman Kumar Padhee

Under the supervision of

Prof. Subashisa Dutta

Department of Civil Engineering
Indian Institute of Technology Guwahati
Assam – 781039, INDIA
November, 2019

Dedicated to

My beloved Parents, My brother, And my wife

For their Love, Care and Support

ACKNOWLEDGEMENT

Though acknowledgement cannot be expressed in a piece of paper, here I get opportunity for expressing token of thanks to peoples who in a way helped and supported me during this tenure.

Foremost, I would like to express my sincere gratitude to my supervisor Prof. Subhasis Dutta, Department of Civil Engineering, Indian Institute of Technology Guwahati (IITG) for his scrupulous guidance, incessant motivation, valuable suggestions and continuous support throughout my doctoral study and research.

Besides my supervisor, I would like to extend my heartfelt thanks to the Chairman of my Doctoral Committee Prof. Arup Kumar Sarma, Department of Civil Engineering, IITG for useful discussions and contractive criticism throughout the pursuit of this study. I would also like to thank the members of my Doctoral Committee Dr. Bimlesh Kumar, Prof. Santosha K. Dwivedy, and Dr. N. Ganesh for their valuable suggestion provided at various stages of investigation and compilation of the thesis. Sincere thanks are due to Prof. Chitralekha Mahanta, Dean of Academic Affairs and Professor Gopal Das, Dean, Research and Development, IITG for providing me necessary facilities towards successful completion of this endeavor.

I am thankful to my lab mates especially Anjaneyulu, Satish, Ketan for long conceptual discussion. I will never forget the kind and mental support provided by my friends “Gaurav, Vishal, Shivam, Uttam, Ashutosh, Damodaran, Sudarsan, for sharing so many moments in my life for the deepest exchange of thoughts and for understanding me and my thesis worries. I do hereby acknowledge all the project staff especially Mr. Bazal Houque and students of Department of Civil Engineering who have helped immensely during my PhD work. Final appreciation to IIT Guwahati for providing the technology and environment to work.

Words are no eloquent to thanks other Professors for providing valuable suggestions and guidance in the research work.

Last but the most important, my heartiest appreciation is for the moral support given by my entire family, particularly my mother Mrs. Sarojinee Purohit, my father Mr. Sushanta Ku. Padhee, my wife Mrs. Sushreesmita Mishra and my brother Mr. Subham Ku. Padhee. There are

no words to thank you enough for the support and encouragement; I have been given throughout my life.

This list is obviously incomplete; I once again record my deepest gratitude to all those who have cooperated with me either directly or indirectly during my Doctoral study.

Date: 17-08-2020

Place: Guwahati

Suman Kumar Padhee

(Suman Kumar Padhee)

DECLARATION

I, **Suman Kumar Padhee**, author of the Ph. D. thesis "**Terrestrial Water Budgeting using Multi-source Remote Sensing Data in Poorly Gauged River Basins**" would like to certify that

- The work presented in this thesis is original research work carried out by me.
- The research work has not been submitted for any degree or diploma or any other qualification either in this institute or in any other university.
- Whenever I have used resources [theory, concepts, texts, data, graphs, figures or any other similar nature] from other sources, a due credit by citing in the text of the thesis is clearly made.
- The work presented here is free from plagiarism to the best of my knowledge, and I take the responsibility for any issues.
- I also affirm that thesis supervisor is not responsible for any possible instance of plagiarism within this submitted work.

Suman Kumar Padhee

Date:16-08-2020

Place: Guwahati

SUMAN KUMAR PADHEE

[136104017]

Indian Institute of Technology Guwahati

Department of Civil Engineering, Guwahati, Assam 781039

Subashisa Dutta, Ph. D.

Professor and Former Head

(subashisa@iitg.ac.in)

CERTIFICATE

This is to certify that thesis entitled "**Terrestrial Water Budgeting using Multi-source Remote Sensing Data in Poorly Gauged River Basins**" submitted by **Suman Kumar Padhee**, in partial fulfilment of the requirements for the award of degree of Doctor of Philosophy, to Indian Institute of Technology Guwahati, Assam, India, is a record of the bonafide research work carried out by him under my guidance and supervision at the Department of Civil Engineering, Indian Institute of Technology Guwahati, Assam, India. To the best of my knowledge, no part of the work reported in this thesis has been presented for the ward of any degree at any other institution.

Date: 16-8-2020

Place: Guwahati

Subashisa Dutta

ABSTRACT

Terrestrial energy and water budgeting needs consistent monitoring of its components and a good understanding and interpretation of hydrological processes. In poorly gauged river basins, water budgeting is a challenging task especially when the watersheds are located in complex and inaccessible mountains. The mountains are considered as the water towers of the world because it supplies water for mountain ecosystem by their watershed function. However, degradation of mountain ecosystem services has severe consequences for livelihoods and environments of downstream regions. The objective of this study was, therefore, to understand runoff generation process in hilly watersheds of Eastern Himalayan Mountains and simulate it by a developed region-specific rainfall-runoff model to understand the hydrological complexities.

The limitation of distributed gauging network is switched with satellite remote sensing for energy budgeting. However, two of the primary inputs of energy budgeting, viz. Normalized Difference Vegetation Index (NDVI) and Land Surface Temperature (LST) are inconsistently available due to frequent atmospheric obstruction of clouds. Consistent spatio-temporal availability of these two parameters is highly required to analyze spatial and temporal patterns of surface energy and water budget. Hence, new methodologies are developed to reconstruct the missing NDVI and LST time-series. 16-daily NDVI at 1 km is from Moderate Resolution Imaging Spectroradiometer (MODIS) is reconstructed by using a novel pre-filling method called as Moving Offset Method (MOM) prior to Harmonic analysis of time series (HANTS). It is found that using MOM minimizes the error while improving the seasonal trait of NDVI time-series for a variety of land use and land cover (LULC). 8-daily LST from MODIS is reconstructed by an innovative kernel based spatio-temporal data assimilation with LST from Global Land Data Assimilation System (GLDAS ≈25km). It shows the high accuracy of spatial pattern restoration in reconstructed time-series with *RMSE* = 0.6K and R^2=0.98 within the complex physiography. The high-quality reconstructed data are used in an energy balance model called 3T-model to produce consistent evapotranspiration (ET) time-series. Using ET with high resolution precipitation data (P) revealed the location of hotspots where annual ET exceeds annual P to be called as hydrological anomaly. High frequency of hydrological anomaly indicates hydrological resilience of those locations to P deficit per year. It is confirmed that hydrological resilient areas are mostly forest by hydrological efficiency test

for several LULC. Hence, it is hypothesized that the additional water required for ET in hydrological resilience could be in form of unknown preferential storage in forest areas. Also, analysis for 2nd order relationship of hydrological resilience with several selected physical parameters along the spatial extent shows that it is directly proportional to vegetation fraction and bedrock depth. Therefore, vegetation fraction and bedrock depth can be used as indicators for hydrological resilience. Lastly, a process-based hydrological model is developed for water balance in hilly watersheds having a fill and spill approach. It assumes a 3-layer soil matrix, macropores and perched aquifers having a theoretical hydraulic conductivity beyond the surface. The spatial characterization of macropore dynamics is done by using observed experimental values around the hillslopes of Eastern Himalaya. Calibration with a range of variable threshold and hydraulic conductivity values shows that best NSE value of 0.84 is found for threshold = 1cm ±25% and hydraulic conductivity value of a much higher order than theoretical value (≈10^4 times more). Moreover, the surface runoff generation ratio is found to be low but a good amount of runoff volume from base flow is observed. Both of these evidences point out towards possible existence of high velocity preferential flow which might be existing in Eastern Himalayan watersheds. The hydrological model is flexible and can be utilized in other regions, given the macropore properties are collected from field-site experiments.

Contents

List of Figures

List of Tables

Chapter 1

Introduction

1.1. Overview

The fresh water on earth is less than 2.5% of the total amount of terrestrial water, but it is essential for functional climate, environment, and society. The various sources of freshwater on land are in form of ice and snow, glaciers and ice caps, aquifers and soils, and surface water (rivers, reservoirs, wetlands, lakes and other inundated areas due to rainfall). Continuous exchange with the atmosphere makes terrestrial water as a part of the hydrological processes. Therefore, effective terrestrial water management in gauged and ungauged basins requires understanding of fundamental hydrological processes (Kult et al., 2014). Generally, it is easier to address the water quantity in gauged basins by using rainfall–runoff models calibrated to gauges (stream, rainfall, snowmelt, etc.) However, the need to focus on these issues over spatial domains with poorly maintained gauge observation networks are equally important (Hrachowitzet al., 2013). The challenge lies in the fact that some of the most hydrologically susceptible regions around the world have the worst maintained gauge network systems (Sivapalan et al., 2003). A number of approaches are preferred to address these issues including (a) extrapolation of basin response from gauged to ungauged basins, (b) application of remote sensing technology, (c) application of process-based hydrological models, (d) application of coupled meteorological–hydrological models, and (e) combination of some/all of the above. The status quo of these approaches is consistently in development and their usage is increasing to address regional and global hydrology research.

1.2. Terrestrial water budgeting

Understanding hydrological processes and forming water resources management strategies at global and regional scales require accurate estimates of water budgets (Kite and Droogers, 2000). The major water budget components include precipitation (P), evapotranspiration (ET), runoff (R), and combined storage in surface, sub-surface and groundwater as terrestrial water storage (TWS) (Fig. 1.1). On a global basis, ET accounts for about 70% of total P from the land surface (Rosenberg et al., 1983). About 80% of consumptive water use is lost in ET for global crop production (Liu et al., 2009), and can even range 80–90% in arid and semi-arid areas (Gowda et al., 2008). Analysis of trends for global runoff has been reported with increase of about 3 – 5 % (Probst and Tardy, 1987; Labat et al., 2004; Gedney et al., 2006). Both anthropogenic climate change and human water and land management are hypothesized to be responsible for the intensification in global runoff (Gudmundsson et al., 2019). The rivers are formed from accumulation of surface and sub-surface runoff. On average, the world's rivers carry about 30–40% of total P on land (Wang and Dickinson, 2012). The fundamental gears to study terrestrial water budgeting are flow, spatial distribution, storage and variability of freshwater on land (Kundzewicz et al., 2007).

It is highly required to monitor the dynamics in TWS for terrestrial water management. The hyper-resolution global hydrological models (GHM) in a variety in spatio-temporal domains are projected as a big leap towards expansion in understanding of hydrological processes (Bierkens et al., 2015). Due to this reason, many of the current researches related to terrestrial water budgeting are focused on the utilization of hydrological products from GHM. The current focus of majority of researchers for long-term water budgeting studies is on GHMs due to good temporal resolution. However, breakdown of reliant terrestrial water budget at finer resolutions might pose huge challenges due to increase in complexity

in hydrological responses (Beven and Cloke, 2012). GHMs would not be the preferred choice in basin-scale applications, due to the coarser resolution (Sood and Smakhtin, 2015). Hence, GHM are unsuitable for operative management in complex regions such as mountains. And therefore, it is a scientific requirement to understand the hydrological complexity at finer scales for advancements.

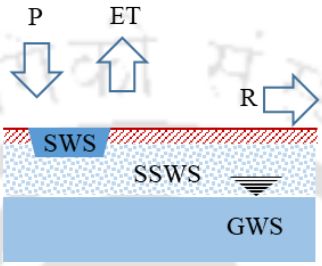

Figure 1.1. Terrestrial water budgeting components. P: precipitation, ET: evapotranspiration, R: runoff, SWS: surface water storage, SSWS: sub-surface water storage, GWS: ground water storage, SWS + SSWS + GWS = TWS: total water storage.

1.3. Remote Sensing Applications in Terrestrial water Budgeting

When it comes to poorly gauged basins, the unavailability of hydro-meteorological records is a big challenge in terrestrial water budgeting. Remote Sensing (RS) techniques are superior in covering spatial heterogeneity of water budgeting components in poorly gauged basins as compared to traditional computations by gauging. These techniques play important role in quantification of spatial dynamics of water loss generating ET (Cleugh et al., 2007). However, consistent spatio-temporal availability of ET at high resolution is still a major problem due to frequent obstruction by seasonal clouds. It is because most of the satellite-derived parameters to estimate ET are within visible and thermal range of electromagnetic spectrum (Jiménez-Muñoz and Sobrino, 2003; Kobayashi and Dye, 2005). The most important meteorological input for forcing and calibrating hydrological models is P. Conversely from ET, the estimation of P from a variety of satellite sensors work in the microwave range of electromagnetic spectrum (Zeng et al., 2018). Due to this reason, there

is very little data unavailability scenario since the launch of first precipitation oriented joint international mission, Tropical Rainfall Measuring Mission (TRMM) in 1998. Some of the popular microwave sensors used today for estimation of P are multiple pass microwave (PMW), the Microwave Imager (TMI), Special Sensor Microwave Imager (SSM/I), Advanced Microwave Scanning Radiometer-Earth Observing System (AMSR-E), and Advanced Microwave sounding Unit-B (AMSU-B). However, long-term P is obtained as climate datasets by reanalysis. Many times, the climate datasets are validated with satellite- and/or gauge-observed P estimations (Sun et al., 2017). However, the best spatial resolution is still not more than 0.1°. The runoff is computed by physical-based or atmospheric-coupled hydrological models by using satellite-based inputs and metadata at regional and global scales (Hassan, 2016; Rafiei Emam et al., 2017; Scanlon et al., 2019). The incoming and outgoing runoff flux at surface, also called as discharge, are important for monitoring the changes in terrestrial surface storage. For sub-surface, the same models are utilized as per the depth schemes provided within. Nevertheless, the biggest contribution of RS technology to terrestrial water budgeting is satellite-gravimetry. The first generation of satellite gravity missions, i.e., CHAMP (Challenging Minisatellite Payload; Reigber et al., 2002), GRACE (Gravity Recovery and Climate Experiment; Tapley et al., 2004), and GOCE (Gravity Field and Steady-State Ocean Circulation Explorer; Drinkwater et al., 2003), has transformed the knowledge of the changes in Earth's gravity field. These changes are related to geophysical processes of mass redistribution on Earth. The most frequent mass redistribution on Earth is due to changes in terrestrial water storage which GRACE has effectively utilized. The RS techniques has revolutionized the terrestrial water budgeting studies in last two decades.

1.4. Complex River Basins

There can be many categorizations of complexity in river basins, but the most important category is as per the physiography. A river basin having large physiographic variation might contain variation in ecology, land use and land cover (LULC), climate etc. and could create difficulties in hydrological modeling. The example of a river basin with complex physiography, Brahmaputra River basin including Eastern Himalayan Mountains in the Northeast Indian region, is presented in Fig. 1.2 (selected as the study area in this research). Various LULC in the ecoregions of the study area are shown in Table 1.1.

Mountainous regions are the main hydrological triggers of the water cycle (de Jong et al., 2005). Mountains and hills are crucial in the hydrological studies because these regions serve as origination place for several rivers of large basins (Merz et al., 2006; Kouraev et al., 2004; Sharma et al., 2017; Molina-Carpio et al., 2017). These regions are crucial being the source of snow and/or rainwater supply to the lowlands (Fayad et al., 2017). Many previous studies have found that the spatial variability of slope gradient, aspect, curvature, slope position and relative elevation, soil properties and solar radiation can influence the distribution of sub-surface water storage (Reynolds, 1970; Moore et al., 1988; Western et al., 1999). The topography in mountainous regions is mostly heterogeneous which affects the variability in these elements. Also, heterogeneity in antecedent soil condition and solar radiation are essential elements known to affect the ecosystem (Gates, 1980a; Wei et al., 2019). The physiography is known to affect important meteorological and land surface variables required for energy and water budgeting. Fig. 1.3 shows the variability in precipitation, land surface temperature, vegetation fraction, and percentage of specific land use according to variation of elevation. Together these combinations create hydrological complexity to influence the hydrological response of an area which might not be addressed

by GHMs. Therefore, accounting of hydrological response by including heterogeneity in complex river basins is important for estimating appropriate terrestrial water components.

1.5. Hydrological Modeling

The difficulty in energy and water budgeting in a complex river basin is due to transition caused by physiographic change. The unsuitability of GHMs in complex scenario is further increased with unavailability of observed data (Sood and Smakhtin, 2015). Therefore, estimation of runoff in ungauged hilly watersheds is a challenging task due to spatial and temporal variations of these elements. In contrary, the hydrological processes in hilly watersheds can be well explained by physical-based concepts in hillslope hydrology which is a research realm in itself.

Usually, terrestrial water budgeting is approached in a perspective with water entering the system as precipitation and leave by evapotranspiration and runoff with changes in terrestrial storage to monitor. However, this model is often inadequate in complex river basin system with hilly watersheds. It is because detailed effects of vegetation and subsurface properties is neglected in generation of overland flow which can change the spatio-temporal dynamics of water budgeting components. In previous research works, these functions were studied independently and recently response to their combination became a research priority (Berry et al., 2005). However, the upscaling process for basin scale studies dilutes the understanding of hillslope dominating hydrological processes. Therefore, the models like SWAT are more popular in application due to numerical-based methods with a scheme of calibration and validation at the outlet. The disadvantage with such models is that they are unable represent the near-real physical process (Grizzetti et al., 2005) which is quite important in terrestrial water budgeting.

Alternately, it is a general practice to develop a hydrological model by the understanding of hydrological processes and dynamics and scale-up to the watershed level in physical-based hydrological modeling (Dutta and Zade, 2003). There are evidences of a threshold-based runoff delay in hilly watersheds of humid tropical or sub-tropical regions (Williams et al., 2002). Such a threshold mechanism of runoff generation is often closely related to preferential flow characteristics associated with different land covers (Tromp-van Meerveld and McDonnell, 2005; Graham et al., 2010; Graham and McDonnell, 2010; Penna et al., 2011). The preferential flow is caused by active soil macropores depending on land covers (Shougrakpam et al., 2010; Sharma et al., 2013). Moreover, recent research has also indicated that there could be separate storage system for natural vegetation and streams (Berry et al., 2018; Sprenger et al., 2019). Interpretation of hillslope concepts to understand the spatial hydrological responses and precisely integrating to upscale at basin scale can be a great contribution to terrestrial water budgeting in hilly watersheds of complex river basin systems.

Table 1.1. Major LULC classes in different ecological regions in the study area.

Ecological Region	MODIS LULC	Percentage of area in ecoregion (%)
Himalayas	Mixed forest	36
	Evergreen broadleaf forest	14
	Grassland	08
Assam Plains	Agriculture	30
	Cropland and natural vegetation	18
	Woody savannas	08
Khasi and Garo hills	Evergreen broadleaf forest	47
	Woody savannas	15
	Mixed forest	06

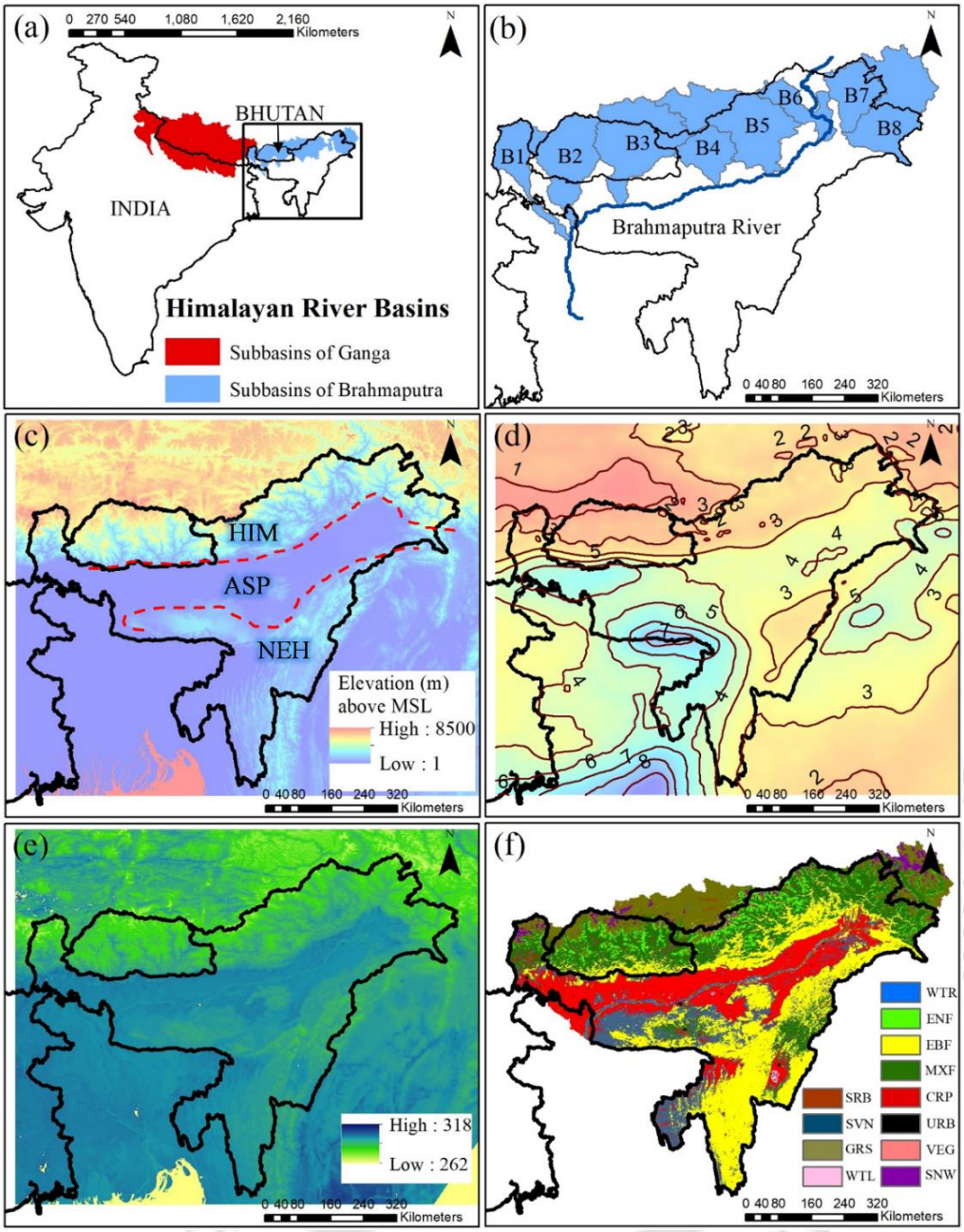

Figure 1.2. (a) Geographical Location of upper sub-basins of the Brahmaputra River. (b) Upper sub-basins of Brahmaputra River (B1-Teesta, B2-Gangadhar, B3-Manas, B4-Kameng, B5-Subansiri, B6-Siyom, B7-Dibang and B8-Lohit). (c) Physiographic divisions of Northeast Indian region (HIM-Eastern Himalaya, ASP-Assam Plains, NEH-Northeast Hills). (d) Mean annual daily rainfall (mm/day) in Northeast Indian region (Source: GsMap daily rainfall by JAXA). (e) Mean annual daily temperature at 1030 IST in Northeast Indian region (Source: MODIS Terra). (f) Land use and land cover in Northeast Indian region (WTR-water, ENF-evergreen needleleaf forest, EBF-evergreen broadleaf forest, MXF-mixed forest, CRP-cropland, URB-urban area, VEG-natural vegetation, SNW-snow, SRB-shrubland, SVN-savanna, GRS-grassland, WTL-wetland).

1.6. Objectives

The main objectives of the present research are:

1. To derive spatio-temporally consistent parameters in data deficient scenario for energy budgeting at moderate spatial resolution of 1 km.
2. To estimate the annual ET flux at monthly scale using moderate spatial resolution multi-sourced satellite data in the 3T-model.
3. To analyse the annual fluctuations in water loss/gain components for natural and anthropogenic vegetation cover in the study area.
4. To develop a hydrological model for water balance in hilly watersheds and derive surface and sub-surface water storage.

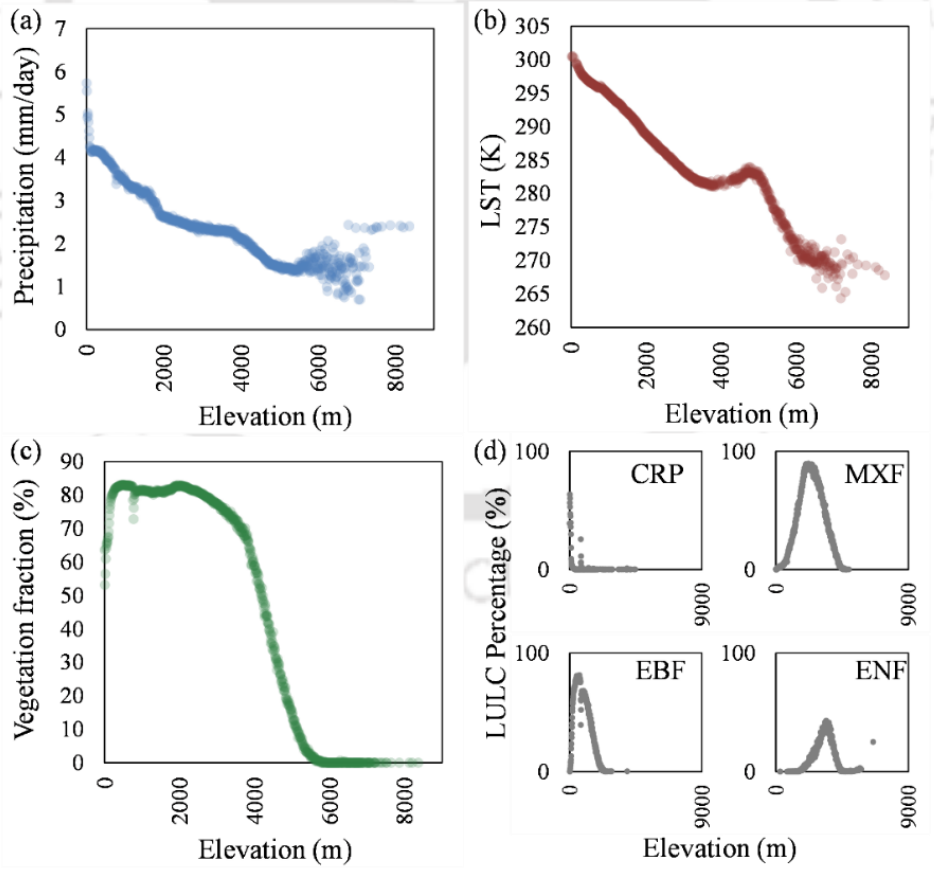

Figure 1.3. Variation of (a) mean annual daily precipitation, (b) median land surface temperature, (c) median vegetation fraction, (d) percentage area of specific land use and land cover in the study area with elevation.

1.7. Organization of Thesis

The thesis of the present study comprises of seven chapters. Chapter 1 contains a brief overview of the problem and the specific objectives taken for the study. Chapter 2 focuses towards understanding the relevant literatures to study the progress in data reconstruction, energy budgeting and process-based concepts on hillslope hydrology. Chapter 3 mainly documents the details of reconstruction of time-series of land surface vegetation which is an essential variable in energy and water budgeting. It discusses about a novel technique used to overcome large data deficiency. Chapter 4 describes the details of another essential variable in energy and water balance, the land surface temperature. The chapter summarizes use of an innovative spatio-temporal assimilation approach which can overcome the data deficiency in complex physiography. Chapter 5 outlines the other essential data preparation, energy budgeting, surface water budgeting and several important observations in the Eastern Himalayan watersheds. The conclusive evidences are used for building region specific hydrological knowledge. Data reconstructed from the previous chapters have been used for energy and water budgeting which makes it possible to observe consistent surface water availability in order to conclude. Chapter 6 deals with development of a process-based hydrological by using conclusive evidences in the previous chapter and literature-based concepts and observations. It summarizes the base of the model, its calibration scheme, simulation projections and the conclusions of observations. It also demonstrates the model simulation in one of the pilot watersheds of Eastern Himalaya. Chapter 7 is the final chapter which highlights the conclusions arrived at and also summarizes the research work.

Chapter 2

Literature Review

2.1. Introduction

Monitoring the surface water availability is the beginning of effective management of terrestrial water. It requires consistency of hydro-meteorological and surface condition data with good knowledge of hydrological processes to derive water availability. But, majority of river basins in the world are ungauged or poorly gauged which makes water budgeting a challenging task. The challenge is raised with increase in physiographic complexity of watersheds like in Himalayan region. Satellite remote sensing operational in visible range of electromagnetic spectrum are used to monitor many land surface variables including those which influence hydrological processes. The land surface vegetation and temperature are two of the essential variables used in estimating water loss or evapotranspiration (ET). Satellite technology have limitations in acquisition of these variables during clouded situation. The Eastern Himalayan watersheds located in Northeast region of India are one of the frequently clouded regions in the world. There are several methods to recover the missing time-series data, however these methods are problem and location specific. Likewise, there are numerous hydrological models with specific objectives. The selection of a proper rainfall-runoff scheme can be key to impact the initial process of water budgeting. A detailed review is listed below covering all these aspects with idea of isolated, poorly gauged and complex hilly watersheds of Eastern Himalaya.

2.2. Evapotranspiration and Energy Balance Models

ET is one of the continuously loss generating components in water budget which is driven by energy flux. The variable ET is the combination of soil evaporation (Es) and vegetation transpiration (Tc). It is an essential component for energy and mass balance in global ecosystems and define the environmental characteristics (Nemani et al., 2002). Its persistency for a prolonged time without Precipitation (P) can cause water deficit in many resources. So, the spatial impact of ET on other water resource components, like surface and sub-surface storage, is essential to monitor change in those components (Batiaanssen et al., 1998a; 1998b). Such crucial proportion of ET in natural processes and applications defines the importance of ET estimation.

The methods to estimate ET can be categorized into three groups: energy balance, micrometeorological and plant physiology methods. Since micrometeorological and plant physiology methods face practical difficulty, suitability of these methods is limited to micro scale homogenous surfaces (Mu et al., 2007). On the other hand, energy balance methods are supportive to utilization of RS data which is advantageous in coverage of heterogeneity over large extents. Hence, there has been a global increase in use of energy balance methods in hydrological studies with time thereby forming several energy balance models.

Initially, ET was usually estimated by water balancing which is assisted using weighing lysimeters. Qiu et al. (1996; 1998) proposed an algorithm, in which Es is estimated by including the temperature of a reference dry soil surface using input variables as temperature, net radiation, and soil heat flux. Its comparison with Es calculated from an installed lysimeter showed high R^2 value of 0.94. This was one of the first experiments in the development of energy balance methods which had the capability to overcome many shortcomings of traditional ET estimation.

Surface Energy Balance Algorithm for Land (SEBAL) developed by Bastiaanssen et al. (1998a; 1998b) is a popular energy balance model. It is basically an empirical model with requirements of RS inputs assisted by field information on short wave atmospheric transmittance, surface temperature and vegetation height. Generally, the empirical relationships of SEBAL are region- and time-dependent which creates difficulty in its usage. Bastiaanssen et al. (1998b) verified the surface fluxes obtained from SEBAL with data available from the large-scale field experiments viz. EFEDA (Spain), HAPEX-Sahel (Niger) and HEIFE (China). The differences were found within the range of instrumental inaccuracies in 85% of the cases. Li et al. (2005) formulated another energy balance model, 'Two-source energy balance model' for parameterizing soil and canopy energy exchanges. It is based on a 'Two resistance network' in which the interaction between the soil and canopy fluxes are rejected by parallel resistance and series resistance provides interaction via the computation of a within-air canopy temperature. Two-source energy balance model was demonstrated by utilization of surface temperature from Landsat TM/ETM scenes. The meteorological data is fed by tower-based readings in this model. The reliability of this model is validated for agriculture cover and soil moisture conditions meant for a narrow range of vegetation cover fraction. Cleugh et al. (2007) evaluated aerodynamic resistance–surface energy balance model and Penman–Monteith (P–M) equation to estimate land surface evaporation at 16-day intervals using MODIS data and surface meteorology as inputs. It was found that P–M equation are superior in estimating ET than aerodynamic resistance–surface energy balance model in a variety of ecosystems. However, the impact of energy could not be neglected due to which Mu et al. (2007) revised the RS based P–M algorithm (RS-PM) as an energy balance model for global scale. The algorithm considers both the surface energy partitioning process and environmental constraints on ET. The basic inputs for the algorithm are ground-based meteorological observations and RS data.

Most of these models are suitable for applications in limited areas due to requirement of huge network of ground-based meteorological data. Concerning on poorly gauged basins, these models can fail in practical use because of either rationality of assumptions or unavailability of other supporting data. These limitations make estimation of ET in poorly gauged basins as one of the most challenging subjects. Luo et al. (2012) conducted a study using land surface energy balance theory and concepts of Qiu et al. (1996; 1998) to develop a new energy balance model, 'Three temperature model (3T model)'. This model estimates Es for the bare soil, Ts for vegetation land, and ET for mixed regions. The requirement of inputs are RS-based variables and meteorological data is limited to air temperature only. The maximum and minimum absolute errors were found as 1.70 mm/d and 0.05 mm/d respectively. Also, the spatial distribution of surface ET was different in the different reaches in accordance with vegetation conditions. Following this work, Tian et al. (2013) conducted an extended case study in Heihe River Basin of northwestern China where ET was estimated by 3T model using MODIS products. The maximum, minimum and mean absolute error were found to be 1.28 mm/d, 0.02 mm/d, and 0.08 mm/d respectively. The 3T model can satisfy regional research requirement for hydrological studies at large scales. However, any energy balance model can face difficulties in time-series applications due to involvement of RS-based inputs operating in visible and thermal range of electromagnetic spectrum (Jiménez-Muñoz and Sobrino, 2003; Kobayashi and Dye, 2005).

2.3. Moderate resolution imaging spectroradiometer (MODIS)

MODIS platform has turned out to be one of the most general sources for satellite-derived land surface variables (Wan, 2014). This is because of its optimal spatial and temporal resolution in earth observation. It has been in operation since year 2000 to present. Characteristically, MODIS satellites are near-polar orbiting due to which it has high

temporal resolution. However, the MODIS Terra and Aqua satellites together acquire the images of a place for only four times a day (two ascending and two descending). Since, MODIS sensors operate at visible electromagnetic spectrum, the instantaneous acquisition is affected by presence of seasonal/non-seasonal opaque atmospheric elements like cloud, fog, aerosol etc. (Neteler et al., 2010; Jia et al., 2011) thereby creating spatio-temporal inconsistency. Therefore, several researchers around the world are engaged in development of reconstruction methods to solve the problem of spatio-temporal inconsistency in land surface variables.

2.4. Land surface Vegetation

Normalized difference vegetation index (NDVI) is a land surface variable which is computed as the normalized ratio of the difference in surface reflectance in near-infrared (ρ_{NIR}) and red (ρ_{Red}) spectrum range to their sum (Tucker, 1979) as shown in Eq.2.1.

$$\text{NDVI} = \frac{\rho_{\text{NIR}} - \rho_{\text{Red}}}{\rho_{\text{NIR}} + \rho_{\text{Red}}} \tag{2.1}$$

It has essential applications in modern terrestrial studies due to its proficiency to reveal vegetation strength. Its application extends to fields like hydrology (Ahmed et al., 2017; Liu et al., 2015); hydrometeorology (Xiong and Qiu, 2011; Carter et al., 2018; Joiner et al., 2018); agriculture (Panda, Ames and Panigrahi, 2010; Glennie and Anyamba, 2018; Padhee et al., 2017), disaster management (Lin et al., 2004; Gandhi et al., 2015), and climate change (Kundu et al., 2018; Szabó et al., 2018). It is often used in energy budgeting (Liang et al., 1994; Bastiaanssen et al., 1998a; 1998b; Tian et al., 2013; Mutti et al., 2019) and the runoff response modeling (Jin et al., 2008; Wenjuan and Hou, 2019).

Spatio-temporal consistency of high-quality NDVI is a necessity for time-series based studies. But the reflectance channels used in computation of NDVI are affected by opaque

atmospheric components thereby creating spatio-temporal inconsistency (Carreiras et al., 2003; Kobayashi and Dye, 2005). Justice et al. (1985) identified that it occurs as noise due to compositing different channels in different atmospheric conditions. Holben (1986) suggested suppressing defective NDVI values in the time-series by maximum-value composite (MVC), where NDVI was calculated from spectral channels with best pixel value within a period. Some of the popular MVC NDVI products used today are from NOAA/AVHRR, SPOT/VEGETATION, and TERRA or AQUA/MODIS. MVC NDVI products also reduce data gaps caused by cloud-contaminated pixels in NDVI time-series besides just suppressing the noise (Jia et al., 2011). However, even MVC NDVI products are reported with noise and data gaps in the time-series (Jönsson and Eklundh, 2002; Chen et al., 2004; Ma and Veroustraete, 2006; Ren et al., 2008; Geng et al., 2014). Subsequently, several methods have been developed to fulfill NDVI consistency (Geng et al., 2016).

The popular reconstruction techniques used after MVC procedure can be categorized into five groups according to their application methods: (1) Running filter techniques – Savitzky-Golay filtering (Savitzky and Golay, 1964; Chen et al., 2004), the mean value iteration filter (Ma and Veroustraete, 2006), the changing-weight filter (Zhu et al., 2012); (2) Function fitting techniques – Fast Fourier transform and harmonic analysis of time-series (FFT/HANTS) (Menenti et al., 1993; Verhoef, 1996; Roerink et al., 2000), the double logistic function fitting (Fischer, 1994; Beck et al., 2006), the temporal window operation (Park et al., 1999), the asymmetric Gaussian function fitting (Jönsson and Eklundh, 2002); (3) Thresholding techniques – the Best index slope extraction (Viovy et al., 1992), and the modified BISE (Lovell et al., 2007); (4) Hybrid techniques – data assimilation (Gu et al., 2009), iterative interpolation for data reconstruction (Julien and Sobrino, 2010); and (5) Other techniques – wavelet transform (Lu et al., 2007), and the Whittaker smoother (Atzberger and Eilers, 2011a; 2011b). Nevertheless, there is still NDVI data deficiency in

many regions due to numerous reasons which limits the studies focused on NDVI time-series applications.

2.5. Land Surface Temperature

Land surface temperature (LST) is the radiative skin temperature of the earth's surface. It is an influential parameter in interactions between land and atmosphere. It has enormous applications in the fields of climate change (Houghton et al., 2001), land cover changes (Tran et al., 2017), crop management (Shen et al., 2018), water management (Muro et al., 2018; Kitsara et al., 2018) forest fire management (Chuvieco et al., 2004) etc. including energy balance models. Satellite-based LST are affected with similar problems to that of NDVI (Neteler et al., 2010). Due to use of LST in energy balance models, consistent spatio-temporal LST availability is anticipated to increase reliability in spatio-temporal information in energy and water flux.

In the recent past, there has been numerous attempts to fill spatio-temporal data gaps by recovering the missing LST. Generally, statistical methods are used for this purpose and broadly categorized into three groups by the utilization of data in dimensions viz. spatial, temporal, and spatio-temporal methods.(Kang et al., 2018) In spatial methods, missing LST is predicted by using spatial relationship (linear/polynomial) between available LST and ancillary data (used as covariate). The covariate/covariates is/are selected based on sole/combined influence on the spatial dynamics of LST (Neteler et al., 2010; Fan et al., 2014; Ke et al., 2013). However, the complexity in relationship between covariates and LST increases with diverse physiography. Temporal methods employ temporal models like harmonic analysis of time-series (HANTS) algorithm and Savitzky-Golay filter (Xu and Shen, 2013) to fit available time-series of LST at any location and recover the missing values. But these models are designed to smoothen time-series irrespective of time due to

which the effect of daily variation is lost (Kang et al., 2018). It limits them to be used only for average predictions at large temporal intervals. Spatio-temporal methods fundamentally uses regression relationship with most similar pixels within the confidence of smallest possible distance (Yu et al., 2015; Chao Zeng et al., 2015; Sun et al., 2017). These methods could be restricted by lack of data due to variable factors. Zhou et al. (2017) used DINEOF method to reconstruct land surface temperature in Tibetan region. But, studies on its application for diversified physiography remains limited. Spatio-temporal inconsistency of LST have led researchers to develop multi-temporal approaches and increase the data consistency. Kou et al. (2016) successfully recovered LST at high spatial resolution from MODIS sensor at nighttime by utilizing microwave temperature brightness at coarse spatial resolution from AMSR-E sensor as a covariate series. However, this approach works for two data series having same acquisition time which is practically difficult to attain. Kang et al. (2018) used LST unaffected by clouds from MODIS Terra and Aqua platforms to reconstruct affected LST. The multi-temporal approaches have grown as promising methods to increase spatio-temporal consistency in LST.

2.6. Irradiance, albedo, emissivity and surface response

Incoming flux of solar radiation or irradiance (R_i) is one of the principal variables in energy budgeting. It drives the energy exchange process between various components on the Earth's surface and influences the naturally occurring environmental cycles (Danehy et al., 2005; Shafer et al., 2005). The sun produces shortwave radiation which enters from the top of the Earth's atmosphere and reaches to the Earth's surface after transmission though it. During this transmission process, a part of the shortwave radiation reaches to the surface either directly or indirectly (via. incidence, reflection, scattering) as incoming shortwave radiation (SW_{in}). The remaining part is absorbed by various atmospheric elements and later

emitted towards the Earth's surface as incoming longwave radiation (LW_{in}). Eq.2.2 depicts that R_{in} is composed of SW_{in} and LW_{in}.

$$R_i = SW_{in} + LW_{in} \tag{2.2}$$

After reaching to the Earth's surface, some amount of SW_{in} is reflected from the surface while remaining is absorbed. This proportion of the SW_{in} reflected by the Earth's surface as outgoing shortwave radiation (SW_{out}) is called Albedo (α) and it is shown in Eq.2.3. The remaining shortwave radiation (SW_{net}) as shown in Eq.2.4, contributes to conversion of water to vapour form. The Earth's surface also absorbs LW_{in} which is later emitted as outgoing longwave radiation (LW_{out}) in a proportion represented by emissivity (ε). The water to vapour conversion process is also assisted by remaining longwave radiation (LW_{net}) in a similar fashion as shown in Eq.2.5. Finally, total remaining radiation (R_{net}) as combination of SW_{net} and LW_{net} is used to calculate the energy (Eq.2.6). This energy is required for the process of conversion of water to vapour as ET as shown in Eq.2.6 and Eq.2.7 (Swift and Knoerr, 1973; Gates, 1980b; Brubaker et al., 1996; Katul et al., 2012; Verdhen et al., 2014; Vourlitis et al., 2015).

$$\alpha = \frac{SW_{out}}{SW_{in}} \tag{2.3}$$

$$SW_{net} = SW_{in} - SW_{out} \tag{2.4}$$

$$LW_{net} = LW_{in} - LW_{out} \tag{2.5}$$

$$R_{net} = SW_{net} + LW_{net} \tag{2.6}$$

$$R_{net} = LE+G+H \tag{2.7}$$

Since, the net radiation is calculated from α and ε, it makes these as the decisive components for energy budgeting techniques. There are many studies to use ε in energy balance out of which the most accepted form for water balance is using a combination of ε for both atmosphere and surface to define LW_{out} as their function (Swinbank, 1963; Brutsaert, 1975;

Crawford et al., 1999; Niemelä et al., 2001). Currently, α and ε are calculated as functions of reflectance in shortwave and longwave ranges by using RS technology (Xiong and Qiu, 2011; Tian et al., 2013).

The most accurate source of collecting R_i are conventional ground-based instruments in meteorological and climatological stations. However, it is difficult to obtain the same for large spatial extent, especially in the mountainous regions. Many times, it is dealt by interpolation techniques for small regional extents but requires high number of recording stations as demonstrated by Jeong et al. (2017) and Rodríguez-Amigo et al. (2017). Other alternatives include empirical correlations using different meteorological, astronomical and geometrical factors **(**Besharat et al., 2013**)**. Majority of these are limited to regional extents and often fails to accommodate the complexity of terrains. In recent years, irradiance products from several RCM/GCM, reanalysis or multi-satellite and gauge observations are available at global scale such as GLDAS (Rodell et al., 2004), CALIPSO (Kato et al., 2011; Stubenrauch et al., 2013), JRA-55 (Kobayashi et al., 2015), Flashflux (L'Ecuyer et al., 2008), CERES (Loeb et al., 2012; 2005), etc. Some national level energy flux products are derived from geostationary satellites such as GEOS (Holdaway and Yang, 2016), METOSAT (Stökler et al., 2016; Razagui et al., 2017), INSAT (Bhattacharya et al., 2013; Vyas et al., 2016), etc.[1] These products projected at surface are nullifies complexity in surface topography due to coarse resolution. Therefore, such global and national products are inappropriate in hydrological applications driven by solar radiation in mountainous regions. The variability in topography in mountainous regions is largely responsible for spatial heterogeneity in irradiance (Swift and Knoerr, 1973; Gates, 1980b). In the recent past, algorithms had been proposed for computation of insolation which include variability

[1] The acronyms for the products are presented in the list of abbreviations

in earth's surface (Kumar et al., 1997; Tovar-Pescador et al., 2006**)** in the form of digital elevation models (DEM). These algorithms have the advantage of considering insolation as a function of topographical features such as elevation, slope, aspect and viewshed (Pelletier et al., 2017). Since, DEM is crucial for regional accuracy in insolation (Huang et al., 2017), spatial heterogeneity of irradiance and diurnal accumulated irradiance (insolation) in complex watersheds could be best captured by a fine resolution DEM.

2.7. Time-series reconstruction

2.7.1. Harmonic analysis of time-series (HANTS)

HANTS is a popular algorithm used worldwide and has been concluded as one of the finest reconstruction techniques (Zhou et al., 2016; Geng et al., 2016; Julien and Sobrino, 2019) for land surface variables of recurring nature. It is represented as

$$RS = a_0 + \sum_{n=1}^{N} a_n \cos\left(2\pi f_n t\right) + b_n \sin\left(2\pi f_n t\right) \tag{2.8}$$

$$S = RS + \varepsilon \tag{2.9}$$

where, S, RS and ε are original time-series, reconstructed time-series and error series respectively; t represents the time against corresponding S, n represents the number of harmonic component associated with the frequency f, N is the maximum number of harmonic components associated with the frequencies (f_n), a_n and b_n are the coefficients of the cosine and sine components with f_n respectively, and a_0 is the baseline constant which is coefficient at zeroth frequency.

Application of HANTS on NDVI time-series was first seen for Southern African and American Continents in the works of Verhoef (1996). Roerink, Menenti and Verhoef (2000) described the details on parameterization in HANTS algorithm by demonstrating its application on AVHRR 10-daily-NDVI MVC over Europe. This algorithm has been used

for a variety of applications with the aim of consistent NDVI time-series availability. It includes assessing the impacts of climate on vegetation (Roerink et al., 2003; Jiang et al., 2014), understanding land cover dynamics (Morton et al., 2006, Wen et al., 2010; Wang et al., 2014), and determination of vegetation based biophysical variables (Wen and Su, 2004; Gokmen et al., 2013; Li, Jia and Zheng, 2014; Li et al., 2018) etc.

2.7.2. Data assimilation

Data assimilation differs from interpolation methods because it mathematically combines concepts with the help of observations for prediction (Reichle, 2008). It is used to achieve different goals like optimization, interpolation, hindcasting and forecasting where the methods depend according to the goals. There are several linear and non-linear methods used for assimilation and predict the missing data. But data assimilation can be broadly distinguished into sequential and non-sequential assimilation (Bouttier and Courtier, 2002). These approaches are classified according to time of observation made and application for prediction. Probability equalization of cumulative distribution functions (CDFs) is a simple but effective assimilation technique used in solving a variety of problems like bias correction, statistical downscaling, quintile mapping, histogram equalizing, and rank matching (Ines and Hansen, 2006; Baigorria et al., 2007; Piani et al., 2010a; Piani et al., 2010b).

2.8. Dimensionality reduction

Principal component analysis (PCA) is a multivariate technique that analyses a set of vectors in which observations are described by several inter-correlated quantitative dependent variables (Abdi and Williams, 2010). There are two types of ways to describe these variance-covariance structure i.e. through linear or non-linear combinations (Hoffmann, 2007). However, mostly the linear form of PCA are used for the dimensionality

reduction due to simplified transformation. The PCA reduces the information of any number of dimensions to a transformation which yields principal components and generally the first and second components have most of the essential information. It is widely used technique in many fields for purposes like band reduction, noise removal and datamining including in the field of hydrological sciences (Kamali et al., 2007; Karlsson et al., 2012).

2.9. Hydrological models

In the hydrological studies, generally semi-distributed hydrological models (SDHM) or global hydrological models (GHM) are preferred. TOPMODEL (Beven and Kirkby, 1979) is one of the early conceptual rainfall-runoff models which is used worldwide. It is semi-distributed in nature which uses topography and soil transmissivity information to estimate runoff generation. It calculates storage deficit depending on topographic index replicating exponential Green-Ampt method (Green and Ampt, 1911) for runoff generation. The Variable Infiltration Capacity (VIC) model developed by Liang et al. (1994) integrates large-scale parameterization of infiltration, and it uses small-scale equations for simulating the storage and transmission of water through the upper portion of the soil matrix. Due to the advantage of integrating simulations at macroscale, VIC model is used for global water balance studies (Bennett et al., 2018). Integration of ecological factors can add new dimension in hydrological modeling. With this intentions, Water and Energy Transfer in Soil Plant and Atmosphere (WetSpa) Model was developed with conceptualization of a basin hydrological system by including atmosphere, canopy, root zone, transmission zone, saturation zone etc. (Wang et al., 1996). But, the more the elements are included, the more the sources of uncertainties increase. The Soil Water Assessment Tool (SWAT) model is one of the distributed hydrological models and it is being widely used for spatial analysis at the watershed level (Arnold et al., 1998). Recently, SWAT has gained popularity due to

the capability to adjust and calibrate the parameters to minimize the uncertainty (Thavhana et al., 2018). However, this model has the limitation of lumping the spatio-temporal information. Despite the popularity of SWAT, a parallel branch of hydrological modeling is focused on process-based concepts, eg. ISBA–MODCOU (Habets et al., 2008; Decharme et al., 2013) considering land surface model Interaction Soil–Biosphere–Atmosphere (ISBA) and the distributed hydrological model MODélisation COUplée (MODCOU); Soil–Water–Atmosphere–Plant (SWAP) developed by Kroes et al. (2003) keeping focus on irrigation and drainage assessments; and Water and Energy Transfer between Soil, Plants, and Atmosphere under quasi-Steady State (WetSpass) which performs the water balance computation at a raster cell level (Abdollahi et al., 2017).

2.10. Advances in process-based hydrological modeling

A process-based hydrological model can be in form of a mathematical formulation representing the hydrologic state variables describing the physical processes. It can be developed by combining two ideas: observability and scale (Fatichi et al., 2016). The runoff generation is considered as one of the important hydrological processes at the beginning of water cycle. It describes the initial partition of precipitation into surface and sub-surface. There are evidences of a threshold-based runoff delay in hilly watersheds of humid tropical or sub-tropical regions (Williams et al., 2002). Many hydrologists argue with collective experiments at watershed scale that this delay is due to antecedent conditions of soil (Penna et al., 2011). However, most of them have reported diverse observations in hillslope and riparian zones of the watersheds.

Another branch of researchers specialized in hillslope experiments have mentioned that runoff delay is caused by presence of macropore fraction (Torres et al., 1998; Shougrakpam et al., 2010; Sharma et al., 2013; Sarkar et al., 2015). The Macropores are large soil pores

in soil, usually greater than 0.08 mm in diameter which allow free movement of air and water by gravity (Chouksey et al., 2017). The macropore network triggers the preferential flow characteristics as the first draw from precipitation (Tromp-van Meerveld and McDonnell, 2005; Graham et al., 2010; Penna et al., 2011) thereby delaying the surface runoff generation. It determines what fraction of precipitation bypasses the root zone and directly contributes to subsurface flow (Menichino et al., 2014). Preferential flow drawn from rainfall due to presence of macropores is considered as the primary dominant control on runoff generation at hillslope scale. The variation of macropore distribution is often associated with different land covers due to which its impact on runoff generation is studied (Niehoff et al., 2002; Bachmair et al., 2009; Das et al., 2014; Mayerhofer et al., 2017). It can be interpreted from these studies is that land cover has strong control over water flow in soils due to which contrast in runoff response to rainfall is seen. However, a common phenomenon is observed that the wet phase has shorten delay in runoff generation than the dry phases. It is due to active macropore network which increases the connectivity thereby raising the hydraulic conductivity in the vadose zone of hillslopes (Graham et al., 2010). Therefore, another important aspect is the topsoil matrix which is highly crucial in defining the preferential flow and infiltration process altered by macropores (Bachmair et al., 2009).

In the last two decades, there have been substantial conceptualization of hydrological processes at hillslope scales via. experimentation at field sites. However, most studies require hydrological applications at watershed scale. Despite of several recent advances in hydrological processes at hillslope, the growth in its application for hydrological predictions at watershed scale is very little (Sivapalan, 2003). There could be various reasons but mostly it is cited as due to heterogeneity, complexity, uncertainty, etc. while upscaling from hillslope to watershed. Commonly, the field experiments conclude the observed hydrological processes to be complex at the hillslope. However, regardless of

complexity in process-based hydrological concepts, spatial scale is important over which hydrological effects of land cover are dominant (Ogden et al., 2013). As a guidance to develop effective process-based hydrological model, past studies have advised to focus on dominant processes rather than unnecessary detail in order to upscale the concept from the hillslope to the watershed (Sivapalan, 2003; Graham and McDonnell, 2010).

Chapter 3

Reconstruction of Land Surface Vegetation

3.1. Introduction

Satellite-derived Normalized Difference Vegetation Index (NDVI) has the proficiency to reveal surface vegetation strength. Consistent spatio-temporal availability of NDVI is a necessity for time-series based studies in many fields. Most of the NDVI reconstruction techniques are highly dependent on the available data at a specific location. Hence, a major limitation arises with possibility of insufficient observation frequency which can affect the quality of NDVI continuity in time-series. HANTS is no different from other methods and shows poor performance during large data gaps in the NDVI time-series (Xu et al., 2015; Zhou et al., 2015). It is difficult to attain good performance for all possible combinations of gap solely by HANTS (Atzberger and Eilers, 2011b). Therefore, pre-filling the NDVI time-series prior to application of HANTS have been addressed in limited recent studies, eg. Temporal-Similarity-Statistics (TSS) by Jia et al. (2011) and spline by Liang et al. (2017). However, pre-filling in these studies are either limited to temporal dependence or do not reflect the land surface phenology. There is a need to incorporate efficient methodologies to overcome this problem. Musial et al. (2011) concluded that the optimal gap-filling approach for geophysical time-series depends on the type and distribution of gaps. This chapter introduces a method to capture the similar temporal variation in NDVI time-series within a confident spatial extent. Then this information is utilized to increase relevant observation frequency in NDVI time-series to as a support for application of HANTS algorithm.

3.2. Land surface phenology

Phenology is the timing of recurring biological events driven by biotic and abiotic forces (Liu et al., 2014). Land surface phenology deals with cyclic pattern of land surface vegetation and it is used as a key indicator of vegetation dynamics. Application of HANTS algorithm has enabled to understand the vegetation evolution and phenological characteristics in the last two decades (Jun et al., 2009; Liu et al., 2014; Anav et al., 2018). The phenology of vegetation is largely associated with climate and terrain characteristics (Azzali and Menenti, 2000; Chen, 2017; Kiapasha et al., 2017). Moreover, vegetation in the same ecoregion faces similar climate and human conditions (Yang et al., 2017). Due to this reason, various classes of land-use/land-cover (LULC) are often classified by using land surface phenology (Friedl et al., 2002; Padhee et al., 2017). Therefore, we can draw that land surface phenology of a particular LULC is supposed to vary similarly to that of same LULC with identical conditions in same ecoregion. However, formerly the time-series data of NDVI is used to delineate land surface phenology (Xiao et al., 2009). NDVI time-series dataset reflects natural phenomena which is nonlinear (Verma and Dutta, 2013) and usually is a resultant of components like noise, inter-annual fluctuations, and long-term trends (de Beurs and Henebry, 2005; Verbesselt et al., 2010). It means NDVI trajectory continuously tends to follow local phenology (phenology at a spatial location or pixel) and any deviation from it is due to noise, inter-annual fluctuations, and/or long-term trends. Since, there is a strong link between NDVI, local phenology and regional LULC, approaches involving spatio-temporal investigation of land surface phenology of LULC are expected to grasp essential evidences for missing NDVI in highly cloud-contaminated regions.

3.3. Data used

MODIS-NDVI is one of the widely used NDVI MVC products in research related to vegetation phenology (Beck et al., 2006; Bucha and Koren, 2017; Testa et al., 2018). The NDVI 16-daily MVC product from Terra-MODIS (MOD13A1 v006) at 500 m spatial resolution (Didan, 2015) for a study period of years 2001 – 2016 was used to carry out the reconstruction. This product was downloaded from the website (https://lpdaac.usgs.gov/). MOD13A1 product is available with quality assurance (QA) layer with 16-bit codes as flag. Only reliable values (i.e. flag "0000" or pixels unaffected by atmospheric obstructions) are selected as the NDVI time-series values in this work. Fig. 3.1 shows the percentage of NDVI data availability in order to present the severity in the study area.

The annual land use/land cover (LULC) data from MODIS (MCD12Q1 v006) was also used for this work. This product is having IGBP global vegetation classification scheme (Friedl et al., 2002) at a spatial resolution of 500 m. The annual LULC time-series was divided into two groups, i.e. static and dynamic on the basis of whether a LULC class of a pixel remains same for 16 years of study period or changes (Fig.1.). Most of the study area is covered with forest cover. Also, water and snow classes were used for masking on NDVI data in the respective years. It is because this study is meant for reconstruction of NDVI time-series for areas which are vegetated round the year.

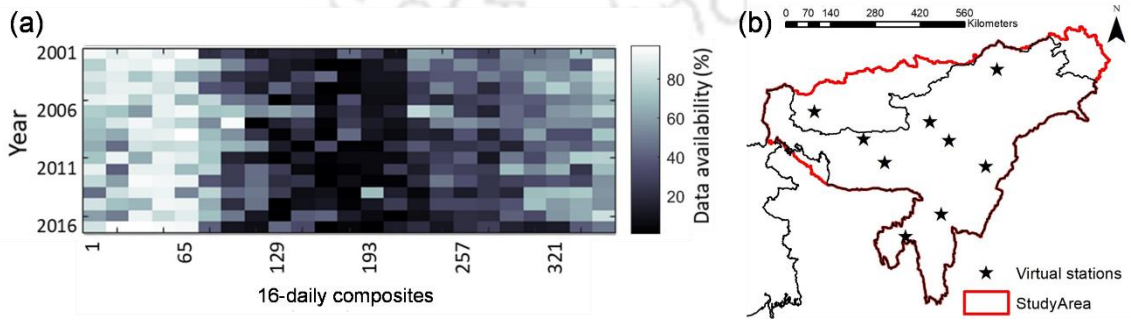

Figure. 3.1 (a) MODIS NDVI availability and (b) virtual stations in the study area.

Standard pixels were selected as virtual stations for methodological evolution, validation and performance evaluation of the proposed approach (Fig. 3.1b). One random pixel from three major LULC in each ecoregion (Table 1.1) having the properties of spatial homogeneity and temporally static LULC (Fig. 1b) throughout the study period (2001-2016) were selected as virtual stations. The details of these virtual stations are presented in Table 3.1. A pixel was considered as spatially homogenous if the LULC class of its surrounding eight pixels are of same class, whereas temporally static if its LULC class has not changed in the study period.

Table 3.1. Details of the virtual stations used in the study area. (**Note:** Codes for LULC: MXF – mixed forest; GRS – grassland; CRP – cropland; VEG – natural vegetation; SVN – savanna; EBF – evergreen broadleaf forest; Codes for Ecoregion: HIM – Eastern Himalaya; ASP – Assam Plains; NEH – Northeast Hills.)

Virtual Station	LULC	Latitude	Longitude	Ecoregion
VS1	MXF	28.54	94.61	HIM
VS2	GRS	27.07	92.72	
VS3	CRP	27.35	89.47	
VS4	CRP	26.57	90.85	ASP
VS5	VEG	25.92	91.45	
VS6	SVN	26.54	93.26	
VS7	EBF	24.47	93.04	NEH
VS8	SVN	23.84	92.04	
VS9	EBF	25.81	94.30	

3.4. Methodology

The schematic diagram of methodology followed in this work is presented in Fig. 3.2. It shows the methodology which is applied for pixels having both static and dynamic LULC. The portion of flow chart within the dashed box differs for pixels having static and dynamic LULC where N_L stands for the number of LULC classes existent at a pixel in 16 years of the study period. However, rest of the portion is commonly applied for all the pixels. A

detailed description of the various components of the flowchart is presented in this section.

3.4.1. Reference phenology curve

It is essential to have a reference trajectory of annual phenology at corresponding pixel to control the pre-filling. So, annual reference phenology curve ($NDVI_{ref}$) was computed for each pixel from annual NDVI series (2001 – 2016) as shown in Eq. 3.1 to Eq. 3.3.

$$NDVI_{ref}^{i,j} = \left(NDVI_{max}^{i,j} + NDVI_{med}^{i,j} \right) / 2 \quad (3.1)$$

$$NDVI_{max}^{i,j} = \max \left(NDVI_{k}^{i,j} \right) \quad (3.2)$$

$$NDVI_{med}^{i,j} = \text{median} \left(NDVI_{k}^{i,j} \right) \quad (3.3)$$

where, (i,j) represents spatial location of the pixel, the subscripts *ref*, *max* and *med* represent reference, maximum, and median, respectively computed at a specific temporal position (k) in annual curve of NDVI series. Due to absence of median and maximum values, computation of reference is not possible. Such points on the annual $NDVI_{ref}$ curve were left as null data. The $NDVI_{ref}$ curves affected by null values were restored by a search and fill algorithm (SFA) as shown in Appendix-A2. Abruptness of $NDVI_{ref}$ curve due to limited statistical observations is smoothed to produce $SNDVI_{ref}$ by HANTS to represent true reference phenology curve with continuous trajectory. The HANTS parameter setting is presented in the Appendix-A1.

3.4.2. Moving offset method (MOM)

It was assumed that the temporal continuity of NDVI changes from one point of time to another continuously and non-linearly but tends to follow the local phenology. The offset of valid NDVI points to its corresponding points on $SNDVI_{ref}$ at the extreme of missing span are linearly interpolated. Later, missing NDVI values are predicted by adding the

interpolated results with the points at $SNDVI_{ref}$. By the virtue of moving the linearly interpolated offsets on reference phenology curve, this method of pre-filling is named as Moving Offset Method (MOM). This method was directly used for pre-filling NDVI time-series with the help of $SNDVI_{ref}$ time-series for the study period. A conceptual demonstration of MOM for pre-filling the missing NDVI is presented in Fig. 3.3. In the figure, W_1 and W_5 represent the offset of NDVI from $SNDVI_{ref}$ time-series at the extreme ends of missing span.

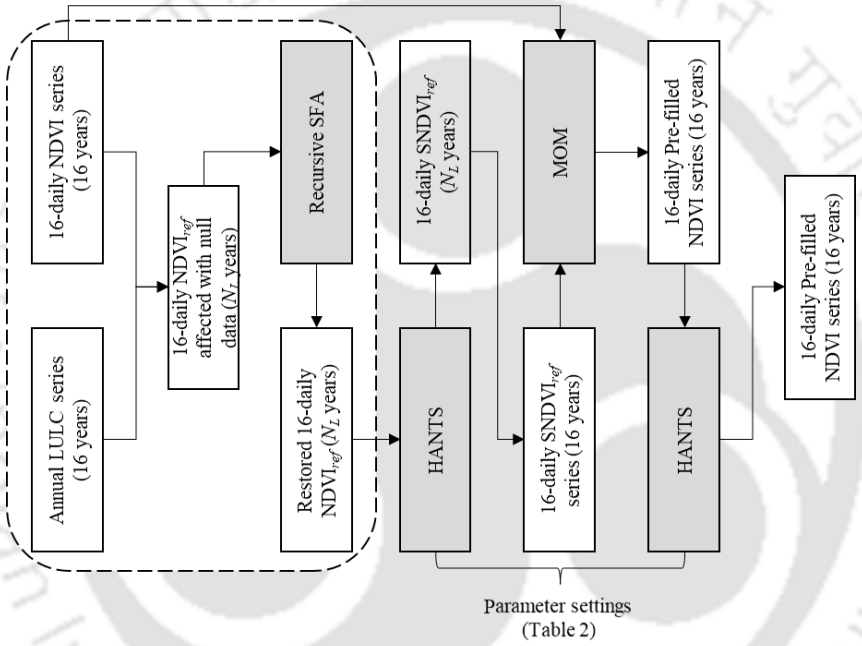

Figure 3.2. Schematic flow diagram for reconstruction of NDVI time-series by using MOM and HANTS where $NDVI_{ref}$ is the reference phenology curve, $SNDVI_{ref}$ is the smoothed reference phenology curve, NL represents number of LULC classes at a pixel from 16 years (2001 – 2016).

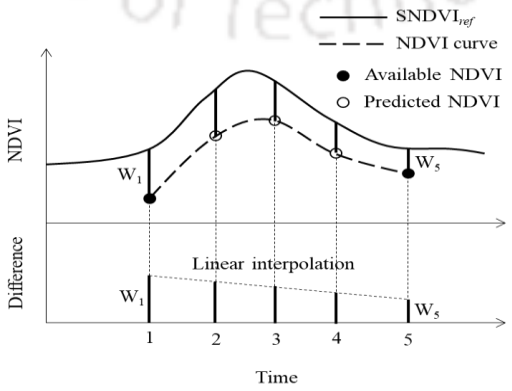

Figure 3.3. Conceptual diagram of Moving Offset Method for pre-filling of NDVI time-series.

3.5. Results and Discussion

3.5.1. Robustness of MOM

MOM was compared with other popular interpolation methods (IDW and cubic spline) for checking its robustness in pre-filling the NDVI time-series. For this purpose, yearly NDVI data with highest availability at virtual station was intentionally reduced from the mid-year. The reduced annual data was applied to the three pre-filling methods MOM, IDW and cubic spline. Variation of R^2 value with decrease in valid data was tested as a measure of robustness of predictions by the pre-filling methods.

The virtual stations, VS1 (mixed forest), VS4 (agriculture), and VS7 (evergreen broadleaf forest) were selected for checking the robustness of MOM. For VS1 and VS4, year 2006 was found as the least problematic year with a data availability of 86.9% and 73.9%, respectively. Similarly, year 2001 was found least problematic with a data availability of 95.7% for VS7. Fig. 3.4 shows the coefficient of determination (R^2 value) for interpolating the missing NDVI values in the year with variable data gaps against original NDVI values. Since, the first set of graphs (Figs. 3.4a, 3.4d, and 3.4g) are plots for interpolated NDVI against original NDVI in the respective years, it shows R^2 value as 1 for all the methods. However, an overall decline in R^2 value for all the methods at all virtual stations could be seen with decrease in data percentage. MOM is found with better predictions than IDW and cubic spline in VS1 and VS4 with R^2 value over 0.8 (Fig. 3.4b, 3.4c, 3.4e, 3.4f), while at VS7, cubic spline was found as the best predicting method with R^2 value over 0.8 where MOM was moderate with R^2 value of 0.78 (Fig. 3.4i). Both cubic spline and IDW methods failed during low data availability at VS1 (Fig 3.4c) and VS4 (Fig. 3.4f), respectively (with R^2 value under 0.5 in both cases). Therefore, it can be considered that MOM is more robust for predicting NDVI time-series in variable data gap conditions than IDW and cubic spline methods.

3.5.2. Seasonality trait in different approaches

A comparative analysis between reconstructed NDVI time-series by four approaches at the virtual stations and in the study area was also conducted. The approaches are (i) HANTS (HA), (ii) IDW prior to HANTS (IHA), (iii) cubic spline prior to HANTS (SHA), and (iv) MOM prior to HANTS (MHA). The parameter settings for application of HANTS to reconstruct annual time-series is shown in Table A2.

The seasonality trait is based on visual interpretation of surface plot of time-series against years where the anomalies in seasonal high, low and transition is compared during reconstruction span. The reconstructed time-series for VS1, VS4 and VS7 are shown in Fig. 3.5. Most data deficient years were found as 2015 and 2016 for VS1, 2008, 2012 and 2016 for VS4 and year 2016 for VS7. Due to long gaps of missing values in above mentioned years, application of HA with the parameter settings (Table A2) is not able to reconstruct values in respective seasonal range. Rather, HA predicted a series of low values (as set in low threshold setting in Table A2) in this time. It shows failure of direct application of HA to long data gaps.

Addition of an pre-filling method prior to application of HANTS was helpful in overcoming this problem. Visual interpretation of Fig. 3.5 shows the shortcomings of IHA and SHA as compared to MHA. For VS1 (mixed forest), the mark near (i) shows that IHA was unable to identify seasonal low and overestimates in years 2015 and 2016. A similar overestimation was seen by SHA in year 2016 as shown in mark near (ii). But MHA was observed to predict seasonal low properly in the years 2015 and 2016 for VS1. For VS4 as agriculture, the occurrence of dormant and peak seasons is equally important where a clear boundary separating the two seasons is logical due to yearly crop calendar and human activities. Comparison between vertical lines drawn near (iii), (iv) and (v) shows that

division between dormant and agricultural season is more prominent for the case of MHA than IHA and SHA. Also, IHA was unable to reconstruct seasonal low in year 2016 as shown at mark near (vi), whereas MHA and SHA succeeded. For VS7 (evergreen broadleaf forest), all MHA, IHA and SHA performed similarly except for that IHA failed to reconstruct seasonal low in 2016 as shown at mark near (vii). From visual observation it was found that MHA satisfied most of the details of seasonality trait for virtual stations as compared to HA, IHA and SHA.

3.5.3. Fitting performance

The fitting performance of reconstructed NDVI was evaluated on the basis of three indicators. The first indicator is linearity of reconstructed NDVI time-series (RNDVI) with $SNDVI_{ref}$ time-series represented by correlation coefficient (R value). It represents the capability of approach to reconstruct NDVI time-series in relevance to seasonality trait. The second indicator is Normalized Noise Related Error (NNRE) which is proposed by Zhou et al. (2016) as fitting evaluation standards. NNRE is the normalized difference of Fitting method Related Error (FRE) and Overall Reconstruction Error (ORE) as described in Eq. 3.4 to 3.6.

$$FRE = \sqrt{\frac{\sum_{i=1}^{n}\left(SNDVI_{ref} - NDVI_{ref}\right)^2}{n}} \tag{3.4}$$

$$ORE = \sqrt{\frac{\sum_{i=1}^{n}\left(RNDVI - NDVI_{ref}\right)^2}{n}} \tag{3.5}$$

$$NNRE = \left(ORE - FRE\right)/\left(ORE + FRE\right) \tag{3.6}$$

Here $SNDVI_{ref}$ is fitted reference phenology curve, $NDVI_{ref}$ is the reference phenology curve, and RNDVI is reconstructed NDVI time-series, *n* is respective number of elements.

The ORE expresses overall reconstruction performance, while FRE estimates the accuracy of the mathematical descriptors of the reconstruction models. On a scale of -1 to 1, larger NNRE means a weaker influence of FRE on overall reconstruction or bad fit whereas small NNRE means the ORE can be mainly explained by FRE or good fit. Indicators of fitting performance i.e. R, ORE, FRE and NNRE for 16-daily time-series at virtual stations of the study area are presented in Table 3.2.

It shows that ORE exceeded the error limit of 0.05 with highest values at most of the instances for HA. The worst performance is mainly due to inability of HA to reconstruct at large data gaps. Addition of an interpolation prior to application of HANTS reduced this error remarkably. However, except for VS1, methods other than MHA could not reduce ORA below 0.05. The FRE always stayed below 0.05. It is only at VS9 that HA performed best due to least problems in large data gaps in original time-series. MHA performed best with lowest ORE and NNRE at majority of virtual stations (VS1, VS3, VS4, VS5, VS6, VS7 and VS8). In other cases, IHA performed best at VS2, but the performance of MHA at VS2 was second best with marginal difference in NNRE than that of IHA. MHA was also seen having NNRE with slim difference to that of HA at VS9. It was seen that unlike HA, IHA and SHA, on the basis of ORE and NNRE, the performance of MHA is either best or second best with marginal difference than that of the best method. Also, the correlation coefficient (R value) of MHA with local reference phenology curve is highest for all the virtual stations. It signifies that MHA have more capability to restore local phenology pattern in reconstructed NDVI time-series which is reasonable according to

seasonality trait. On an overall understanding, MHA was able to effectively fit the shortcomings which were faced with HA.

Fig. 3.6a shows the overall fitting performance of HA, MHA, IHA and SHA approaches over the study area. The distribution of NNRE in the boxplots shows that overall population between the 1st and 3rd quartiles along with median is least in case of MHA from all other approaches. The spatial averages of NNRE for the study area with various approaches were found as 0.21, 0.25, 0.29, and 0.19 for HA, IHA, SHA and MHA, respectively. It indicates that a major part of the study area has reduced NNRE, which means better fitting performance by MHA than other approaches. Similar comparison for coefficient of correlation with reference land surface phenology in Fig. 3.6b shows maximum R for MHA. The spatial averages of R for the study area with various approaches were found as 0.78, 0.77, 0.64, 0.88 for HA, IHA, SHA and MHA, respectively. It means reconstructed NDVI time-series from MHA has better association with seasonality trait.

3.6. Conclusion

Consistent availability of high-quality spatio-temporal NDVI time-series data (e.g., MODIS/SPOT/AVHRR etc.) is important for various terrestrial studies. It has led to development of several reconstruction methods. However, most of these methods draw information temporally from the available NDVI time-series to reconstruct itself. Such approaches lead to misestimate reconstruction outcomes when met by large data gaps. Hence, a new pre-filling method, MOM is adopted to improve the observation frequency. This method increases the relevant NDVI values in the time-series by hypothesizing that vegetation in the missing span should vary according to a general pattern of reference phenology. Utilization of phenological pattern in MOM increases the robustness in data deficient cases as compared to other mathematically driven interpolation techniques like

IDW and cubic spline. It supports the reconstruction and smoothing algorithms to predict approximate values during the missing span. Spatio-temporal comparison of seasonal and fitting performance evaluated for years 2001 – 2016 shows MOM with HANTS (MHA) to be superior than other interpolation methods. The NNRE for MHA was found to be lowest than other approaches (spatial average of 0.19). Also, in maintaining the seasonal trait, correlation with general phenology R was found to be highest than other approaches (spatial average of 0.88). Hence, MOM can be concluded as a prerequisite of HANTS in NDVI time-series reconstruction.

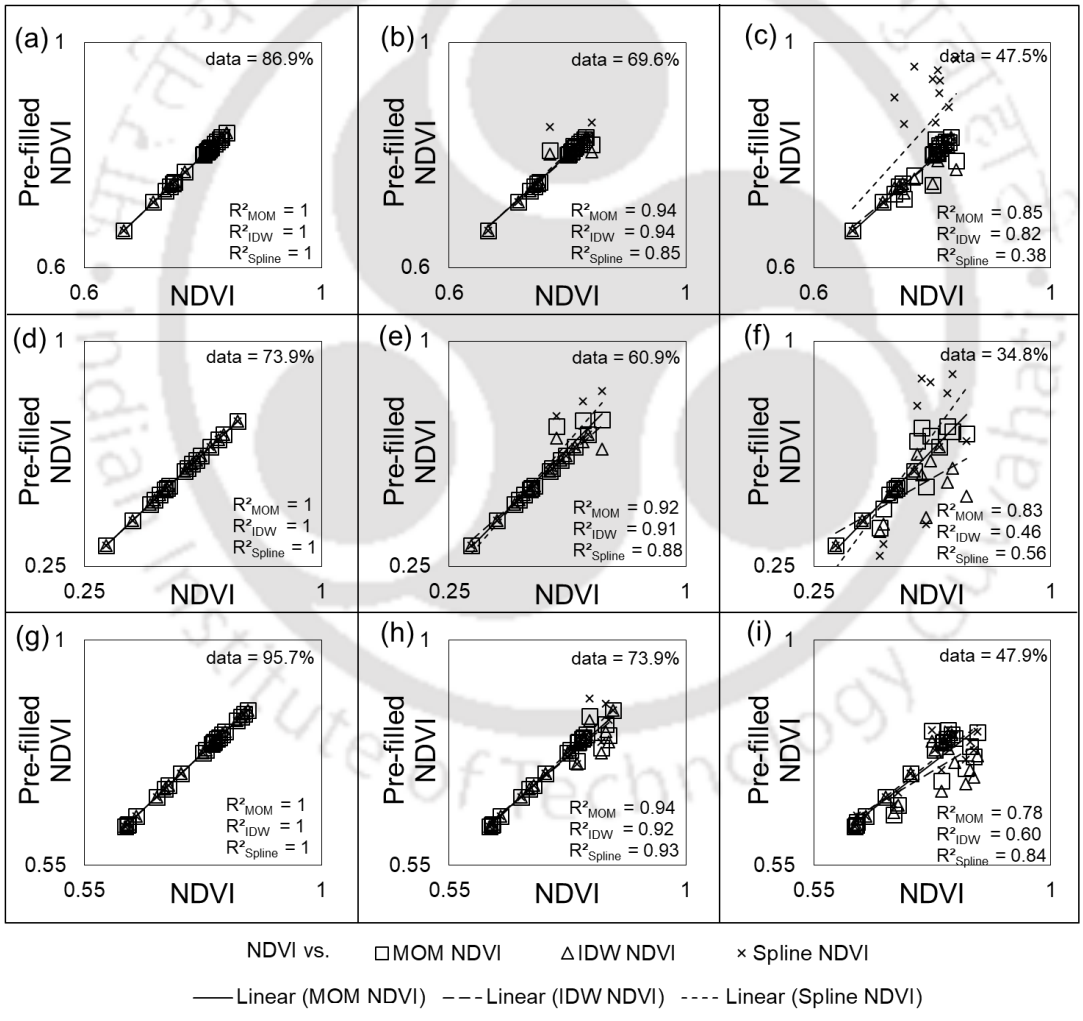

Figure 3.4. Performance of MOM, IDW, and cubic spline interpolation methods in prefilling NDVI time series at virtual stations. Prefilling at VS1 in year 2006 with data availability of (a) 86.9% (original data), (b) 69.6%, and (c) 47.5%. Prefilling at VS3 in year 2006 with data availability of (d) 73.9%, (e) 60.9%, and (f) 34.8%. Prefilling at VS7 in year 2001 with data availability of (g) 95.7%, (h) 73.9%, and (i) 47.9%.

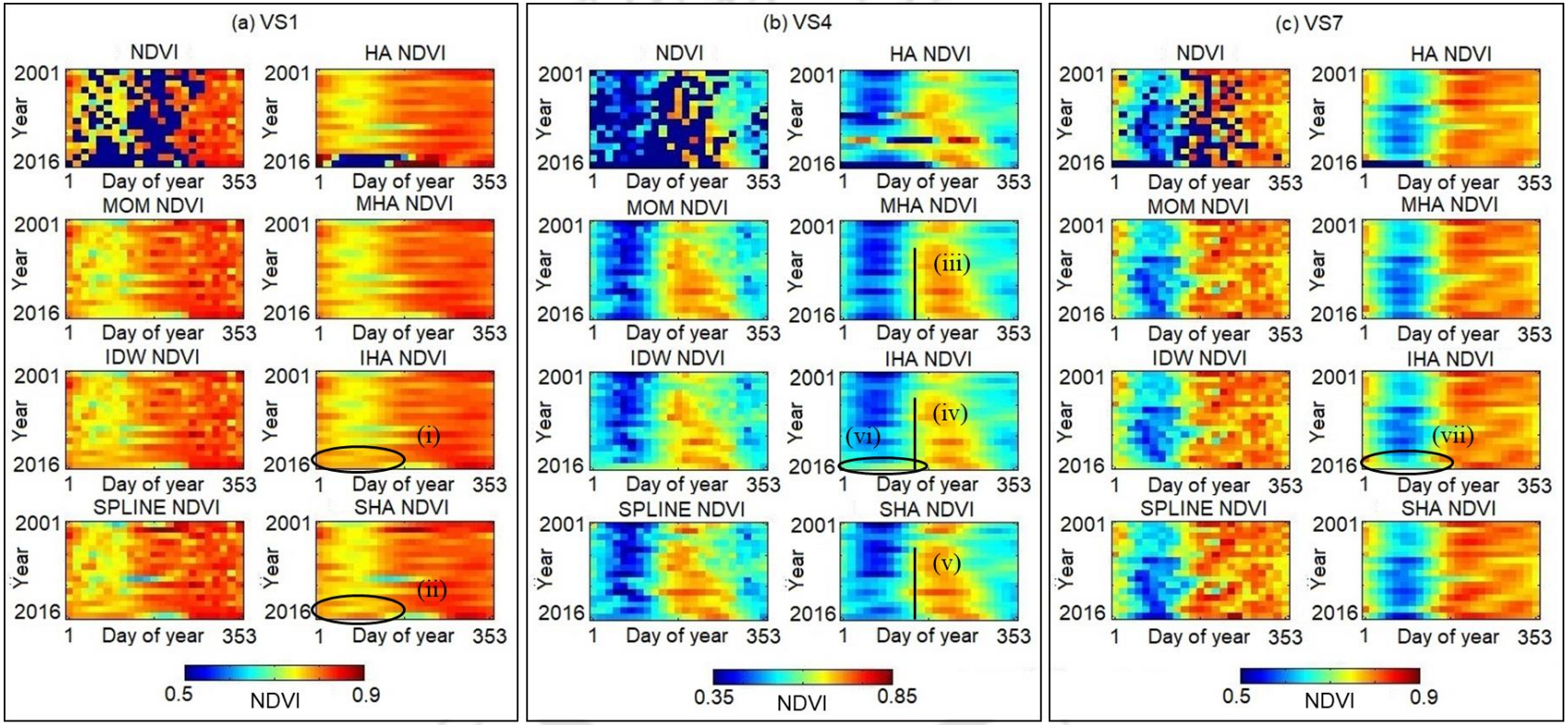

Figure. 3.5. The sixteen annual NDVI series for the virtual stations by different approaches (HA, MHA, IHA and SHA). (a) VS1: Mixed forest, (b) VS4: Agriculture, (c) VS7: Evergreen broadleaf forest.

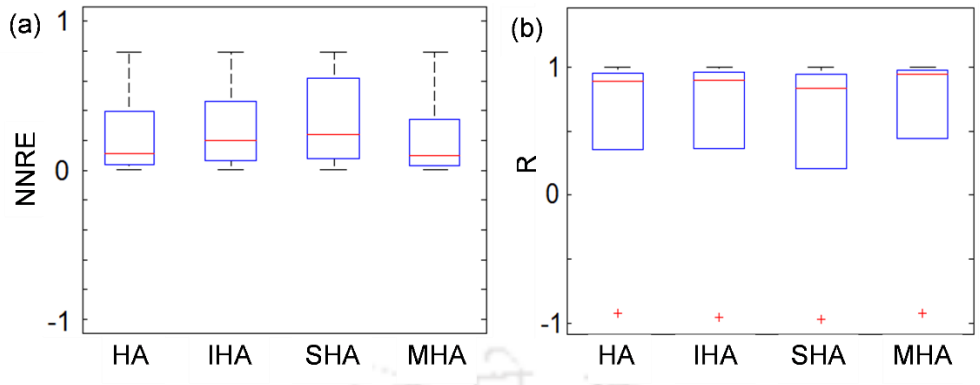

Figure 3.6. Performance of NDVI reconstruction without and with pre-filling methods in the study area evaluated in the terms of (a) curve fitting and (b) phenological similarity.

Table 3.2. Indicators of fitting performance at virtual stations in the study area (**Note:** Best values are bolded).

Virtual Station	R				ORE				FRE	NNRE			
	HA	IHA	SHA	MHA	HA	IHA	SHA	MHA		HA	IHA	SHA	MHA
VS1	.4507	.7643	.6567	**.8026**	.1291	.0644	.0649	**.0636**	.0084	.8778	.7692	.7708	**.7666**
VS2	.2750	.8613	.8190	**.8690**	.0991	**.0311**	.0367	.0321	.0084	.8437	**.5746**	.6274	.5851
VS3	.3568	.9379	.8772	**.9655**	.1888	.0609	.0728	**.0419**	.0204	.8049	.4981	.5622	**.3451**
VS4	.6156	.8903	.8952	**.9334**	.1238	.0567	.0548	**.0483**	.0273	.6386	.3500	.3349	**.2777**
VS5	.9264	.9617	.9396	**.9694**	.0575	.0429	.0473	**.0411**	.0147	.5927	.4895	.5258	**.4731**
VS6	.7588	.9008	.9101	**.9303**	.0875	.0461	.0469	**.0426**	.0344	.4356	.1453	.1537	**.1064**
VS7	.6942	.9229	.9234	**.9375**	.0852	.0392	.0403	**.0373**	.0099	.7917	.5967	.6055	**.5805**
VS8	.6729	.9524	.9186	**.9634**	.0970	.0366	.0408	**.0333**	.0147	.7367	.4269	.4702	**.3875**
VS9	.9726	.9730	.9734	**.9746**	**.0386**	.0443	.0402	.0390	.0204	**.3084**	.3693	.3267	.3131

Chapter 4

Reconstruction of Land Surface Temperature

4.1. Introduction

Land surface temperature (LST) is the radiative skin temperature of the earth's surface. It is an essential input in the energy balance models (Tian et al., 2013). Therefore, consistent LST data availability is anticipated to help in monitoring net energy to make their best utility. Satellite remote sensing technology has advantage over traditional ground-based measurements and its recent improvements have helped to obtain global spatio-temporal LST data. However, LST is affected by atmospheric obstacles because it is estimated using thermal region of the electromagnetic spectrum (Jiménez-Muñoz and Sobrino, 2003). The multi-temporal approaches have grown as promising methods to increase spatio-temporal consistency in LST. Most of these approaches are suitable for LST prediction in same physiography. Yet, these approaches are limited in addressing the performance in complex physiography due to other ancillary data as covariates. It is because the influence of ancillary data on LST might be limited to a same physiography. This chapter explains a framework based on multi-temporal approach to predict LST in complex physiography by using stochastic information. It uses LST as dependent and independent variables from two different sources for assimilation which eliminates the chances of complex relationship between two different variables.

4.2. Kernel density estimator

In case of a statistical population from consistent geophysical variables, generally the distribution is fitted by parametric means (e.g. Normal, Gaussian, Binomial, Exponential etc.) due to little frequency at high and/or low extremities. However, it is not possible to use parametric distribution in this work due to spatio-temporal data gaps. Therefore, non-parametric kernel density estimator (Jones, 1990; Harvey and Oryshchenko, 2012) is used to fit empirical distribution. The kernel density estimator returns a probability density function (PDF) from a sample data based on a normal kernel function evaluated at equally-spaced points that cover the range of the sample data. For any distribution $F(x)$ with a corresponding probability density function $f(x)$, the kernel density estimator $\mathrm{pdf}_w(x)$ at a point x by using a sample of w observations (bandwidth), is given by Eq. 4.1. Its corresponding cumulative distribution function (CDF) or $\mathrm{cdf}_w(x)$ is given by Eq. 4.2.

$$\mathrm{pdf}_w(x) = \frac{1}{aw}\sum_{i=1}^{a} K\left(\frac{x - x_i}{w}\right) \tag{4.1}$$

$$\mathrm{cdf}_w(x) = \frac{1}{a}\sum_{i=1}^{a} H\left(\frac{x - x_i}{w}\right) \tag{4.2}$$

Here, a is the sample size, K is the kernel smoothing function which is a bounded PDF symmetric about the origin (*i.e.* point x), and H is a kernel which takes the form of a CDF obtained by integrating K. The non-parametric distribution produced to fit empirical distribution from kernel estimator is called as kernel distribution and its resulting PDF and CDF curves are represented as $\mathrm{pdf}_x(x) = \mathrm{P}(X = x)$ and $\mathrm{cdf}_x(x) = \mathrm{P}(X \leq x)$ respectively.

4.3. Data used

The 8-daily LST composite product from MODIS TERRA satellite (MOD11A2) at a spatial resolution of 1 km^2 is used as microscale LST (LST_m). A study period of years 2001 – 2016 was selected. It is affected with spatio-temporal gaps in the study area as shown in Fig. 4.1a. It shows the spatio-temporal severity of LST inconsistency in the study area.

LST from Global Land Data Assimilation System (GLDAS) version 2.1 NOAH LSM product was used as macroscale LST (LST_M). It is developed by Rodell et al. (2004) and its various outputs are available at the website (https://disc.gsfc.nasa.gov). This product is forced with a combination of model and observation based forcing data sets. It is available at a spatial resolution of 0.25° and temporal resolution of 3 hours. Having high temporal consistency, this dataset is used to derive 8-daily composites of LST_M to be used as covariate series temporally equivalent with LST_m. Fig. 4.2 shows agreement between spatial and temporal variability of LST_M and LST_m reflected by spatial distribution of temporal correlation coefficient.

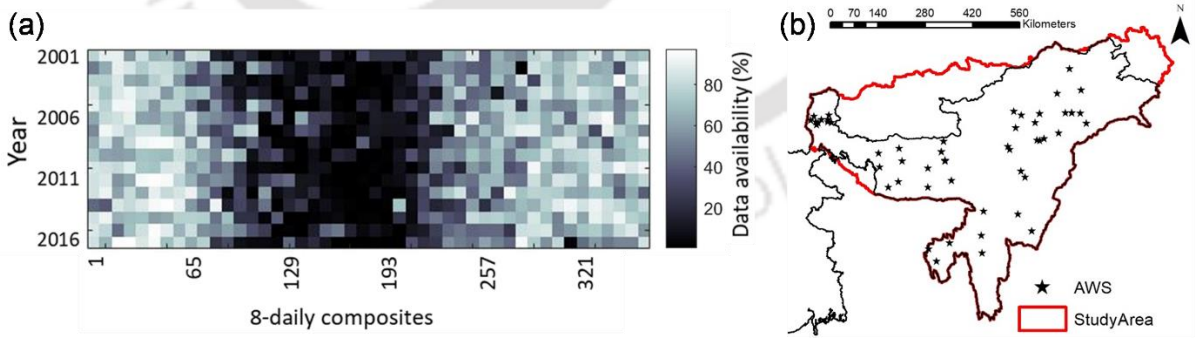

Figure 4.1. (a) MODIS LST availability and (b) automatic weather stations in the study area.

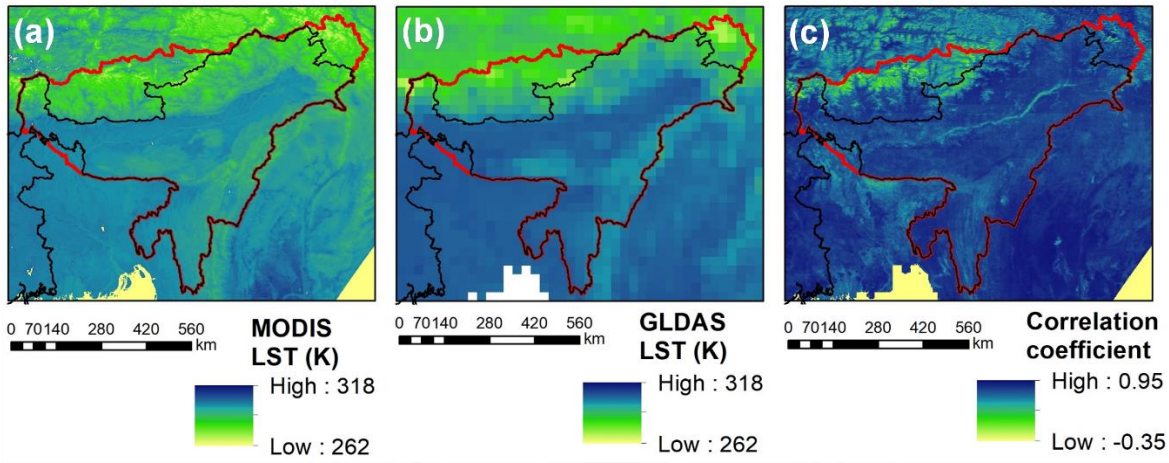

Figure 4.2. (a) Temporal median of MODIS LST, (b) Temporal median of GLDAS LST, and (c) Correlation between MODIS and GLDAS LST in the study area.

Also, temperature data from 57 automatic weather stations (AWS) spread around the study area (Fig. 4.1b) was downloaded from MOSDAC website (https://www.mosdac.gov.in/). Being air temperature, these ground-based measurements can't be directly validated with geospatial LSTs for precision but can be used to check their agreement on seasonality and ranges. Due to scarcity and inconsistency in the daily ground-based observations, 8-daily median during passing time of MODIS was used for comparison.

4.4. Methodology

Spatio-temporal assimilation was used to predict the data gaps between LST_m from LST_M by using kernel density estimator. The entire framework is divided into three parts, viz. temporal matching, temporal assimilation, and spatial assimilation. Temporal matching includes the pre-processing of 8-daily LST_M composites at temporal resolution compatible with LST_m. Accordingly, 3-dimensional matrices of LST_m and LST_M are prepared by temporally stacking spatial layers of 16 years. The first and second dimensions are assigned to space while third dimension is assigned to time in these matrices. Temporal and spatial assimilations are referred

as stage 1 and stage 2 respectively. In stage 1, temporal values in time dimension from LST_m and LST_M matrices is captured at a spatial location (directed by latitude and longitude); distribution in time is mapped by using non-parametric kernel distribution[2]; and a macroscale-to-microscale transfer function is used to predict a new set of temporal values. This process is routed till all locations across the spatial extent are completed to create a new 3-dimensional matrix (LST_{mT}) which is microscale LST predicted by temporal assimilation. In stage 2, values of LST_{mT} and LST_m in space dimension is captured for each 8-daily composite (directed by stacked layers); distribution in space is mapped by using non-parametric kernel distribution*; and a residual rectifying transfer function is used to predict a new set of spatial values. The process is routed till all 8-daily layers across the time-series are completed to create a new 3-dimensional matrix (LST_n) with corrected spatial residuals. This derivative is reconstructed LST by spatio-temporal assimilation. A typical representation of the framework is presented in Fig. 3.3.

4.4.1. Temporal matching

For assimilation, LST_M is required at approximate passing time of MODIS Terra satellite (1030 IST or 0500 GMT). It is done by fitting a curve across diurnal LST_M by first order Fourier fitting (Eq. 4.3) and returning the value at the specific time from the curve as shown in Fig. 4.4.

$$G(t) = a_0 + a_1 \cos(2\pi\ t) + a_2 \sin(2\pi\ t) \tag{4.3}$$

[2] Common observations as per the availability of MODIS LST are used.

Here, $G(t)$ is the resultant curve produced by Fourier fitting, a_0 models a constant (intercept) term in the diurnal data, a_1 and a_2 are the coefficients of the cosine and sine components with fundamental frequency (*i.e.* 2π), and t represents the variable time of day in hours. Later, the returned LSTs are averaged to produce 8-daily composites of LST_M.

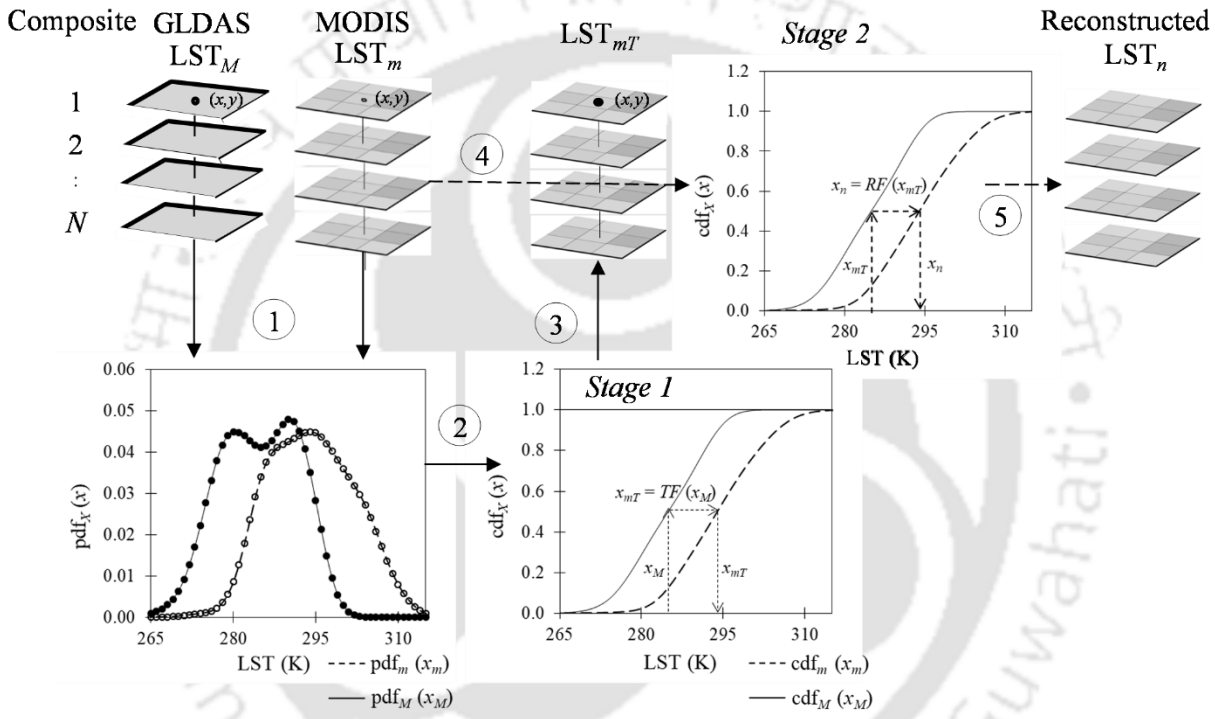

Figure 4.3. Schematic diagram of the spatio-temporal assimilation by using kernel distribution. Latitude and longitude is represented by (x, y). The circled numbers are steps where steps 1, 2, 3, 4, and 5 represents mapping of temporal PDF from LST_M and LST_m, conversion of temporal PDF to temporal CDF, prediction of LST_{mT}, mapping of spatial CDF from LST_m and LST_{mT}, and prediction of LST_n respectively.

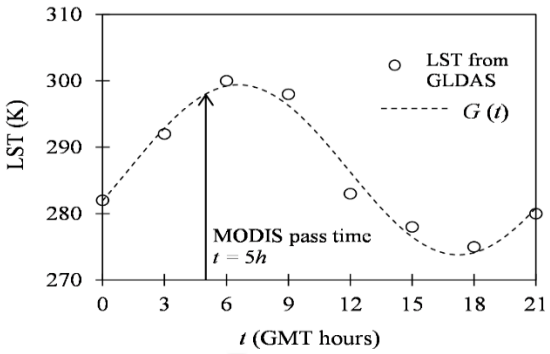

Figure 4.4. Extraction of LST at approximate passing time of MODIS from diurnal GLDAS LST data.

4.4.2. Temporal assimilation

Initial assumption is made that distributions of LST_m and LST_M are well approximated by kernel distribution. A new derivative (LST_{mT}) is signified as a function of LST_M or simply $x_{mT} = TF(x_M)$, where TF plays the role of macroscale-to-microscale transfer function. We utilize this function to predict LST_{mT} by using the non-linear relationship defined by probability equalization of CDFs of LST_m and LST_M in time dimension (Eq. 4.4). Hence it is named as temporal assimilation.

$$\mathrm{cdf}_m\left(TF\left(x_M\right)\right) = \mathrm{cdf}_M\left(x_M\right) \tag{4.4}$$

4.4.3. Spatial assimilation

There will be spatial difference (or spatial residual) between LST from predicted and satellite estimated images due to diverse daily conditions. This spatial residual is required to be corrected. Hence, a spatial residual corrected derivative (LST_n) is produced by mapping CDFs of LST_{mT} and LST_m in a similar way to the previous process but in spatial dimension. LST_n is signified as a function of LST_{mT} or simply $x_n = RF(x_{mT})$, where RF plays the role of transfer function to rectify spatial residual. Eq. 4.5 depicts spatial residual correction by using non-

linear relationship defined by probability equalization of CDFs of LST_m and LST_{mT} in space dimension or spatial assimilation.

$$\mathrm{cdf}_m\left(RF\left(x_{mT}\right)\right) = \mathrm{cdf}_{mT}\left(x_{mT}\right) \tag{4.5}$$

4.5. Results and Discussion

Having LST_m and LST_M at fine and coarse spatial resolutions respectively, the existence of spatio-temporal dissimilarity between these products are likely to affect LST_n. Accordingly, spatio-temporal investigation is followed to evaluate the performance of the methodology. For indicators of performance, root mean square error (*RMSE*) and absolute bias (*B*) are used as shown in Eq. 4.6 and 4.7 respectively.

$$RMSE = \left(\sum_{i=1}^{N}\left(O_i - P_i\right)^2 \Big/ N\right)^{\frac{1}{2}} \tag{4.6}$$

$$B = \left|\sum_{i=1}^{N}\left(O_i - P_i\right) \Big/ N\right| \tag{4.7}$$

These indicators are computed between two series, observed (O_i) and predicted (P_i), and N is the number entities. The indicator *RMSE* provided overall reconstruction performance whereas *B* indicated the overall deviation between O_i and P_i. These indicators are used independently for spatial and temporal verifications according to the necessity of verification. Additionally, the estimations from LST_n is also validated with available ground-based temperature measurements in the study area for checking the agreement with seasonal variation and range of prediction. Later, the values of LST_n are used to fill the spatio-temporal gaps in LST_m on the basis of overall evaluation.

4.5.1. Validation using MODIS original LST

The maps of temporal medians of LST_m and LST_n in 2001 - 2016 are shown in Fig. 4.5*. The scatter plot between the two maps confirm the restoration of spatial variation of LST with high accuracy (R^2 = 0.98; *RMSE* = 0.6 K; B = 0.36 K) in the study area. To investigate the performance of reconstruction in complex physiography, temporal *RMSE* and *B* between LST_m and LST_n were checked for three physiographic classes. These classes (highland, midland and lowland) were classified by using k-means clustering between the vectors from DEM and temporal median of LST_m in 16 years. Table 4.1 presents the area proportion by physiographic class and corresponding indicator statistics between LST_m and LST_n. Since, the extent of study area includes least proportion of highland (≈ 20%) and other physiographic regions with majority of area proportion show good accuracy, we considered the reconstruction method as feasible.

Table 4.1. Error statistics in physiographic zones in the study area.

Physiographic class	Area (Thousand km^2)	Area (%)	*RMSE* (K)	*B* (K)
Highland	86.23	20.49	4.11	17.68
Midland	115.17	27.37	2.32	5.58
Lowland	219.37	52.14	1.85	5.57
Overall	420.77	100.00	2.16	7.03

* Common observations as per the availability of MODIS LST are used.

4.5.2. Validation with ground data

Fig.4.6 shows the comparison between LST_m and LST_n with ground-based observations at three sample locations. It is found that most of the LST_n are within range of LST_m having positive correlation when compared against ground-based measurements. Therefore, we can consider that most of the predictions from LST_n are as good as LST_m. However, there are few seasonal underestimated predictions in the time-series plot (Fig. 4.6a) which can be also seen as outliers in the scatter plots (Fig. 4.6b). These disagreements are carried from pre-existing dissimilarity between MODIS and GLDAS in highland region (Fig 4.2c). It could be due to seasonal effect of snow cover in highland regions which could be undetected by GLDAS LST at coarse spatial resolution but captured by MODIS at high resolution. For an overall evaluation, a map of correlation coefficient (R) between LST_n pixels and various AWS points in the study area presented in Fig. 4.7. It is observed that out of 57 AWS, ranges of R is found as 0.5 – 0.6 at 8 AWS, 0.6 – 0.7 at 17 AWS, 0.7 – 0.8 at 26 AWS, and 0.8 – 0.9 at 6 AWS, with average R = 0.71. It confirms the credibility of predictions in reconstructed LST with good agreement with seasonal variation.

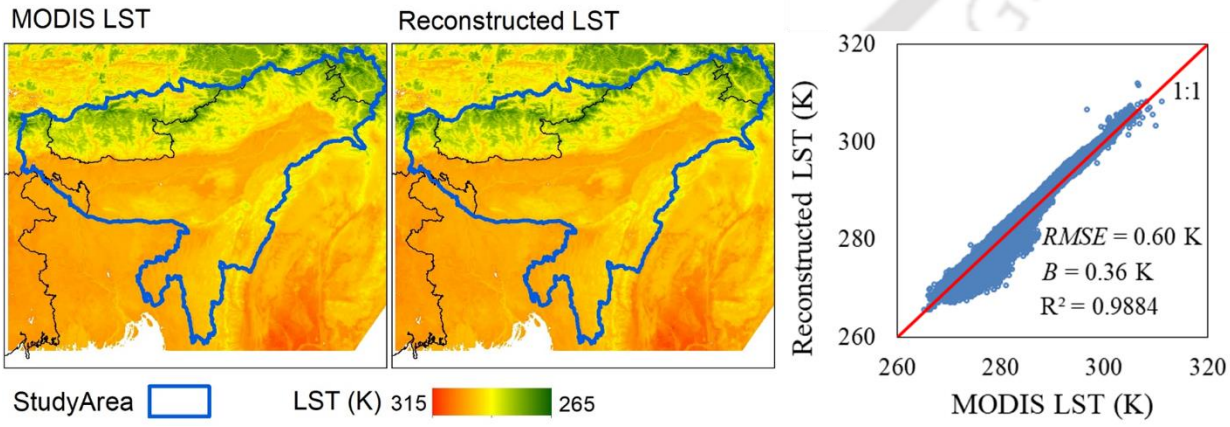

Figure 4.5. Spatial comparison between temporal medians of MODIS LST and reconstructed LST.

4.5.3. Uncertainty analysis

To know the source of uncertainty, we considered LST_m as the baseline data and computed its spatial mean of temporal *RMSE* and *B* with derivatives at various stages of assimilation and plotted it against the baseline data availability in percentage. Fig. 4.8a, 4.8b, and 4.8c shows the *RMSE* and *B* between MODIS LST (LST_m) against GLDAS LST (LST_M), LST after temporal assimilation (LST_{mT}), and LST after spatial assimilation (LST_n) respectively. It is found that most of the uncertainty are produced due to severe deficiency in LST_m (approximately $\leq$ 10%). The cases of severe deficiency in 2001 – 2016 is around 19%. However, 40% of reconstructed LST in these severe conditions is under *RMSE* of 4K and *B* of 10K. Comprehensively, Fig. 4.8d shows that with advances in assimilation stages, there is decline in overall distribution of *RMSE* and *B*. Hence, the spatio-temporal assimilation process is considered to be efficient.

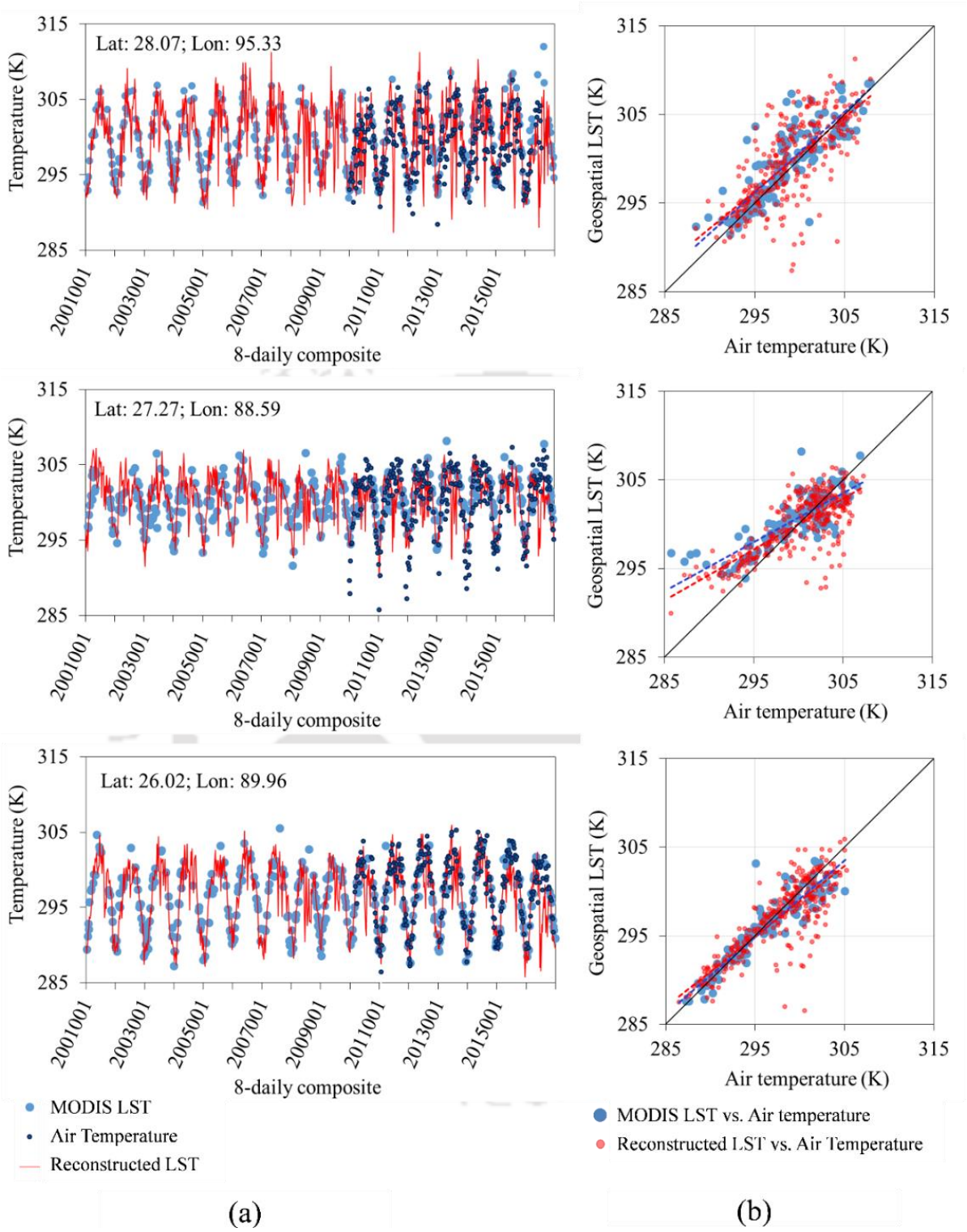

Figure 4.6. Comparison of MODIS LST and reconstructed LST with ground-based measurements for (a) seasonality by time-series and (b) range of prediction by scatter cloud.

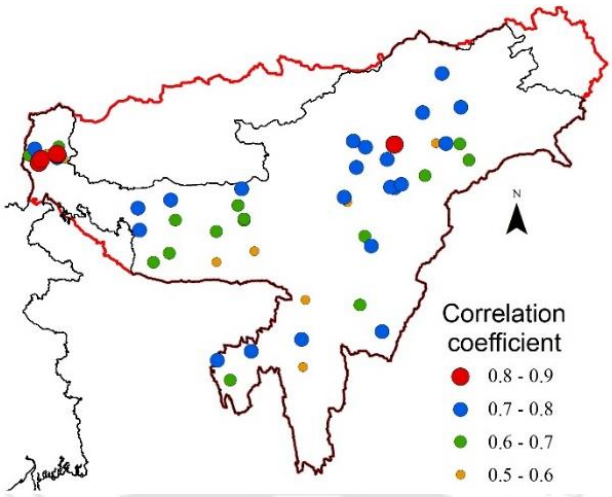

Figure 4.7. Distribution of correlation coefficient between reconstructed LST and ground-based measurements in the study area.

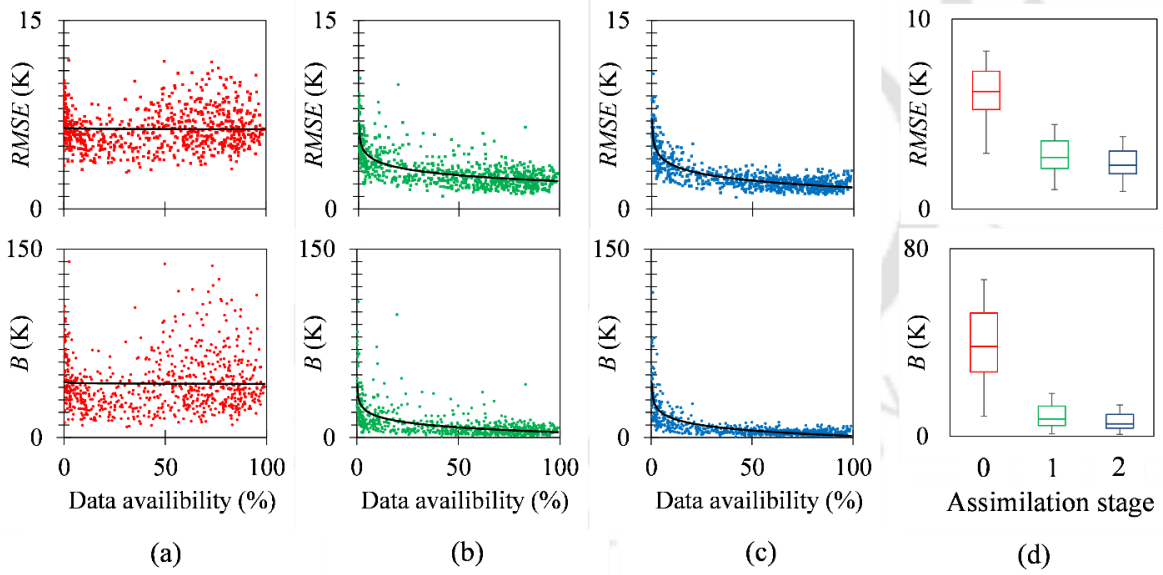

Figure 4.8. *RMSE* and *B* between (a) LST_m and LST_M in stage 0, (b) LST_m and LST_{mT} in stage 1, and (c) LST_m and LST_n in stage 2, with variation in data availability. (d) Reduction in distribution range of root mean square and bias between LST_m and derivatives (LST_M, LST_{mT}, and LST_n) with progress in assimilation stages (pre-reconstruction:0, temporal assimilation:1, and spatial assimilation:2).

4.6. Conclusion

Satellite-based LST is constantly interrupted by atmospheric conditions to produce spatio-temporal inconsistency. The multi-temporal approach is one of the newest methods in reducing this inconsistency. However, the difficulties to apply these methods grow with increase in terrain complexity and diverse physiography. Hence, kernel based spatio-temporal assimilation is used to reconstruct MDOIS LST with the help of GLDAS LST. Comparison of reconstructed LST with original MODIS LST shows ability to restore the spatial variability in complex physiography with high accuracy ($R^2 = 0.98$; $RMSE = 0.6$ K; $B = 0.36$ K). On breaking the error statistics in independent physiographic classes, the method was found to be capable of predicting within reliable ranges ($RMSE \leq 3$K) except at highland regions due to effects of seasonal/perennial snow cover. The spatio-temporal assimilation was also found to effectively encounter cases with severe data deficiency (availability $\leq 10\%$) given that there is uniform spatial distribution in the baseline data (MODIS LST). Comparison of reconstructed LST with ground-based measurements showed positive correlation (average $R = 0.71$) indicating agreement with seasonal variation. The credibility of reconstructed LST is inferred to be as good as MODIS LST to fill the spatio-temporal gaps. The methodology used in this study is concluded as a simple and promising approach for spatio-temporal LST reconstruction in diverse physiographic conditions.

Chapter 5

Surface Water and Energy Budgeting

5.1. Introduction

The Two Water World hypothesis (Renée Brooks et al., 2010; McDonell, 2014; Berry et al., 2018) is an emerging concept which advocate that streams and trees return different pools of water to the hydrosphere. It is expressed by new age researchers that this hypothesis is associated with resilience system of forests during water deficit scenario. Such advancements in hydrological concepts raises the complexity of rainfall-runoff modeling. However, past studies have showed that focusing on dominant processes can help to overcome these complexities rather than capturing unnecessary details (Sivapalan, 2003; Graham et al., 2010). Also, limited observations and knowledge poses big questions that what parameters could be utilized for simplification and overcoming these complexities. Furthermore, can these simplifications be used for poorly gauged watersheds?

Evapotranspiration (ET) and precipitation (P) are most important variables in the water budgeting. Several studies in terrestrial water budgeting use these two variables as decisive parameters to regulate other components of water budgeting. The focus of many of the current researches on terrestrial water budgeting is on the utilization of hydrological products from global hydrological models (GHM). Since, ET estimated from GHM are generally at coarse resolution, breakdown of reliant terrestrial water budget at complex watersheds might not be approximate. It might be well represented by diverse spatial heterogeneity of ET. It is

hypothesized that spatial budget of ET and P might indicate resilience hotspots which could be used to unveil physical process behind hydrological complexity. This chapter summarizes the preparation of consistent long-term ET at high spatio-temporal resolution from satellite data and utilize it for identification of resilience hotspot and inspection of the indicators of resilience to strengthen the hydrological knowledge in complex watersheds of Eastern Himalaya.

5.2. Methodology

The methodology is divided into four parts, viz. input data preparation for energy budgeting, surface water budgeting, resilience hotspot identification and diagnosis to find indicators of resilience in complex watersheds. The details are summarized in this section and the methodology of consistent accessibility to surface water budget is presented in Fig. 5.1.

5.2.1. Data preparation

The reconstructed NDVI and LST time-series data, as discussed in the previous chapters, were used as the primary inputs for the energy balance. These inputs were meant for GMT 0530 or IST 1030 according to the MODIS Terra passing time. The other essential inputs for energy balance, viz. irradiance, albedo and reflectance were processed. GLDAS NOAH provides 3-hourly average of these parameters which were used along with corresponding MODIS products for preparing processed inputs. Table 5.1 shows the appropriate data and processing used to derive these products for surface energy and water balance. For compatibility, all the input parameters were set at a standard of 1 km spatial resolution and 16-daily temporal resolution failing to which were produced by averaging in spatial and temporal dimension

respectively. In addition, annual MODIS LULC data was also used for hydrological efficiency analysis.

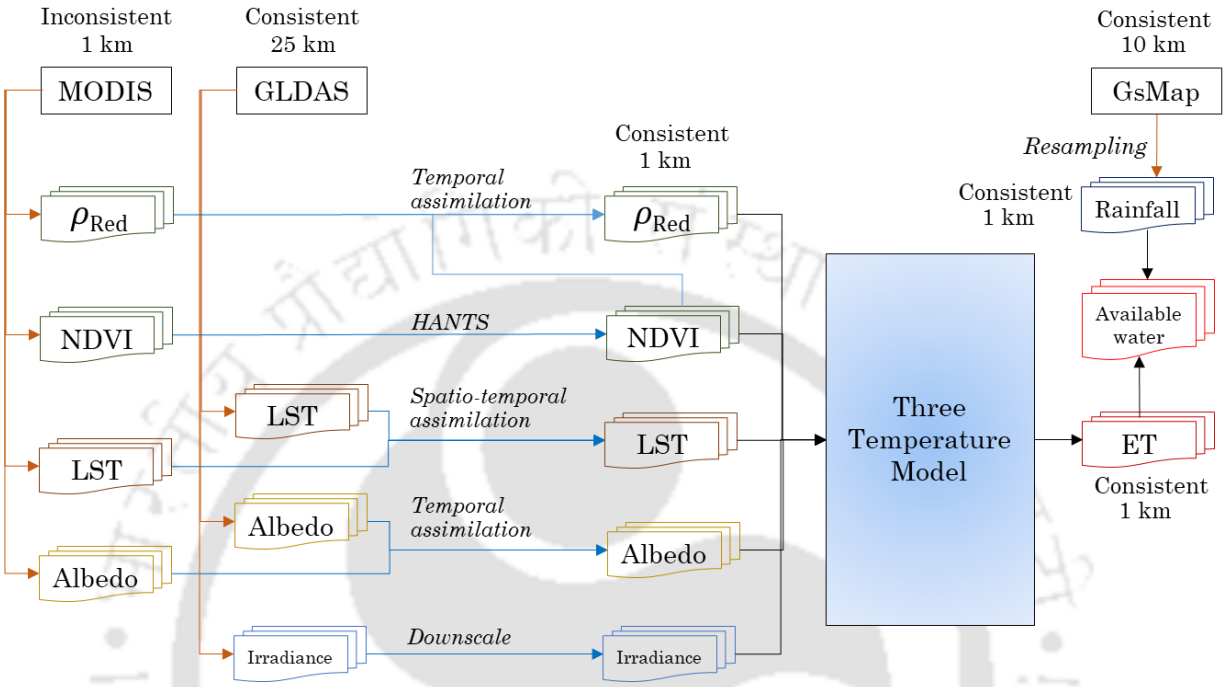

Figure 5.1. Schematic diagram for calculation of water availability.

Incoming solar radiation

Incoming solar radiation at an instance is called irradiance (R_i) and integrated over diurnal time period is called insolation (R_d). It is the source of energy driving the water cycle on Earth (Danehy et al., 2005; Shafer et al., 2005). Hence, it is one of the principal parameters in hydrological applications. Most of the hydrological models use R_i and R_d from latitude-based empirical models. It causes uncertainty in driving force itself due to terrain complexity in the mountainous regions. Complexity of terrain is largely responsible for spatial heterogeneity in R_i (Swift and Knoerr, 1973; Gates, 1980a) which can propagate to R_d based estimates such as energy and water budget (Gutiérrez-Jurado and Vivoni, 2013). Complex watersheds are very much liable to this heterogeneity. Therefore, digital elevation model (DEM) from Shuttle

Radar Topography Mission (SRTM) at high resolution of 90m was used to calculate R_i and R_d thereby overcoming this uncertainty. For this purpose, R_i from GLDAS was resampled at 90m by bilinear cubic convolution and algorithm from Kumar et al. (1997) was used to calculate R_i at DEM surface. The R_i integrated for the entire solar day gave R_d at 90m. Later, these two derivatives were upscaled by spatial averaging from 90m to 1km for application.

Table 5.1. Data and processing of input parameters for energy balance.

Input parameter	Products used	Processing
NDVI	#Reconstructed NDVI	#MOM with HANTS
LST	#Reconstructed LST	#Spatio-temporal assimilation
Irradiance	#GLDAS 3-hourly (0.25) and SRTM DEM (90m)	#Spatial downscaling of irradiance at 90m and spatial averaging at 1km
Insolation	#Irradiance (1km)	#Diurnal integration
Albedo	#GLDAS 3-hourly (0.25) and MODIS 16-daily (500m) [MCD43A3 v006]	#Temporal assimilation
Red band reflectance	#Reconstructed NDVI and MODIS 8-daily (500m) [MOD09A1 v006]	#Temporal assimilation

Albedo and Reflectance

Since, the albedo and reflectance are implication of surface conditions, there is no appropriate method to recover its data gaps. However, GLDAS provides numerically modelled albedo at coarse resolution of 0.25° x 0.25°. To have the albedo at 1 km in resolution, a similar approach to that of LST reconstruction by using GLDAS and MODIS albedo products was followed but limited to only temporal assimilation. It is because unlike LST, there is no evidence of correlation among spatial albedo. Reflectance in red region of electromagnetic spectrum is often an indicator for land surface emissivity (Sobrino et al., 2004). Since, red reflectance is an integral part of NDVI computation, reconstructed NDVI time-series was utilized to predict the occurrence of 16-daily red reflectance at 1km by temporal assimilation.

Rainfall

The GSMaP project (Kubota et al., 2006) is initiated for the development of an advanced microwave radiometer algorithm based on the deterministic rain-retrieval algorithm. The algorithms are developed based on physical models of precipitation including particle-size distribution. The information obtained by the precipitation radar is introduced in order to share a common precipitation model between the microwave radiometers and the precipitation radar algorithms. It uses information from satellites of TRMM, AMSR-E, ADEOS-II, and Defense Meteorological Satellites. The spatial resolution of GSMaP is 0.1° x 0.1° and this data is available from the website maintained by JAXA (https://sharaku.eorc.jaxa.jp/GSMaP/). It was used as the source of precipitation in water budgeting after resampling it to 1km resolution for compatibility.

5.2.2. Surface energy and water budget

Three-Temperature Model (3T model) developed by Tian et al. (2013) was used to calculate spatio-temporally consistent ET at 16-daily scale as shown in Fig. 5.1. Modified algorithm from 3T model used in this work is presented in Appendix-A3. The 3T model produces instantaneous ET (ET_i) which is required to be converted into daily estimations (ET_d). Tian et al. (2013) integrated instantaneous ET to get daily ET as the outcome of a time-based sinusoidal function (Eq. 5.1) proposed by Jackson et al. (1983). This approach is might be applicable to plain regions but unsuitable for complex terrains due to presence of undulating topography. Therefore, a new approach was used to rectify for the heterogeneity of radiation received in mountainous topography. The insolation (R_d) and irradiance (R_i) produced at 1km in the pre-processing steps were used in Eq. 5.2 to give net radiation daily net radiation ($R_{net,d}$) (Samani et al., 2005). Since, R_d was calculated by using variable R_i and incident angle by

Kumar et al. (1997), it was free from any uncertainty caused by topography. An evaporative fraction (F_E) was produced by using the assumption made by Nahry et al. (2011), as shown in Eq. 5.3 where it is believed that F_E remains constant throughout the day. Therefore, it was used in Eq. 5.4 to get ET_d (mm/day).

$$ET_d = \left(2ET_i N_E\right) / \pi \sin\left(\pi t / N_E\right) \quad (5.1)$$

$$R_{net,d} = R_{net,i}\left(R_d / R_{in}\right) \quad (5.2)$$

$$F_E = LET_i / \left(R_{net,i} - G_i\right) \quad (5.3)$$

$$ET_d = 86400 F_E \left[ET_i / \left(R_{net,d} - G_d\right)\right] / L \quad (5.4)$$

where, L is the latent heat of vaporization ($W/m^2/mm$) and G is soil heat flux (W/m^2) with suffixes *i* and *d* representing instantaneous and daily time. G_i is computed in 3T model whereas $G_d \approx 0$ and can be neglected. ET_d calculated represented 16-daily average due to which ET time-series was interpolated by using spline to get daily ET time-series. Later, it was used with daily P time-series for inspecting the water availability as well as other hydrological diagnosis and indications on the mountainous topography of the study area.

5.2.3. Hydrological efficiency and resilience

Spatio-temporally consistent ET and P data at daily level were used to identify storage pattern in the study area. In depth analysis was carried out for six major LULC in the study area, viz. agriculture (CRP), evergreen broad leaf forest (EBF), evergreen needle leaf forest (ENF), mixed forest (MXF), grassland (GRS) and savanna (SVN), in order to understand the control of LULC in surface water budget. The hydrological efficiency (η) was calculated as the proportion of ET and P over a period (water year in this case) as shown in Eq. 5.5.

$$\eta = \sum_{t=1}^{m} ET_t \Big/ \sum_{t=1}^{m} P_t \qquad (5.5)$$

where, *t* represents time step and *m* represents limit of the time period. Eq. 5.5 for yearly time period yields annual water budget. The value η indicated the capability of a particular area to effectively convert P into ET. A value of η greater than 1 indicated the presence of water from storage or some other means. Moreover, it was broken down to seasonal scale to see the pattern of storage activity throughout the year. These storage patterns analyzed over time were anticipated to indicate the hotspots where the stored water is utilized in P deficit scenario. Such areas might exceed the cumulative ET over cumulative P for certain time period. These events will be called hydrological anomaly. High frequency of anomaly indicates the presence of more resilient area. Therefore, analysis of frequency of hydrological anomaly in 15 water years (2001-02 to 2015-16) was done for investigating on resilience of LULC.

5.2.4. Indicators of hydrological resilience

The spatial variation of nine physical parameters were selected and checked for relationship with spatial variation of frequency of hydrological anomaly. These parameters are described in Table 5.2. Since, Eastern Himalayan watersheds are complex in nature, it might be possible that a single parameter might not solely address the complexity of frequency but can associate well in combined effects. Hence, the 1st and 2nd principal components of combination of physical parameters were also diagnosed for relationship with frequency. Again, the range of frequency lied between 1 – 15 and it can be considered as a weak statistic with scaling problems when addressed by linear relationship with a huge variation in the range of indicating parameter. Therefore, both the frequency and parameters were normalized to nullify the scaling effects followed by use 2nd order relationship to get the coefficient of determination (R^2) for

addressing non-linear relationship. This process was conducted for 4th order sub-watersheds to entire watershed and highest mean of R^2 was considered as the strongest indicator to address the resilience.

Table 5.2. List of physical parameters used for investigation as indicators of resilience.

Parameter	Details	Parameter	Details
Ti	#Topographic wetness index (Beven and Kirkby, 1979)	Vg	#Normalized distribution of median NDVI in 16 years
El	#Elevation (SRTM resampled at 1km)	Sa, Si, Cl	#Overall percentage of sand, silt and clay in A, B and C horizon (Hengl et al., 2017)
Sl	#Slope (Calculated from SRTM DEM at 1 km)	Vd	#Regional valley depth (Conrad et al., 2015)
Db	#Depth to bedrock in R-horizon (Shangguan et al., 2017)		

5.3. Results and Discussion

5.3.1. Seasonality

It can be seen in Fig. 5.2 that most of the P is received in the eastern parts of NEH and ASP ecoregions in the study area which comes under watersheds originates in Meghalaya. The monsoon is found to travel from Bangladesh through NEH and ASP to appear as onset at the foothills of HIM ecoregion in the month of June and continues till September. March to May and October to November showed some pre-monsoon and post-monsoon activities respectively while December to February receives negligible P being dry. The HIM ecoregion is found to receive least rainfall relative to the other ecoregions study area. However, the western parts of HIM ecoregion receives a good amount of pre-monsoon activity from April to May. These parts are located as upstream of Brahmaputra River. On the other hand, the

water loss component, ET was seen to rise and decline in the span of June to September (Fig. 5.3). It is interesting that ET in the study area rises and declines according to onset and decay of monsoon. It indicates that ET is highly dependent on available water from occurrence of P. Since, the study is strongly focused on Eastern Himalayan watersheds, HIM ecoregion was analyzed exclusively apart from other ecoregions.

To know the spatial variability in water availability, monthly P was subtracted from ET (Fig. 5.4). Monthly ET exceedance from monthly P indicated the hotspots where water storage is possible. It was found that most parts of the study area gained water by higher P from April to October whereas lost water by higher ET from November to March as a pattern. Nevertheless, spatial variability in ET exceedance indicated control of LULC in the surface water budget. Therefore, it was necessary to analyze this pattern in terms of efficiency of LULC which can clarify the its storage potential.

5.3.2. Hydrological efficiency of various LULC

Fig. 5.5 shows the annual daily median (March to February as water year) of the spatial average of P and ET in 2001-02 to 2015-16 over major LULC in the study area. Selection of annual daily median can reveal the most general scenario which might be occurring frequently throughout the water year. Out of selected six LULC, CRP have anthropogenic controls over water budget whereas other LULC are naturally regulated. It was found that high and low elevated EBF, MXF, and SVN are able to utilize water as ET in November to March which might be stored from water as P in April to October. Also, ENF and GRS which are located at very high elevation are unable to store water from P efficiently. ENF and GRS are located at very high elevation and don't receive as high P as EBF and MXF do receive. Most of the CRP and SVN are lying in the lowlands and receive highest annual P.

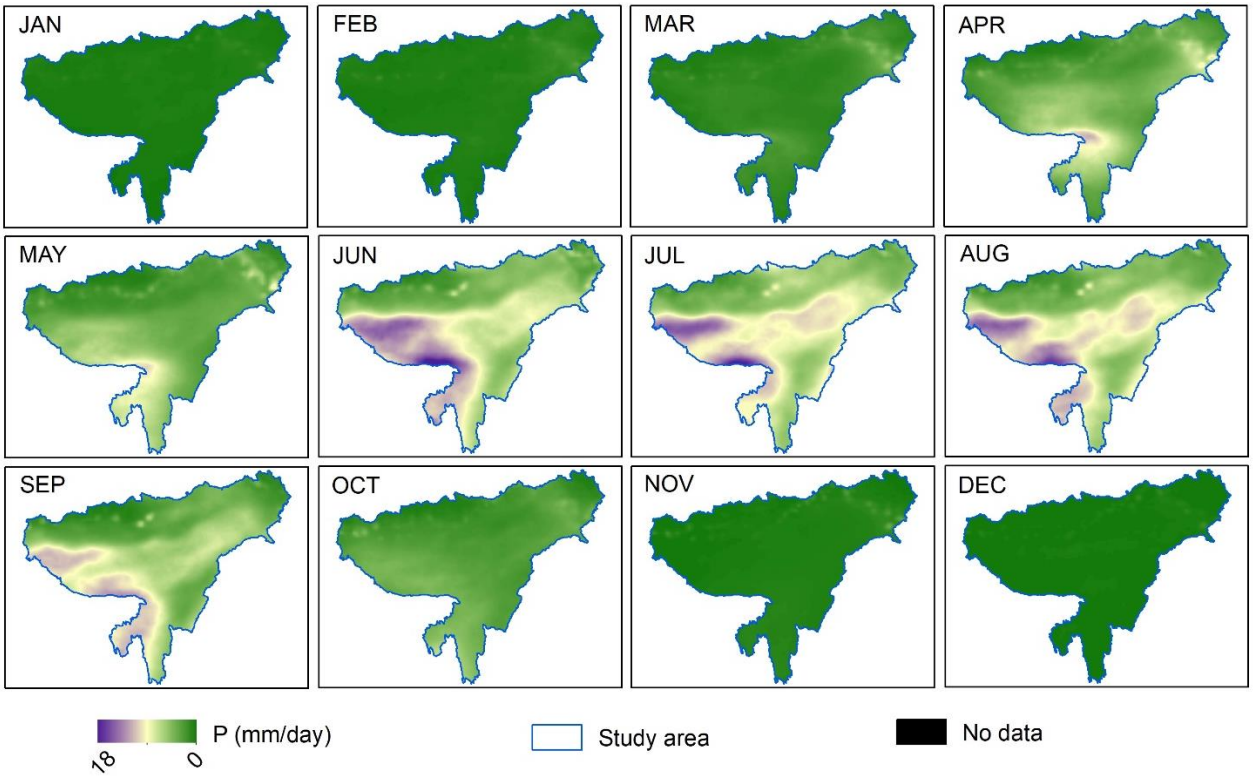

Figure 5.2. Monthly average precipitation (2001 – 2016) in the study area.

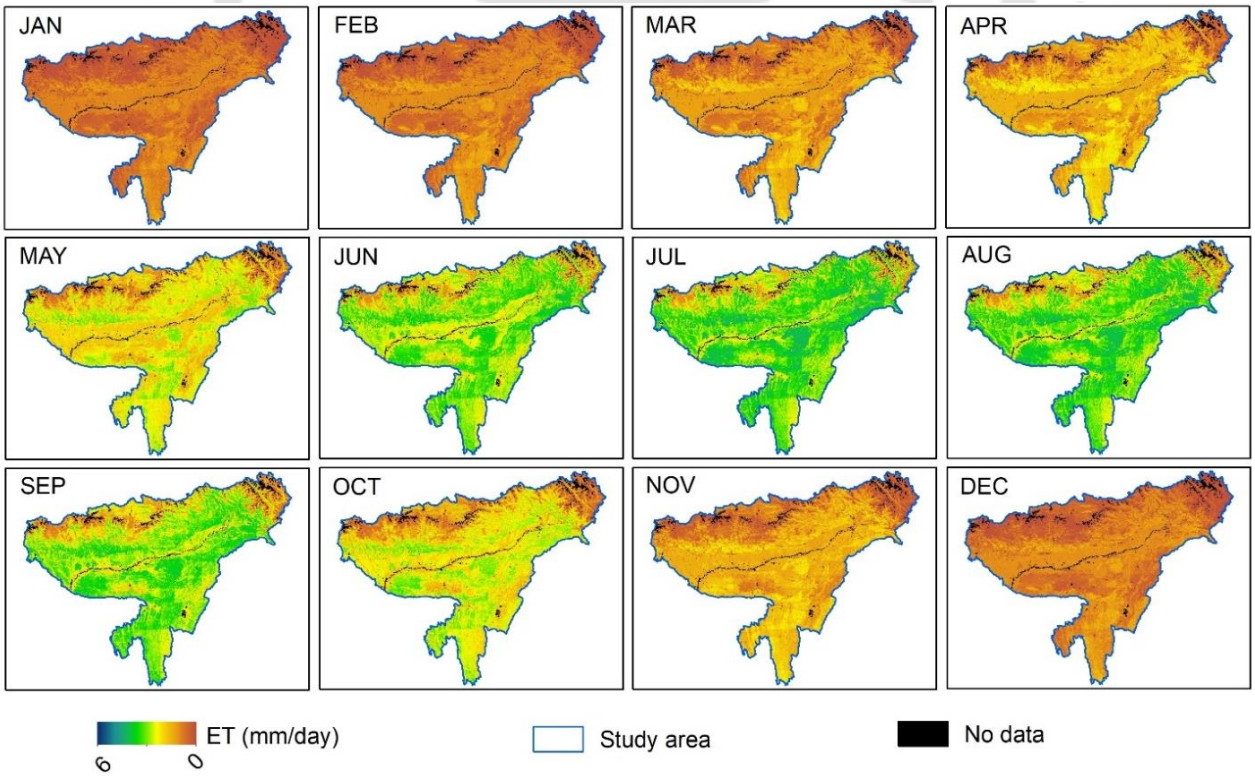

Figure 5.3. Monthly average evapotranspiration (2001 – 2016) in the study area.

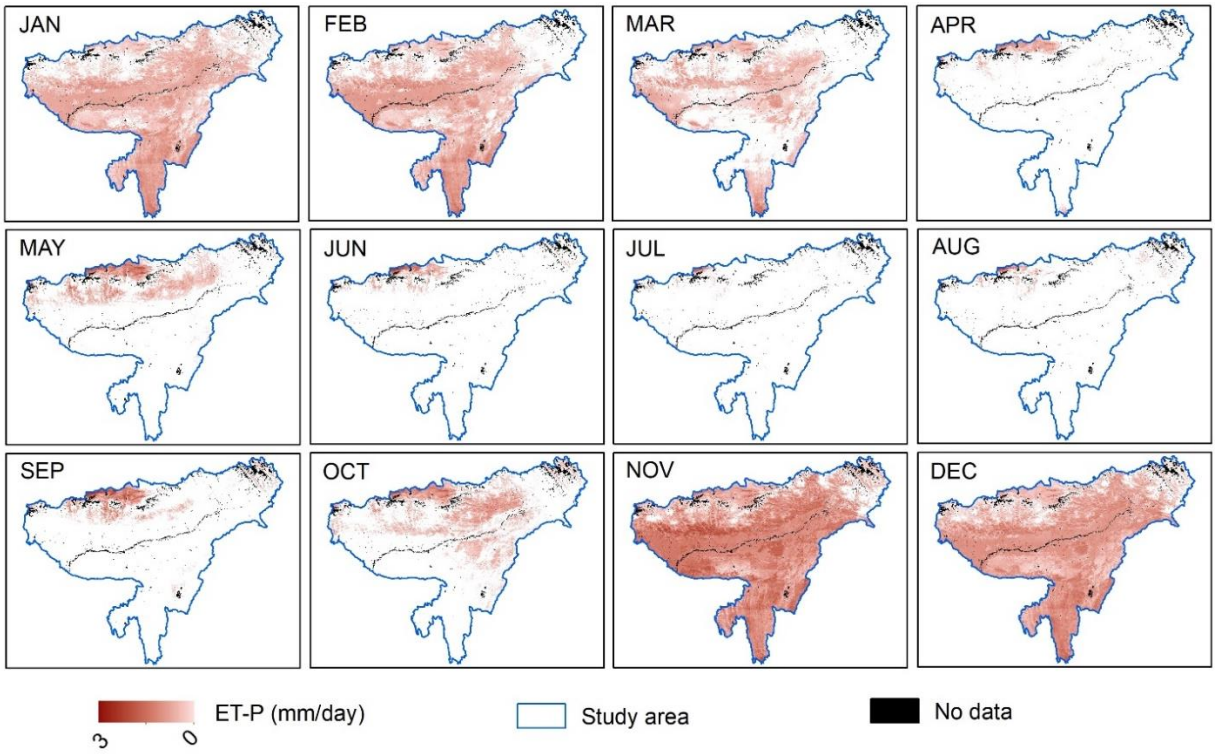

Figure 5.4. Monthly average exceedance of evapotranspiration than precipitation (2001 – 2016) in the study area.

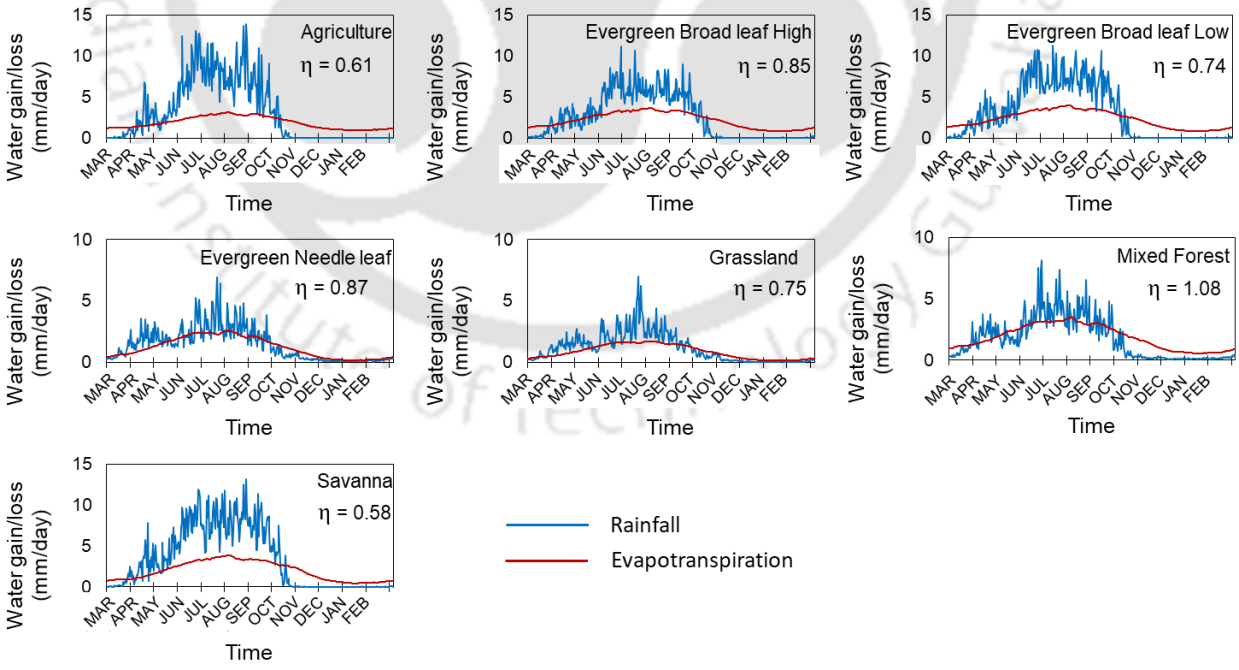

Figure 5.5. Annual daily median (2001 – 2016) of precipitation and evapotranspiration and annual efficiency (η) for various LULC in the study area.

Table 5.3 presents the η for LULC for all the ecoregions at seasonal and annual scales. It is found that almost all LULC in all ecoregions, the η in post-monsoon and dry season increases. CRP shows a stronger increase in dry season of ASP ecoregion indicating the involvement of artificial water supply by irrigation in Rabi agricultural season. Comparison of annual η shows higher values in forested LULC (i.e. EBF, ENF, and MXF) than other classes. Relatively sparse vegetation classes (i.e. GRS and SVN) show lowest η throughout the annual scale. Focusing on HIM ecoregion, it shows that ENF and MXF are most efficient LULC in utilizing water from P throughout the year. The EBF and SVN, particularly situated at the transition between highland and foothills also show good efficiency, mostly in post-monsoon and dry seasons. It is understood that forests have larger η value at annual, post-monsoon and dry seasons which can be associated with better storage capability then sparse vegetation classes like GRS and SVN. Also, CRP shows very high η in post-monsoon and dry seasons similar to other ecoregions indicating influence of artificial water supply. It could be inferred that LULC is an important variable influencing surface water partition due to difference in capability of storage and utilization. Moreover, forest regions have are high hydrological efficient throughout the annual scale.

5.3.3. Resilience hotspots

Analysis of frequency of hydrological anomaly for 15 water years helped to know the likeliness of water storage throughout the year (Fig. 5.6). At annual scale, the frequency indicates likeliness of resilience system. A low frequency indicates no/poor storage system whereas high frequency indicates that the region is most likely to gain a large part of water as storage gained from elsewhere (most likely as preferential storage). The resulting map at annual scale shows clearly three different spatial zones of hydrological anomaly classes viz. Tibetian, Bhutanese

and Indian regions (marked as circles 1, 2 and 3 respectively in Fig. 5.6). It might be due to three different land policies active in those regions. Overall inspection suggests that the highlands in Tibetian region have very high frequency while regions at transition between highland and foothills have moderate frequency. Since, the derived LST in highlands of Tibetian region were erroneous and ET is highly sensitive to LST, the interpretations for these regions is not arisen. However, results in rest of the mountain stretch suggests effective use of stored water from monsoon in the trailing seasons. This analysis was also applied for all the seasons for further understanding of the pattern. It shows that the stored water in monsoon is used most efficiently used in the non-monsoon seasons. Combining the results from Table 5.3, it can be said that forest covered LULC (ENF and MXF) have high efficiency and resilience than other LULC. That means the forest areas have the capability to store water as preferential storage and use it better than sparsely vegetated areas.

Table 5.3. Efficiency (η) of various LULC in the ecoregions of the study area (**Note –** Seasons PR: pre-monsoon; MN: monsoon; PO: post-monsoon; DR: dry; AN: annual).

LULC	HIM					ASP					NEH				
	PR	MN	PO	DR	AN	PR	MN	PO	DR	AN	PR	MN	PO	DR	AN
CRP	**0.69**	**0.36**	**1.23**	**4.12**	**0.53**	0.52	0.29	1.06	5.32	0.43	0.32	0.31	0.87	4.37	0.41
EBF	**0.61**	**0.59**	**0.87**	**1.00**	**0.62**	0.27	0.29	0.53	0.42	0.31	0.60	0.45	1.08	2.35	0.57
ENF	**0.82**	**0.53**	**1.61**	**3.60**	**0.72**	NA	NA	NA	NA	NA	0.53	0.44	1.08	4.54	0.57
MXF	**0.74**	**0.66**	**1.22**	**2.02**	**0.74**	0.41	0.35	0.89	1.34	0.43	0.50	0.45	1.04	2.27	0.54
GRS	**0.56**	**0.39**	**1.03**	**1.85**	**0.48**	0.39	0.34	1.09	1.66	0.41	0.34	0.35	0.94	2.77	0.42
SVN	**0.80**	**0.56**	**1.36**	**0.95**	**0.65**	0.38	0.24	0.78	2.60	0.33	0.14	0.16	0.37	0.68	0.17

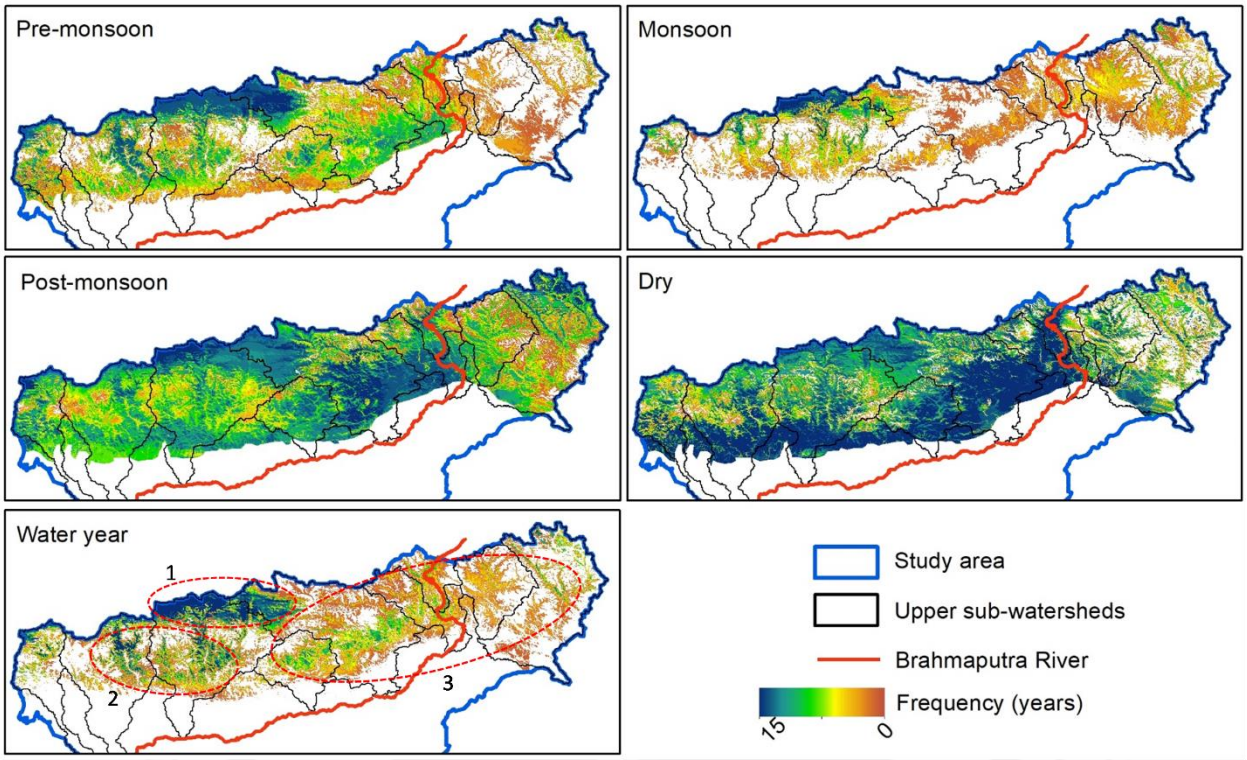

Figure 5.6. Frequency of hydrological anomaly in the study area. (**Note:** The circles marked 1, 2 and 3 represents the Tibetian, Bhutanese and Indian regions respectively).

5.3.4. Influence of forest on hydrologic resilience

The principal components of 9 listed physical parameters in combination was investigated with frequency of hydrological anomaly at 4^{th}, 5^{th}, and 6^{th} order sub-watersheds along with entire watershed and their mean R^2 values are shown in Fig. 5.7. Due to limited range of frequency, low R^2 values were expected as well as seen, however there were differences among various combinations of parameters. Therefore, to analyze significant parameters as indicators of hydrological anomaly, top 10 combinations with highest R^2 values were listed. None of these watersheds showed best relationship with any of the parameters solely which advocates for their complexity. The watersheds Dibang and Siyom were found as most complex watersheds

with very low R^2 values. Gangadhar, Lohit and Manas were moderately complex and Teesta, Kameng and Subansiri were least complex. A particular repeating combination of parameters is expected to address the resilience due to influence on the frequency of anomaly. It is interesting that in most of the watersheds the combination of hillslope parameters (Vg, Db) overcame topographic parameters (Ti, El, Sl), soil parameters (Sa, Si, Cl) and regional parameter (Vd). For eg. in case of Subansiri, the combination (Vg, Db) is seen most of the times in top 10 principal components list. It means that Subansiri watershed have storage systems that is mostly controlled by vegetation fraction and depth to bedrock in the hill slopes. On the other hand, Siyom watershed could be seen to be dominated by topographic parameters (El,Sl). The Kameng watershed, which is attached to the boundary of Subansiri watershed shows control of combined vegetation fraction and soil. Such contrast in combinations suggests that the hydrological resilience is basin dependent and it is difficult to be associated with an universal indicator. From regional modeling perspective, it was concluded that the storage system of Eastern Himalayan watershed is mostly controlled by vegetation fraction indicating forest cover and bedrock depth indicating higher sub-surface storage in the soil-bedrock interface. It can be true because the forests have evolved according to physiography and climate in natural conditions over millions of years, which can alter the depth of soil formation and storage systems. These two parameters are concluded as key variables that can indicate the hydrological resilience in many of the Eastern Himalayan watersheds.

Figure 5.7. Coefficient of determination (R^2) between principal component and frequency of hydrological anomaly. (Ti: topographic index, El: elevation, Sl: slope, Db: depth to bedrock, Vg: vegetation fraction, Sa, Si & Cl: percentage of sand, silt and clay respectively, Vd: regional valley depth).

5.4. Conclusion

Limitation of observations in poorly gauged watersheds of Eastern Himalayan region implies questions on understanding of hydrological complexity. Using consistent input variables for energy balance helped in retaining consistent spatio-temporal ET data. Using consistent ET at high resolution with precipitation data (P) at high resolution revealed the location of hotspots where annual ET exceeds annual P to be called as hydrological anomaly. High frequency of hydrological anomaly indicates hydrological resilience of those locations to P deficit per year. It is confirmed that hydrological resilient areas are mostly forest by hydrological efficiency test for several LULC. Hence, it is hypothesized that the additional water required for ET in hydrological resilience could be in form of unknown preferential storage in forest areas. Also, analysis for 2nd order relationship of hydrological resilience with several selected physical parameters along the spatial extent shows that it is directly proportional to vegetation fraction and bedrock depth. Therefore, vegetation fraction and bedrock depth can be used as indicators for hydrological resilience. However, there can be contrasting influence of different parameters in the watersheds of same ecoregion. These observations are useful for knowledge building and could be used in assimilation strategies for development of efficient process-based hydrological model.

Chapter – 6

Hydrological Modeling for Hilly Watersheds

6.1. Introduction

The hilly watersheds in humid tropical or sub-tropical regions are dominated by hillslope process where a threshold-based runoff generation is frequently seen (Williams et al., 2002; Das et al., 2014). This threshold is generally not encountered in hydrological modeling, but it is kept intact as a calibrated quantity. Researchers have stated the reason for occurrence of this threshold is due to presence of macropores (Torres et al., 1998; Shougrakpam et al., 2010; Sharma et al., 2013; Sarkar et al., 2015) and often varies with LULC depending upon vegetation (Niehoff et al., 2002; Shougrakpam et al., 2010; Bachmair et al., 2009; Mayerhofer et al., 2017). However, it is also informed in many research outcomes that the soil-bedrock interface is an important factor in hillslopes (Dusek and Vogel, 2016) and have controls over threshold (Graham et al., 2010, Janzena and McDonnell, 2015). These findings agree with the outcomes of analysis form many Eastern Himalayan watersheds in the previous chapter. In this chapter, a process-based model from various evidences and data is developed which is applied on Subansiri watershed as a demonstration. Graham and McDonnell (2010) derived the threshold from relationship of long-term rainfall, evaporation and water budget to develop a macroscale hydrological model in a fill and spill approach. The developed model is having a similar approach. This model is formulated based on the understanding from previous chapters and several related works.

6.2. Macropores

The Macropores are large soil pores in soil, usually greater than 0.08 mm in diameter which allow free movement of air and water by gravity (Chouksey et al., 2017). It is an essential part in hillslope hydrology which is generally neglected in hydrological modeling (Beven and Germann, 2013; Weiler, 2017). The presence of macropores changes the dynamics of runoff generation in a contrast manner with the concepts of current hydrological models. There are basically two types of macropores, main bypass (MB) (Hoogmoed and Bouma, 1980) which is continuously interconnected with increase in depth and internal catchment (IC) (Bouma and Dekker, 1978; Van Stiphout et al., 1987) which is not connected. The MB is first to abstract water out of a precipitation event and it is responsible for direct contribution to the ground water. The IC are the type of macropores which stores water, and hence is named after its purpose. The amount of water to be abstracted by macropores is computed based upon the macropore geometry which can vary according to different LULC (Das et al., 2014).

6.3. Methodology

A list of various data used for the model setup and simulation is shown in Table 6.1 which was run for Subansiri watershed as a demonstration. Apart from this data, monthly total dependable flow volume observed from (1996 – 2004) was procured from Central Water Commission, India (CWC). The model description is given below.

6.3.1. Model concept

The water balance model for poorly gauged complex watersheds of Eastern Himalaya was developed from physical-based concepts in a semi-distributed fashion. Flow diagram of the model is given in Fig. 6.1. It shows that the model has three categorical inputs viz. daily initial

conditions, daily forcing data and water balance parameters. The daily initial parameters are the various storage variables which define the antecedent condition of storages. Daily forcing files consists of daily incoming and outgoing water flux (P and ET respectively) and leaf area index (LAI) for calculation of interception loss. The water balance parameters are storage restricting constants dependent upon soil texture i.e. field capacity (θ_{FC}) and wilting point (θ_{WP}), and macropore volumes of IC and MB domains (V_{IC} and V_{MB}). Apart from these parameters, another additional set of parameters are user defined which is calibrated according to the observed data. These parameters are threshold (T_{sur}) and slope (S) values used in surface runoff generation and saturated hydraulic conductivity (K_{sat}) controlling the daily base flow from perched aquifer.

Basic spatial and temporal resolution for this model was set at 1 km and 1 day respectively. It was assumed that each grid at this scale represents a micro-watershed with inherent properties. These properties were defined as the volumetric capacity for storage according to the heterogeneity of water balance parameters (LULC, soil texture) as described in sub-surface characterization section. Also, due to data unavailability, the storage capacity of perched aquifer was assumed to reach a maximum thickness of 1m.

6.3.2. Sub-surface characterization

This model is inspired from the of concepts of Soil–Water–Atmosphere–Plant (SWAP) model (Kroes et al., 2003; van Dam et al., 2008) and water balance with fill and spill approach (Graham and McDonnell, 2010). Generally, the depth of entire soil matrix is considered equal to depth till saturation zone. However, this model is focused on the top horizon where three-layer system is considered (A, B and C horizons). The A-horizon is the root zone depth of various LULC and it was obtained from Table 6.2, which is modified from Das et al., (2005)

for the compatibility of MODIS LULC. The B- and C-horizons were considered to stand at depth of 50 cm and 150 cm from the top of the surface.

Table 6.1. Data used in the hydrological model setup and simulation. (**Note:** NDSI represents normalized difference snow index which is calculated as the normalized ratio of the difference in surface reflectance in green and shortwave infrared bands).

Variable name	Data used	Source
# DEM	#SRTM 90m	# https://dwtkns.com/srtm/
# Soil texture, field capacity, wilting point & bedrock depth	#SOILGRIDS	# ftp://soilgrids:soilgrids@ftp.soilgrids.org/
# LULC	#MODIS annual LULC	# https://lpdaac.usgs.gov/
# P	#GsMap daily precipitation intensity	# https://sharaku.eorc.jaxa.jp/GSMaP/
# ET	#16-daily ET from 3T-model	# Interpolation from 16-daily ET to daily ET by spline
# NDSI	#8-daily reflectance from MODIS product	# Interpolation from 8-daily NDSI to daily NDSI by spline
# T_{max} and T_{min}	#GLDAS temperature	# https://disc.gsfc.nasa.gov/
#Vegetation fraction	#16-daily NDVI	# Median of 16 years NDVI prepared by using MOM+HANTS followed by spatial normalization between 0 to 1

The macropore volume fraction volumetric proportion of the two domains, main bypass (V_{mb}) and internal catchments (V_{ic}) per grid is calculated by using Table 6.1 and its detailed description of calculation procedure is given in the Appendix-A4. The volume of soil matrix was limited between field capacity (θ_{FC}) and wilting point (θ_{WP}) multiplied by the depths of corresponding horizons as acquired from SOILGRIDS data. The water balance schemes (water gain and loss) in the soil matrix were carried out from top to bottom in order. The bedrock was considered beyond C-horizon where the depth of perched aquifer can't overlap with C-horizon.

Table 6.2. Parameters of macropore geometry for various LULC (modified for MODIS LULC from Das et al., 2014).

Parameter	Description	LULC							
		ENF	EBF	MXF	SVN	SRB/ VGF	CRP	GRS	WTR/ WTL/ URB/ SNW
AH (cm)	# Bottom of A Horizon	-10	-4	-10	-4	-4	-2	-20	NA
Z_{ic} (cm)	# Bottom of IC domain	-30	-14	-30	-13	-13	-20	-30	NA
R_{ZAH}	# Cumulative frequency distribution at Bottom of A-Horizon	0.99	0.89	0.96	0.76	0.67	0.73	0.78	NA
m	# Shape factor	1.52	0.8	1.52	0.97	0.93	1.12	1.19	NA
V_{st0} (cm^3/cm^3)	# Static macropore volume fraction at the top soil surface	0.06	0.06	0.09	0.04	0.06	0.03	0.06	NA
P_{ic} (cm^3/cm^3)	# Volumetric proportion of IC domain	0.83	0.82	0.87	0.84	0.85	0.71	0.05	NA
d_{pmax}	# Maximum polygon diameter	32.07	32.32	35.95	33.2	34.04	17.59	32.39	NA
d_{pmin}	# Minimum polygon diameter	12.11	12.56	10.65	11.81	11.59	15.86	12.03	NA

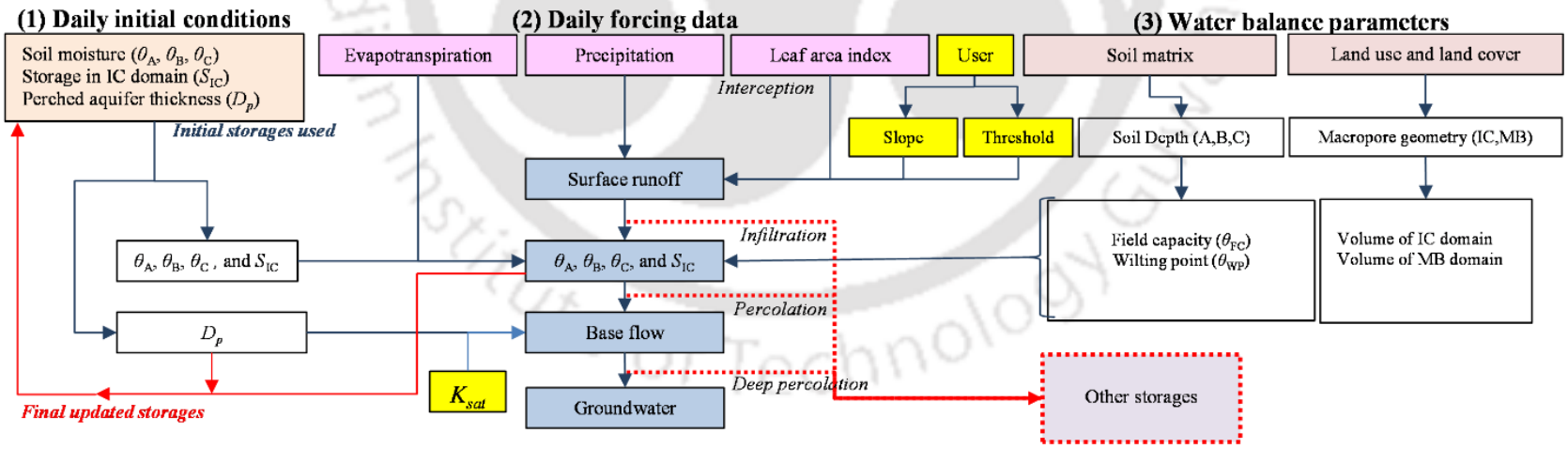

Figure 6.1. Schematic flow diagram of the developed model for surface and sub-surface water balance in hilly watersheds.

6.3.3. Micro-watershed characterization

Each grid in the model was assumed as a theoretical micro-watershed. These grids have variable threshold of runoff generation (T_{sur}) and hydraulic conductivity (K_{sat}) of the perched aquifer in spatial dimension. These spatial variabilities were supposed to affect the runoff volume in each micro-watershed. Therefore, T_{sur} and K_{sat} maps were produced to characterize the micro-watersheds. In the previous chapter, vegetation fraction (Vg) and depth to bedrock (Db) were found as key indicators for hydrological resilience. Here, it is assumed that high resilient areas have higher threshold values than low resilient areas due to more likeliness to store water in preferential storage. Hence, the 2nd order relationship between normalized Vg and Db with hydrological resilience (Fig. 6.2 showing for Subansiri watershed) is used as a weight factor to distribute T_{sur} in spatial extent within a range of T_{sur} ± 25%. The K_{sat} map was produced by using conceptual method developed by Luo et al. (2010) and it is described in the Appendix-A5.

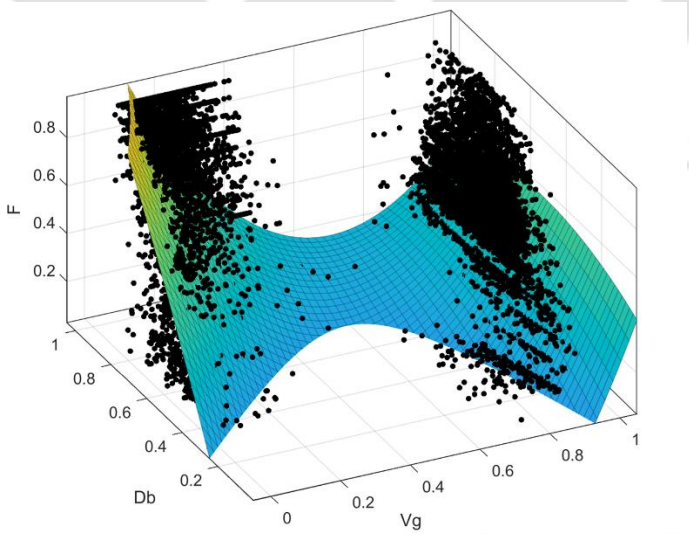

$$f(x,y) = -0.644 + (-1.525x) + (2.42y) + (2.42x^2) + (-1.807xy) + y^2$$

Figure 6.2. Second order polynomial relationship of normalized Vg and Db with hydrological resilience in Subansiri watershed where *x* and *y* represent normalized Vg and Db respectively.

6.3.4. Water flow and balance

Fill and spill approach

The fill and spill approach (also known as source and sink) was serially ordered according to observations of various studies. The water depth from P reaches to the surface after an interception loss due to vegetation canopy as shown in Eq. 6.1. After reaching the surface, water depth is computed for surface runoff generation (Eq. 6.3). It is followed by division of remaining water depth into different sub-surface domains (soil matrix, IC and MB). Most of the studies state that the macropores are first to draw incoming water on hillslopes followed by soil infiltration (Sarkar and Dutta, 2015; Sarkar et al., 2015). However, these studies were done at hourly level with P intensity. The daily level model needed a different approach conferring to data availability. Therefore, water depth remaining after surface runoff is divided according to proportion of antecedent volumetric capacity of sub-surface domains to intake water. The proportion of water into MB domain is directly contributed to purged aquifer thickness (D_p limited to its maximum capacity of 1m and any exceedance is considered as deep percolation). D_p is used to calculate runoff as base flow from perched aquifer (Eq.6.5) to be added with surface runoff to get the total runoff from a grid (Eq. 6.2). Both gain and loss in volumetric storage in soil matrix driven by forcing parameters was calculated from top to bottom order (A- to C-horizon).

Total Runoff

The total runoff scheme comprised of two elements in the areas with no snow cover, i.e. sum of runoff from surface and base flow. The surface runoff generation rate changes according to seasonal variations where for a same P, dry and wet seasons are observed to produce low and high runoff respectively (Das et al., 2014). Hence, a slope variation of 0.3 to 0.5 was assumed

to replicate the seasonal runoff behavior of dry to wet conditions which are standardized according to variation of antecedent moisture conditions of A-horizon ($\theta_{A,WP} - \theta_{A,FC}$) as shown in Eq. 6.4.

$$P_{sur} = P - (C \times LAI) \tag{6.1}$$

$$R = R_{sur} + R_{bf} \tag{6.2}$$

$$R_{sur} = (S \times P_{sur}) - [A(\theta_{A,FC} - \theta_A)] + T_{sur} \tag{6.3}$$

$$S = \{[(\theta_A - \theta_{A,WP}) / (\theta_{A,FC} - \theta_{A,WP})](0.5 - 0.3)\} + 0.3 \tag{6.4}$$

$$R_{bf} = \left(8K_{sat}\, pD_p{}^2 L^2 / Ar\right) \exp\left[-\frac{\pi^2 K_{sat}\, pD_p L^2 t}{n_e Ar^2}\right] \tag{6.5}$$

where, P and P_{sur} are the rainfall depth falling and reaching the ground surface respectively, C is coefficient of interception (0.05 – 0.2 mm), LAI is leaf area index computed from NDVI (Eq. A3.17), R is total runoff depth and suffixes *sur* and *bf* represents that originating from surface and base flow respectively, $T_{sur,}$ is threshold of surface runoff generation, S is the variable slope between 0.5 to 0.3 according to antecedent moisture condition in A-horizon (θ_A) between the corresponding wilting point ($\theta_{A,WP}$) and field capacity ($\theta_{A,WP}$), K_{sat} is the saturated hydraulic conductivity of perched aquifer, p is constant adjustment parameter (0.3465), D_p is the depth of perched aquifer, L and Ar are length of all tributaries and area of micro-watershed respectively, n_e is effective porosity (0.35 - 0.4), and t is time. In the snow-covered areas, runoff was calculated as snowmelt by using WINSRM software (Martinec et al., 2008) with inputs as daily precipitation, maximum and minimum temperature data (Table 6.2) and critical temperature assumed at 1°C.

6.3.5. Calibration and validation scheme

The observed total flow volume data from June to May of 2004 – 2005 was used for calibrating the model threshold values against highest Nash–Sutcliffe model efficiency coefficient (NSE) values (Eq. 6.6) and it was simulated for years 2001 – 2016.

$$\mathrm{NSE} = \sum (Q_m \times Q_o)^2 \Big/ \sum \left(Q_m \times Q_{avg}\right)^2 \tag{6.6}$$

where, Q is the flow volume represented by suffixes m, o and avg as modelled, observed and average values respectively. Due to unavailability of observed data in simulation period, water level data from Jason-3 altimeter from Jul-2008 to Feb-2016 was downloaded from the website (http://ctoh.legos.obs-mip.fr/data/hydroweb/) for indirect comparison at monthly scale. The location of both the CWC observation location and Jason-3 virtual station is given in Fig. 6.3. The selected virtual station from Jason-3 is located on the Brahmaputra River after confluence of tributary of Subansiri watershed and before the confluence of any other watersheds in the downstream. Therefore, it was expected to be most influenced by flow from Subansiri watershed.

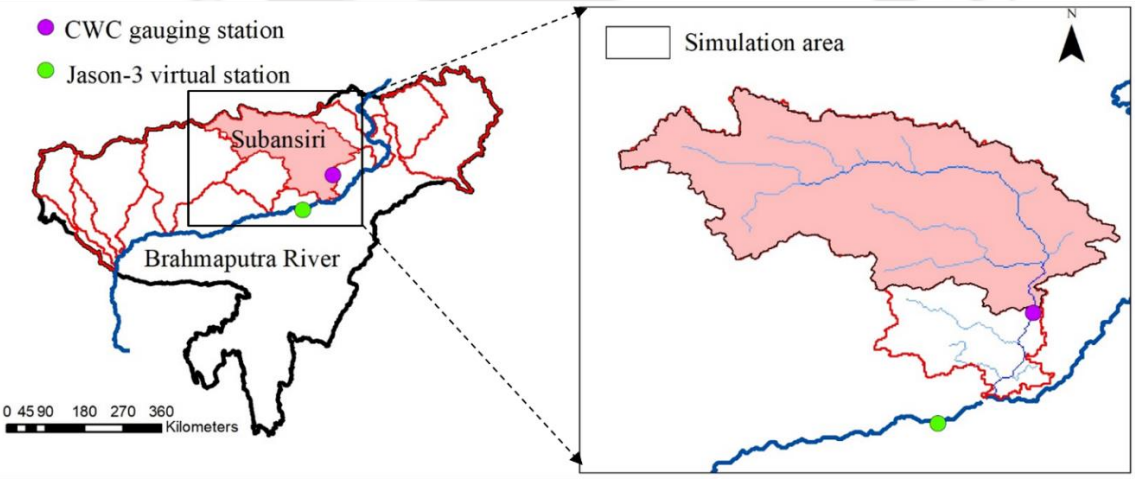

Figure. 6.3. Locations of CWC gauging station and Jason-3 virtual station used for comparison with model outputs.

6.4. Results and Discussion

6.4.1. Surface and sub-surface flow

The calibration scheme focused on adjustment of an overall threshold value of entire watershed with best NSE values. Fig. 6.5 shows the observed and simulated monthly total flow volume of Subansiri watershed. The simulations were started from a threshold value of 1cm, 2.5cm, 5 cm, 7.5 cm, and 10cm. The simulated total volume comprised of added surface runoff, sub-surface runoff and snow melt from the model. However, it was noticed that the used K_{sat} values were producing low base flow computed from Eq. 6.5. Therefore, the K_{sat} was also brought into calibration scheme by multiplying with a factor of 10^x (x = 1, 2, 3, 4 and 5) along with the combination of thresholds. Simulated range of monthly flow volume resulted from the combinations of K_{sat} and threshold is shown as calibration range in Fig. 6.4. The optimum values for threshold of 1 cm ± 25 % and K_{sat} at a much higher order (≈10^4) than original K_{sat} produces highest NSE = 0.83 (Table 6.2).

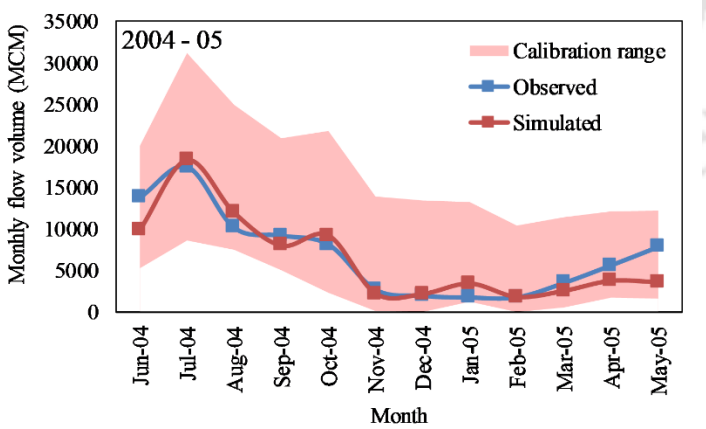

Figure 6.4. Calibration of model monthly total flow volume of Subansiri watershed.

This value of optimum threshold is approximately close to that observed by Das et al. (2017). Also, the flow velocity is observed to attain much higher order than theoretical values due to

influence of macropore network (Graham et al., 2010). Agreement of Subansiri case study with these two previous works can be interpreted as strong influence of preferential flow on runoff generation.

Table 6.3. NSE values for various simulation schemes in calibration.

Threshold (cm)	Multiplication factor to K_{sat}					
	10^0	10^1	10^2	10^3	10^4	10^5
1.00	0.56	0.56	0.57	0.62	**0.84**	-3.48
2.50	0.02	0.03	0.04	0.13	0.59	-2.72
5.00	0.00	0.01	0.02	0.11	0.58	-2.75
7.50	0.00	0.01	0.02	0.11	0.58	-2.77
10.00	0.00	0.01	0.02	0.11	0.59	-2.78

The simulated monthly flow volume is shown as a comparison against monthly dependable flow volume in Fig. 6.5a. It shows that the calibrated T_{sur} and K_{sat} produces monthly flow volume within reasonable ranges. It is seen to that the model over predicts in peak monsoon period but captures the trend of onset and dissemination of flow. It might be due to limited data utilized for calibration of T_{sur} and K_{sat}. But precise calibration can improve the model for better predictions. Due to unavailability of observed data in simulated period, another indirect comparison with monthly water level data (Jul-2008 to Feb-2016) from Jason-3 altimeter shows a good relationship with monthly average flow volume simulated by the model (Fig 6.5b). Generally, this type of relationships is established for location-specific discharge. However, the developed hydrological model is a water balance model due to which the outcome is limited in terms of flow volume. It can be utilized by an efficient routing scheme for mountainous topography in the future.

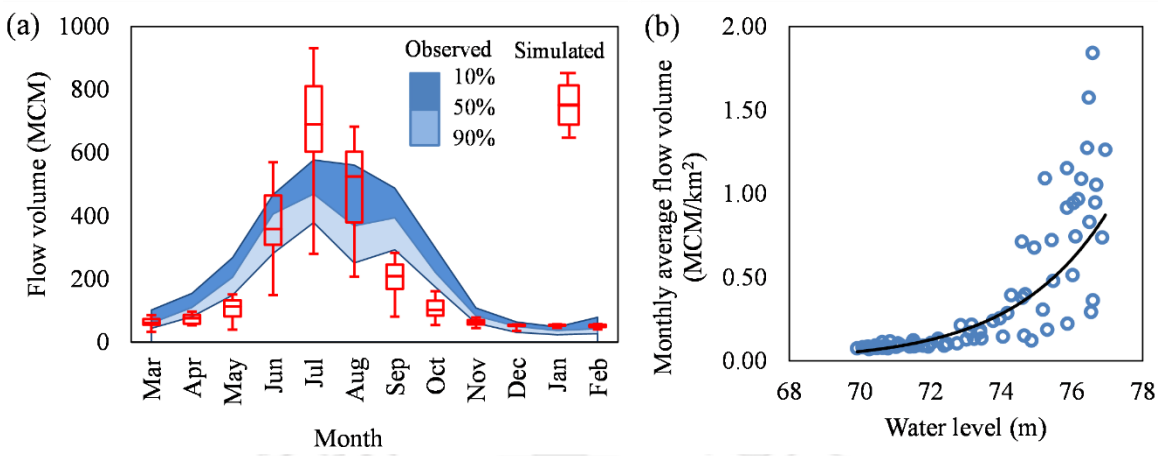

Figure 6.5. (a) Comparison of observed monthly dependable flow volume (1996-2006) and simulated monthly flow volume (2001-2016). (b) Comparison between simulated monthly average flow volume and monthly average water level (Jul-2008 to Feb-2016).

The various inputs and outputs of water balance model simulated from 2001 – 2016 for Subansiri watershed is shown in Fig 6.6. The watershed is divided into two regions, upper and lower, to decode the outcomes of the model. The midlevel regions are neglected because majority of the area is covered with snow. It shows that most of the runoff volume is generated at both upper and lower regions. The reason for upper regions to produce good runoff is low infiltration fraction because low base flow is observed. However, the lower regions have a high base flow contribution and high average soil moisture which indicates that preferential flow is active in this region. The ET is enormously high in the lower regions even if the precipitation in some zones is less. This happens due to presence of forest cover as suggested in the previous chapter. Overall performance of the model is found to deliver the objectives of semi-distributed models as far as spatial variability is concerned.

6.4.2. Runoff response

It is shown by several research experiments that the events of runoff generation on surface is rare in hillslopes (Sarkar et al., 2015). The outcomes of water balance model were analyzed for the number of runoff events which occurs on the surface. Fig. 6.7 shows the percentage of surface runoff generation out of all rainfall events between 2001 – 2016 in Subansiri watershed. It is found that highest surface runoff generation ratio is at the snow-covered areas and near the outlet of the watershed where lowland starts. The interested region i.e. forests, and grassland regions show this proportion ranging between 0 – 5 %. Most of the study area is covered with grassland in the upper regions and forest in the lower regions. As these regions are noticed to have high average base flow runoff but low surface runoff generation ratio, it confirms preferential flow activities to contribute in total runoff volume. Since, the developed model includes observation on macropore geometry form experimental sites at various LULC in Eastern Himalayan region, the macropore dominance in the hillslopes is convinced.

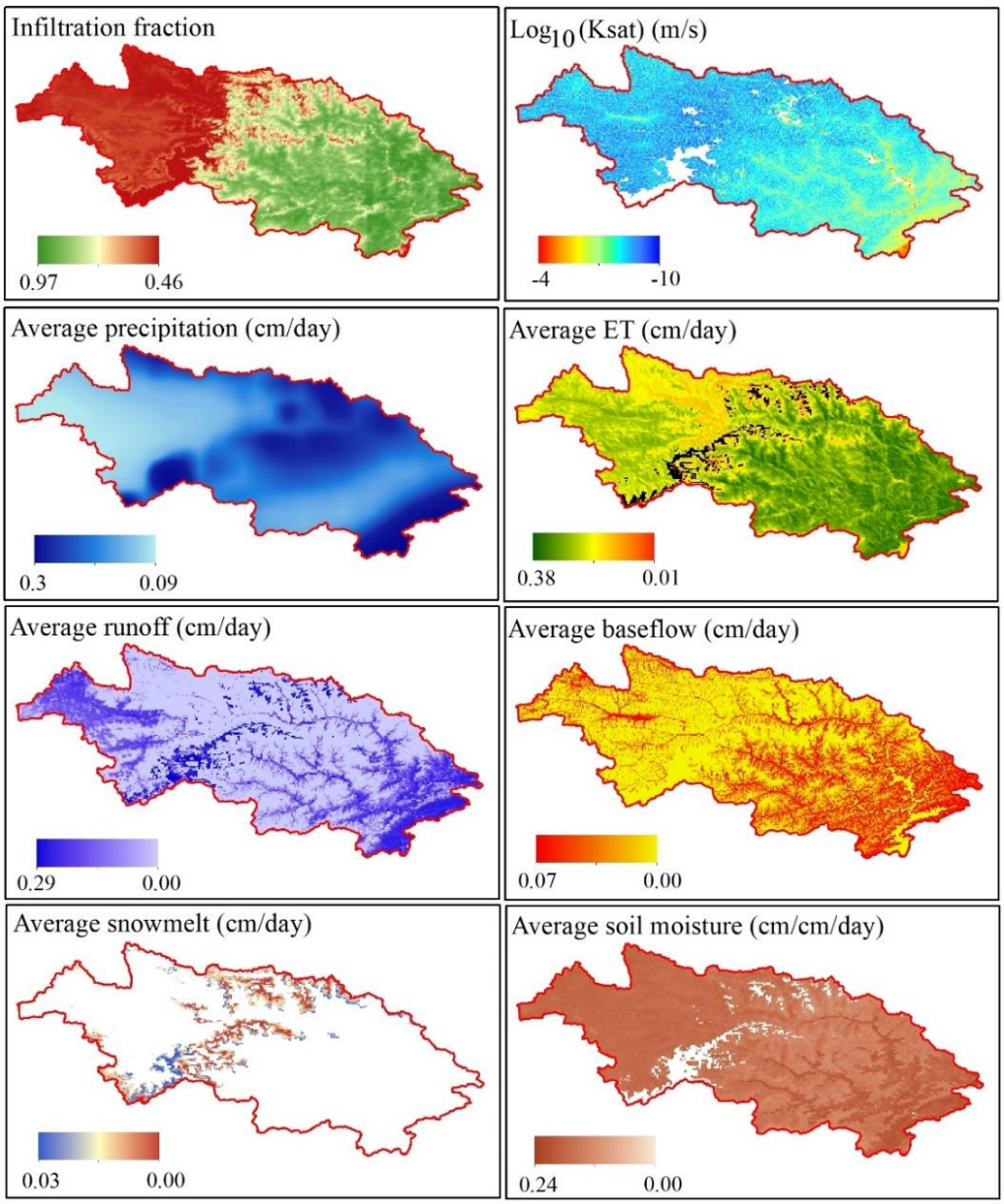

Figure 6.6. Input and output of water balance simulation from 2001 – 2016 in Subansiri watershed.

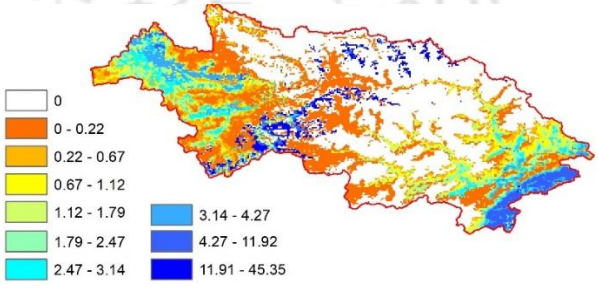

Figure 6.7. Surface runoff generation ratio calculated from the GsMap precipitation and outputs of calibrated model simulation for 2001- 2016.

6.5. Conclusion

Macropores are essential factor in hillslope hydrology which is mostly neglected in modeling works. The presence of macropores can change the dynamics of runoff generation scenario in hilly watersheds. Hence, a process based semi-distributed model was developed incorporating the findings of previous experiments and works in the Eastern Himalayan region. Being limited to volumetric predictions of runoff, the model required careful calibration of threshold and hydraulic conductivity from the basin outlet. Even if the is model developed purely based on theoretical concepts and observations, it indicated the presence of active preferential flow from time to time. During calibration with observed data in the basin outlet, a much higher order saturated hydraulic conductivity (approximately than 10^4 times more) than the theoretical hydraulic conductivity was found to have better NSE value of 0.84. It indicates the presence of preferential flow which is known to be responsible for increasing the sub-surface flow velocity. Also, the surface water balance by using the model with calibrated values show low surface runoff generation ratio but high base flow volume in forests. It indicates towards the dominance of macropores which lead a proportion of the infiltrated water volume through active preferential flow. Yet, there are limitations in the developed process-based hydrological model for water balance. Like any other physical model, the uncertainties are input data dependent. Several other models working with numerical modeling overcomes such uncertainties. However, this model has and advantage of semi distributed outputs. Also, the model is limited to surface and sub-surface (limited to a small depth) water budgeting. It can be improved further with more observation and experimentation. As far as rainfall-runoff modeling is concerned, it can be considered as a reasonable model specialized in hilly watersheds of Eastern Himalayan region.

Chapter 7

Conclusion and Recommendations

7.1. Brief Review of the Work Done

Terrestrial energy and water budgeting in poorly gauged, complex and inaccessible watersheds is a difficult task. It takes consistent monitoring over a period to understand and interpret hydrological processes involved in water balance. The evolution of energy balance models has advanced to a stage where minimum in-situ data can be tolerated with use of satellite derived remote sensing data. However, inconsistency in satellite data propagates the produces inconstancy in observation and understanding of the hydrological process. Satellite remote sensing operational in visible range of electromagnetic spectrum are used to monitor many land surface variables including those which affects hydrological processes. The land surface vegetation condition and temperature are two of the essential variables used in estimating water loss or evapotranspiration (ET). Satellite technology have limitations in acquisition of these variables during clouded situation. The Eastern Himalayan watersheds located in Northeast region of India are one of the frequently clouded regions in the world. The data gaps in land surface variables were successfully reconstructed. Land surface vegetation condition was reconstructed by a novel algorithm called moving offset method (MOM). Land surface temperature was also reconstructed by using an innovative kernel-based spatio-temporal assimilation of satellite data at high resolution with a global macroscale temperature product from Global Land Data Assimilation System (GLDAS). These reconstructed data with other variables were fed in an energy balance model called the 3T-model to estimate ET at high

spatio-temporal resolution for 16 years (2001 – 2016). Consistency in ET data was used to observe certain hydrological anomaly spatial distribution of hydrological anomaly of annual ET exceeding annual precipitation (P). Several hotspots were located in the Eastern Himalayan watersheds which were highly resilient to water unavailability throughout the year. Out of several physical parameters, dense vegetation fraction and deep bedrock were found to be best associated with these hydrological anomalies. It indicates that the forest cover and preferential storage controls the hydrological processes in Eastern Himalayan watersheds. With the past studies and evidences of macropores, a specialized hydrological model for surface and sub-surface water balance was developed exclusively for complex watersheds of Eastern Himalaya. It was used as a demonstration with theoretical saturated hydraulic conductivity and infiltration rate on Subansiri watershed. Calibration with observed values showed the existence of hydraulic conductivity of a much larger order than expected. It shows that the sub-surface flow is affected by presence of preferential flow which is known to increase the flow velocity in hillslopes. The developed model has capability to integrate with satellite remote sensing and modelled data reveal the insights of surface water balance and runoff generation processes in hilly watersheds at high resolution spatial resolution. It is made flexible for further improvisation and can collaborate the observations of hillslope experiments in variable conditions.

7.2. Literature Review

The literature review presented a thorough discussion on long-term energy and water budgeting in poorly gauged, complex and inaccessible watersheds. It discussed the evolution of energy balance models based on remote sensing applications and its limitations. The update on one of the longest and consistently active satellite remote sensing missions, MODIS, was

debated on its application in energy budgeting and hydrological modeling studies. As discussed by many researchers, land surface vegetation and temperature are essential inputs acquired by satellite remote sensing in energy balance models. It was understood that satellite data deficiency and complex topography are the two crucial challenges in monitoring the energy and water budget in mountainous watersheds. The unavailability of satellite data restricts the access to monitor and understand the hydrological processes based on time-series. Therefore, techniques to reconstruct the time-series variables derived from satellite remote sensing for energy budgeting were discussed with a focus on data deficient regions. It was followed by review on principal component analysis technique which is widely used for reducing the complexity in vector dimensions. A brief history of hydrological models used for water balance studies was also discussed to understand the approach of handling hydrological process in a variety of cases. Finally, an advancement over understanding the hydrological process on hillslope was discussed to assimilate the knowledge and concepts for the development of a process-based hydrological model focused on complicated watersheds of Eastern Himalayan River systems.

7.3. Reconstruction of Land Surface Vegetation

The condition of land surface vegetation is represented by satellite-derived Normalized Difference Vegetation Index (NDVI). Consistent availability of high-quality NDVI time-series data is important for energy budgeting for long periods. Most of the reconstruction methods draw information temporally from the available time-series to reconstruct itself. It increases the chances of failed reconstruction in large data deficiency. Hence, a new pre-filling method, MOM was adopted to improve the observation frequency. This method increases the relevant NDVI values in the time-series by assuming trajectory in the missing span according to a

general pattern of land surface phenology. It was applied with HANTS, a popular algorithm for NDVI reconstruction, for the years 2001 – 2016 by using MODIS NDVI time-series. Together, MOM with HANTS (MHA) showed a better performance in prediction when compared to other interpolation techniques like spline and inverse distance weighted (IDW) methods. The pre-filling by MOM was found to be robust than spline and IDW due in a variety of data deficiency conditions. Physical assumption of MOM also helped to restore the seasonal trait better than other methods and HANTS smoothened NDVI time-series to get high quality NDVI data.

7.4. Reconstruction of Land Surface Temperature

Land surface temperature (LST) is the radiative skin temperature of the earth's surface and an essential input in the energy balance models. Like NDVI, satellite-based LST is also constantly interrupted by atmospheric conditions. However, daily variation of LST is not like gradual trajectory like NDVI. There is no core method for reconstruction of high quality LST time-series in complex physiography. A multi-temporal approach was used to reconstruct LST from MODIS at 1km with the help of LST from GLDAS at macroscale resolution of 0.25°. Unlike other methods, using the same variable as dependent and independent variables for assimilation was noticed to eliminate the chances of complex relationship between two different variables. The assimilation was carried out by an innovative kernel based non-parametric technique. It uses to map the cumulative frequency distribution of both the dependent variable and covariate followed by predicting the missing span of dependent variable by using covariate. The prediction is done in two stages viz. temporal followed by spatial. Comparison of reconstructed LST with original MODIS LST shows ability to restore the spatial variability in most of the regions having complex physiography with high accuracy (R^2 = 0.98 and RMSE = 0.6 K).

With good performance of kernel-based assimilation in complex region, the reconstructed LST was concluded to be suitable in Northeast region.

7.5. Surface Energy and Water Budgeting

Monitoring the evapotranspiration (ET) and precipitation (P) at surface level are anticipated to unveil some of the basic knowledge on the ongoing hydrological processes. Limitation of observations in poorly gauged watersheds poses big questions on understanding of hydrological complexity. Therefore, consistent ET was estimated by using reconstructed NDVI and LST time-series. Monitoring long-term ET and P data at high resolution showed hydrological anomaly of annual ET exceeding annual P in several hotpots. Some of these hotspots were observed with high frequency in 16 years of analysis which indicated the resilience of those regions to water deficit. To know the basis of the resilience, it was necessary to find a one or more physical indicator/indicators causing the process. Hence, 9 selected physical parameters viz. topographic wetness index, elevation, slope, bedrock depth in R-horizon, vegetation fraction, percentage of sand, silt & clay and regional valley depth were analyzed singularly as well as in combinations (by using PCA) to have relationship with frequency of hydrological anomaly in Eastern Himalayan stretch. It was found that most of the watersheds were having the best relationship for vegetation fraction and bedrock depth. Moreover, this relationship was positive for both the physical parameters. This evidence combining was combined with hydrological efficiency test for different LULC to conclude that the forest cover having high bedrock depth are causing the frequency of annual ET more than annual P. The interpretation clearly indicates the preferential storage which might be possible due to deep macropores due to roots of forest and more space for sub-surface storage due to

deeper bedrock. These observations are useful for knowledge building and could be used in assimilation strategies for development of efficient process-based hydrological model.

7.6. Hydrological Modeling for Hilly Watersheds

The evidences of threshold-based runoff generation process in the hillslopes of humid tropical or sub-tropical regions is contrasting with most of the hydrological modeling concepts. Researchers have stated the reason for occurrence of this threshold is due to presence of macropores which is mostly neglected in modeling works and often varies with LULC depending upon vegetation. The soil-bedrock interface is also an important factor in hillslopes to have control over threshold. Since, vegetation fraction and bedrock depth displayed their potential to reflect frequency of hydrological anomaly (viz. presence of resilience) in many watersheds of Eastern Himalaya, it was considered that the variation in spatial distribution of threshold could be represented by these two parameters. It is because threshold and resilience are directly related. A process based semi-distributed model was developed incorporating the findings of previous experiments and works in the Eastern Himalayan region. The model used daily ET and P as forcing data and it was calibrated with field observations for an optimum threshold and saturated hydraulic conductivity. It was noticed that the model predicts the flow with high NSE value of 0.84 at 1cm±25% variation of threshold and a much higher order saturated hydraulic conductivity $\approx 10^4$ m/s than expected ranges. The calibration indicated the presence sub-surface flow at a higher velocity indirectly hinting the presence of preferential flow contribution to runoff. Moreover, the existence of preferential flow was confirmed when same regions with least surface runoff generation ratio, but high base flow volume were observed. These regions were mostly forests and grassland. Therefore, it can be said that dominance of macropores which lead a proportion of the infiltrated water volume through

active preferential flow. As far as rainfall-runoff modeling is concerned, they can be considered as a reasonable model specialized in hilly watersheds of Eastern Himalayan region.

7.7. Recommendations for Future Research

The products from satellite remote sensing are found as a reasonable spatio-temporal source of hydrometeorological parameters for poorly gauged and isolated hilly watersheds. Interpretation of complex hydrological phenomenon like hydrological resilience requires observation of high spatio-temporal resolution hydrological components. This study provides a considerate towards the use of satellite based hydrological components to observe and locate the presence of hydrological resilience. The spatial dynamics of threshold for runoff generation is modeled for isolated river basins by considering direct relation with hydrological resilience which is indicated by satellite based geospatial parameters, i.e. vegetation fraction and bedrock depth. It is evident that that there is always scope for improvement in uncertainty reduction of remote sensing based hydrometeorological and hydrological parameters, but it can be achieved only with time and contribution of researchers in future.

The interaction between hydrometeorological variables and land surface is the initial process focused in hydrological modeling. The consequences of this interaction are highly dependent upon the antecedent conditions in the sub-surface. Therefore, even with the small capability to store water in comparison to the total terrestrial water, the sub-surface should be treated as an important part in water budgeting. It consists of variable active rootzone, soil type, macropores and bedrock structures which creates complexities in the runoff generation. This work utilized some of the archived articles which characterized the sub-surface of Eastern Himalayan region by considering the macropore, rootzone, and bedrock dynamics through distributed dye tracer

experiments. However, this characterization is region-specific and further research is required in other regions.

The development of physically based semi-distributed hydrological model was a challenge due to limitations in gauged hydrological observations. The model is developed at a timescale of daily inputs and defended at monthly level. It is found that the actual hydraulic conductivity at saturation or K_{sat} could be much times higher than its theoretical counterpart. Therefore, the development, calibration, and validation of physically based hydrological models at finer timescale is another dimension which has the scope of future exploration. River basins with rich hydrological observations can unveil several hydrological phenomena at finer timescale (eg. infiltration, lateral exchanges, and baseflow). It would contribute to the improvement of model having capability to upscale for integration with satellite gravimetry.

To further carry out the research in these directions, it may yield useful results. The scope of future research discussed as follows.

1. Reduction of data uncertainty with multi-satellite and ground-based observations.
2. To conduct dye trace experiments and characterize macropore geometry in a variety of regions.
3. To conduct experiments focusing the sub-surface and observe the daily scale variability of lateral exchanges.
4. To study and understand complexity of sparse-vegetated hilly watersheds.
5. Integration of hilly watersheds with alluvial ground water level fluctuations.
6. Integration with large scale satellite gravimetry data for regional interpretations of water balance.

Bibliography

Abdi, H., Williams, L.J., 2010. Principal component analysis. Wiley Interdiscip. Rev. Comput. Stat. 2, 433–459. doi:10.1002/wics.101

Agam, N., Kustas, W.P., Anderson, M.C., Li, F. and Neale, C.M., 2007. A vegetation index based technique for spatial sharpening of thermal imagery. Remote Sensing of Environment, 107(4), 545-558. doi:10.1016/j.rse.2006.10.006

Agam, N., Kustas, W.P., Anderson, M.C., Li, F., Colaizzi, P.D., 2007. Utility of thermal sharpening over Texas high plains irrigated agricultural fields. J. Geophys. Res. 112, D19110. doi:10.1029/2007JD008407

Ahmed, M., Else, B., Eklundh, L., Ardö, J., Seaquist, J., 2017. Dynamic response of NDVI to soil moisture variations during different hydrological regimes in the Sahel region. Int. J. Remote Sens. 38, 5408–5429. doi:10.1080/01431161.2017.1339920

Allen, R.G., 1994. An update for the calculation of reference evapotranspiration. ICID Bull., 43(2), 35-92.

Allen, R.G., Pereira, L.S., Raes, D. and Smith, M., 1998. Crop evapotranspiration-Guidelines for computing crop water requirements-FAO Irrigation and drainage paper 56. Fao, Rome, 300(9), p.D05109.

Anav, A., Liu, Q., De Marco, A., Proietti, C., Savi, F., Paoletti, E., Piao, S., 2018. The role of plant phenology in stomatal ozone flux modeling. Glob. Chang. Biol. 24, 235–248. doi:10.1111/gcb.13823

Atzberger, C., Eilers, P.H.C., 2011a. Evaluating the effectiveness of smoothing algorithms in the absence of ground reference measurements. Int. J. Remote Sens. 32, 3689–3709. doi:10.1080/01431161003762405

Atzberger, C., Eilers, P.H.C., 2011b. A time series for monitoring vegetation activity and phenology at 10-daily time steps covering large parts of South America. doi:10.1080/17538947.2010.505664. doi:10.1080/17538947.2010.505664

Azzali, S., Menenti, M., 2000. Mapping vegetation-soil-climate complexes in southern Africa using temporal Fourier analysis of NOAA-AVHRR NDVI data. Int. J. Remote Sens. 21, 973–996. doi:10.1080/014311600210380

Bachmair, S., Weiler, M., Nützmann, G., 2009. Controls of land use and soil structure on water movement: Lessons for pollutant transfer through the unsaturated zone. J. Hydrol. 369, 241–252. doi:10.1016/J.JHYDROL.2009.02.031

Baigorria, G., Jones, J., Shin, D., Mishra, A., O'Brien, J., 2007. Assessing uncertainties in crop model simulations using daily bias-corrected Regional Circulation Model outputs. Clim. Res. 34, 211–222. doi:10.3354/cr00703

Bastiaanssen, W.G.M., Meneti, M., Feddes, R.A., Holtslag, A.A.M., 1998. A remote sensing surface energy balance algorithm for land (SEBAL): 1. Formulation. J. Hydrol. 212–213, 198–212. doi:10.1016/S0022-1694(98)00254-6

Bastiaanssen, W.G.M., Pelgrum, H., Wang, J., Ma, Y., Moreno, J.F., Roerink, G.J., Van Der Wal, T., 1998. A remote sensing surface energy balance algorithm for land (SEBAL): 2. Validation. J. Hydrol. 212–213, 213–229. doi:10.1016/S0022-1694(98)00254-6

Beck, P.S.A., Atzberger, C., Høgda, K.A., Johansen, B., Skidmore, A.K., 2006. Improved monitoring of vegetation dynamics at very high latitudes: A new method using MODIS NDVI. Remote Sens. Environ. 100, 321–334. doi:10.1016/J.RSE.2005.10.021

Bennett, K.E., Urrego Blanco, J.R., Jonko, A., Bohn, T.J., Atchley, A.L., Urban, N.M., Middleton, R.S., 2018. Global sensitivity of simulated water balance indicators under future climate change in the Colorado basin. Water Resour. Res. 54, 132–149. doi:10.1002/2017WR020471

Berry, S.L., Farquhar, G.D., Roderick, M.L., 2005. Co-Evolution of climate, soil and vegetation, in: encyclopedia of hydrological sciences. John Wiley & Sons, Ltd, Chichester, UK. doi:10.1002/0470848944.hsa011

Berry, Z.C., Evaristo, J., Moore, G., Poca, M., Steppe, K., Verrot, L., Asbjornsen, H., Borma, L.S., Bretfeld, M., Hervé-Fernández, P., Seyfried, M., Schwendenmann, L., Sinacore, K., De Wispelaere, L., McDonnell, J., 2018. The two water worlds hypothesis: Addressing multiple working hypotheses and proposing a way forward. Ecohydrology 11, e1843. doi:10.1002/eco.1843

Besharat, F., Dehghan, A.A., Faghih, A.R., 2013. Empirical models for estimating global solar radiation: A review and case study. Renewable and Sustainable Energy Reviews, 21 , 798-821. doi:10.1016/j.rser.2012.12.043

Beven, K., Germann, P., 2013. Macropores and water flow in soils revisited. Water Resour. Res. 49, 3071–3092. doi:10.1002/wrcr.20156

Beven, K.J., Cloke, H.L., 2012. Comment on "Hyperresolution global land surface modeling: Meeting a grand challenge for monitoring Earth's terrestrial water" by Eric F. Wood et al. Water Resour. Res. 48. doi:10.1029/2011WR010982

Beven, K.J., Kirkby, M.J., 1979. A physically based, variable contributing area model of basin hydrology. Hydrol. Sci. Bull. 24, 43–69. doi:10.1080/02626667909491834

Bhattacharya, B.K., Padmanabhan, N., Mahammed, S., Ramakrishnan, R., Parihar, J.S., 2013. Assessing solar energy potential using diurnal remote-sensing observations from Kalpana-1 VHRR and validation over the Indian landmass. International Journal of Remote Sensing, 34, 7069-7090. doi:10.1080/01431161.2013.811311

Bierkens, M.F.P.P., Bell, V.A., Burek, P., Chaney, N., Condon, L.E., David, C.H., de Roo, A., Döll, P., Drost, N., Famiglietti, J.S., Flörke, M., Gochis, D.J., Houser, P., Hut, R., Keune, J., Kollet, S., Maxwell, R.M., Reager, J.T., Samaniego, L., Sudicky, E., Sutanudjaja, E.H., van de Giesen, N., Winsemius, H., Wood, E.F., 2015. Hyper-resolution global hydrological modelling: what is next?: "Everywhere and locally relevant." Hydrol. Process. 29, 310–320. doi:10.1002/hyp.10391

Bouma, J., Dekker, L.W., 1978. A case study on infiltration into dry clay soil I. Morphological observations. Geoderma 20, 27–40. doi:10.1016/0016-7061(78)90047-2

Brubaker, K., Rango, A., Kustas, W., 1996. Incorporating radiation inputs into the snowmelt runoff model. Hydrological Processes, 10, 1329-1343. doi:10.1002/(SICI)1099-1085(199610)10:10<1329::AID-HYP464>3.0.CO;2-W

Brutsaert, W., 1975. On a derivable formula for long-wave radiation from clear skies. Water Resour. Res. 11, 742–744. doi:10.1029/WR011i005p00742

Bucha, T., Koren, M., 2017. Phenology of the beech forests in the Western Carpathians from MODIS for 2000-2015. doi:10.3832/IFOR2062-010

Carlson, T.N., Gillies, R.R. and Schmugge, T.J., 1995. An interpretation of methodologies for indirect measurement of soil water content. Agricultural and forest meteorology, 77(3-4), 191-205. doi:10.1016/0168-1923(95)02261-U

Carreiras, J.M.B., Pereira, J.M.C., Shimabukuro, Y.E., Stroppiana, D., 2003. Evaluation of compositing algorithms over the Brazilian Amazon using SPOT-4 vegetation data. Int. J. Remote Sens. 24, 3427–3440. doi:10.1080/0143116021000021251

Chao Zeng, Huanfeng Shen, Mingliang Zhong, Liangpei Zhang, Penghai Wu, 2015. Reconstructing MODIS LST based on multitemporal classification and robust regression. IEEE Geosci. Remote Sens. Lett. 12, 512–516. doi:10.1109/LGRS.2014.2348651

Chen, J., Jönsson, P., Tamura, M., Gu, Z., Matsushita, B., Eklundh, L., 2004. A simple method for reconstructing a high-quality NDVI time-series data set based on the Savitzky–Golay filter. Remote Sens. Environ. 91, 332–344. doi:10.1016/J.RSE.2004.03.014

Chen, L., Young, M.H., 2006. Green-Ampt infiltration model for sloping surfaces. Water Resour. Res. 42, 1–9. doi:10.1029/2005WR004468

Chen, X., 2017. Spatiotemporal coupling effects of plant phenology. Springer, Berlin, Heidelberg, 91–96. doi:10.1007/978-3-662-49839-2_9

Chouksey, A., Lambey, V., Nikam, B.R., Aggarwal, S.P., Dutta, S., 2017. Hydrological modelling using a rainfall simulator over an experimental hillslope plot. Hydrology 4. doi:10.3390/hydrology4010017

Chuvieco, E., Cocero, D., Riaño, D., Martin, P., Martínez-Vega, J., de la Riva, J., Pérez, F., 2004. Combining NDVI and surface temperature for the estimation of live fuel moisture content in forest fire danger rating. Remote Sens. Environ. 92, 322–331. doi:10.1016/J.RSE.2004.01.019

Cleugh, H.A., Leuning, R., Mu, Q., Running, S.W., 2007. Regional evaporation estimates from flux tower and MODIS satellite data. Remote Sens. Environ. 106, 285–304. doi:10.1016/j.rse.2006.07.007

Conrad, O., Bechtel, B., Bock, M., Dietrich, H., Fischer, E., Gerlitz, L., Wehberg, J., Wichmann, V., Böhner, J., 2015. System for automated geoscientific analyses (SAGA) v. 2.1.4. Geosci. Model Dev. 8, 1991–2007. doi:10.5194/gmd-8-1991-2015

Courtier, P., Bouttier, F., 2001. Assimilation_concepts_ecmwf. Ecmwf Lect. Notes 1–58.

Crawford, T.M., Duchon, C.E., Crawford, T.M., Duchon, C.E., 1999. An improved parameterization for estimating effective atmospheric emissivity for use in calculating daytime downwelling longwave radiation. J. Appl. Meteorol. 38, 474–480. doi:10.1175/1520-0450(1999)038<0474:AIPFEE>2.0.CO;2

Danehy, R.J., Colson, C.G., Parrett, K.B., Duke, S.D., 2005. Patterns and sources of thermal heterogeneity in small mountain streams within a forested setting. Forest Ecology and Management, 208, 287-302. doi:10.1016/j.foreco.2004.12.006

Das, P., Islam, A., Dutta, S., Dubey, A.K., Sarkar, R., 2014. Estimation of runoff curve numbers using a physically-based approach of preferential flow modelling. International Association of Hydrological Sciences (IAHS) Publication, 363, 443-448.

de Beurs, K.M., Henebry, G.M., 2005. A statistical framework for the analysis of long image time series. Int. J. Remote Sens. 26, 1551–1573. doi:10.1080/01431160512331326657

de Jong, C., Collins, D., Ranzi, R., 2005. Climate and Hydrology in Mountain Areas. Wiley, West Sussex, England.

de Jong, C., Ranzi, R., Collins, D., 2006. Introduction: Climate and Hydrology in Mountain Areas, in: Climate and Hydrology in Mountain Areas. John Wiley & Sons, Ltd, Chichester, UK, xix–xxi. doi:10.1002/0470858249.ch

Didan, K., 2015. MOD13A1 MODIS/Terra Vegetation Indices 16-Day L3 Global 500m SIN Grid V006 [Data set], NASA EOSDIS LP DAAC. doi: 10.5067/MODIS/MOD13A1.006

Drinkwater, M.R., Floberghagen, R., Haagmans, R., Muzi, D., Popescu, A., 2011. GOCE: ESA'S first earth explorer core mission. Russell J. Bertrand Russell Arch. 26428, 1–4. doi:10.1007/978-94-017-1333-7_36

Dusek, J., Vogel, T., 2016. Hillslope-storage and rainfall-amount thresholds as controls of preferential stormflow. J. Hydrol. 534, 590–605. doi:10.1016/J.JHYDROL.2016.01.047

Dutta, S., Zade, M, 2003. RISE-A distributed hydrologic model for rice agriculture: Concept and evaluation. In Watershed Hydrology; Singh, V.P., Yadava, R.N., Eds., 240–251, Allied Publisher: New Delhi, India.

Fan, X.-M., Liu, H.-G., Liu, G.-H., Li, S.-B., 2014. Reconstruction of MODIS land-surface temperature in a flat terrain and fragmented landscape. Int. J. Remote Sens. 35, 7857–7877. doi:10.1080/01431161.2014.978036

Fatichi, S., Vivoni, E.R., Ogden, F.L., Ivanov, V.Y., Mirus, B., Gochis, D., Downer, C.W., Camporese, M., Davison, J.H., Ebel, B., Jones, N., Kim, J., Mascaro, G., Niswonger, R., Restrepo, P., Rigon, R., Shen, C., Sulis, M., Tarboton, D., 2016. An overview of current applications, challenges, and future trends in distributed process-based models in hydrology. J. Hydrol. 537, 45–60. doi:10.1016/J.JHYDROL.2016.03.026

Fayad, A., Gascoin, S., Faour, G., López-Moreno, J.I., Drapeau, L., Page, M. Le, Escadafal, R., 2017. Snow hydrology in Mediterranean mountain regions: A review. J. Hydrol. doi:10.1016/j.jhydrol.2017.05.063

Fayad, A., Gascoin, S., Faour, G., López-Moreno, J.I., Drapeau, L., Page, M.L., Escadafal, R., 2017. Snow hydrology in Mediterranean mountain regions: A review. Journal of Hydrology, 551, 374-396. doi: 10.1016/j.jhydrol.2017.05.063

Fischer, A., 1994. A model for the seasonal variations of vegetation indices in coarse resolution data and its inversion to extract crop parameters. Remote Sens. Environ. 48, 220–230. doi:10.1016/0034-4257(94)90143-0

Friedl, M.., McIver, D.., Hodges, J.C.., Zhang, X.., Muchoney, D., Strahler, A.., Woodcock, C.., Gopal, S., Schneider, A., Cooper, A., Baccini, A., Gao, F., Schaaf, C., 2002. Global land cover mapping from MODIS: algorithms and early results. Remote Sens. Environ. 83, 287–302. doi:10.1016/S0034-4257(02)00078-0

Galat, D., R. Berry, C., J. Peters, E., G. White, R., 2005. Missouri River Basin. doi:10.1016/B978-012088253-3/50013-4

Gandhi, G.M., Parthiban, S., Thummalu, N., Christy, A., 2015. NDVI: vegetation change detection using remote sensing and GIS – A case study of Vellore district. Procedia Comput. Sci. 57, 1199–1210. doi:10.1016/J.PROCS.2015.07.415

Gates, D.M., 1980a. Energy and Energy Budgets. In: Biophysical Ecology. Springer Advanced Texts in Life Sciences. Springer, New York. doi:10.1007/978-1-4612-6024-0_2

Gates, D.M., 1980b. Solar Radiation. In: Biophysical Ecology. Springer Advanced Texts in Life Sciences. Springer, New York. doi:10.1007/978-1-4612-6024-0_6

Gedney, N., Cox, P.M., Betts, R.A., Boucher, O., Huntingford, C., Stott, P.A., 2006. Detection of a direct carbon dioxide effect in continental river runoff records. Nature 439, 835–838. doi:10.1038/nature04504

Geerken, R., Zaitchik, B., Evans, J.P., 2005. Classifying rangeland vegetation type and coverage from NDVI time series using Fourier Filtered Cycle Similarity. Int. J. Remote Sens. 26, 5535–5554. doi:10.1080/01431160500300297

Geng, L., Ma, M., Wang, H., 2016. An effective compound algorithm for reconstructing MODIS NDVI time series data and its validation based on ground measurements. IEEE J. Sel. Top. Appl. Earth Obs. Remote Sens. 9, 3588–3597. doi:10.1109/JSTARS.2015.2495112

Geng, L., Ma, M., Wang, X., Yu, W., Jia, S., Wang, H., Geng, L., Ma, M., Wang, X., Yu, W., Jia, S., Wang, H., 2014. Comparison of eight techniques for reconstructing multi-satellite sensor time-series NDVI data sets in the Heihe river basin, China. Remote Sens. 6, 2024–2049. doi:10.3390/rs6032024

Glennie, E., Anyamba, A., 2018. Midwest agriculture and ENSO: A comparison of AVHRR NDVI3g data and crop yields in the United States corn belt from 1982 to 2014. Int. J. Appl. Earth Obs. Geoinf. 68, 180–188. doi:10.1016/J.JAG.2017.12.011

Gokmen, M., Vekerdy, Z., Verhoef, W., Batelaan, O., 2013. Satellite-based analysis of recent trends in the ecohydrology of a semi-arid region. Hydrol. Earth Syst. Sci 17, 3779–3794. doi:10.5194/hess-17-3779-2013

Gowda, P.H., Chavez, J.L., Colaizzi, P.D., Evett, S.R., Howell, T.A., Tolk, J.A., 2008. ET mapping for agricultural water management: Present status and challenges. 26-223, Irrig. Sci. doi:10.1007/s00271-007-0088-6

Graham, C.B., McDonnell, J.J., 2010. Hillslope threshold response to rainfall: (2) Development and use of a macroscale model. J. Hydrol. 393, 77–93. doi:10.1016/j.jhydrol.2010.03.008

Graham, C.B., Woods, R.A., McDonnell, J.J., 2010a. Hillslope threshold response to rainfall: (1) A field based forensic approach. J. Hydrol. 393, 65–76. doi:10.1016/J.JHYDROL.2009.12.015

Grizzetti, B., Bouraoui, F., De Marsily, G., 2005. Modelling nitrogen pressure in river basins: A comparison between a statistical approach and the physically-based SWAT model. Phys. Chem. Earth, Parts A/B/C 30, 508–517. doi:10.1016/J.PCE.2005.07.005

Gu, J., Li, X., Huang, C., Okin, G.S., 2009. A simplified data assimilation method for reconstructing time-series MODIS NDVI data. Adv. Sp. Res. 44, 501–509. doi:10.1016/J.ASR.2009.05.009

Gudmundsson, L., Leonard, M., Do, H.X., Westra, S., Seneviratne, S.I., 2019. Observed trends in global indicators of mean and extreme streamflow. Geophys. Res. Lett. 46, 756–766. doi:10.1029/2018GL079725

Gutiérrez-Jurado, H.A., Vivoni, E.R., 2013. Ecogeomorphic expressions of an aspect-controlled semiarid basin: II. Topographic and vegetation controls on solar irradiance. Ecohydrology 6, 24–37. doi:10.1002/eco.1263

Harvey, A., Oryshchenko, V., 2012. Kernel density estimation for time series data. Int. J. Forecast. 28, 3–14. doi:10.1016/J.IJFORECAST.2011.02.016

Hassan, A., 2016. Water storage changes and balances in Africa observed by GRACE and hydrologic models. Geod. Geodyn. 7, 39–49. doi:10.1016/J.GEOG.2016.03.002

Hengl, T., Mendes de Jesus, J., Heuvelink, G.B.M., Ruiperez Gonzalez, M., Kilibarda, M., Blagotić, A., Shangguan, W., Wright, M.N., Geng, X., Bauer-Marschallinger, B., Guevara, M.A., Vargas, R., MacMillan, R.A., Batjes, N.H., Leenaars, J.G.B., Ribeiro, E., Wheeler, I., Mantel, S., Kempen, B., 2017. SoilGrids250m: Global gridded soil information based on machine learning. PLoS One 12, e0169748. doi:10.1371/journal.pone.0169748

Hengl, T., Mendes de Jesus, J., Heuvelink, G.B.M., Ruiperez Gonzalez, M., Kilibarda, M., Blagotić, A., Shangguan, W., Wright, M.N., Geng, X., Bauer-Marschallinger, B., Guevara, M.A., Vargas, R., MacMillan, R.A., Batjes, N.H., Leenaars, J.G.B., Ribeiro, E., Wheeler, I., Mantel, S., Kempen, B., 2017. SoilGrids250m: Global gridded soil information based on machine learning. PLoS One 12, e0169748. doi:10.1371/journal.pone.0169748

Hoffmann, H., 2007. Kernel PCA for novelty detection. Pattern Recognit. 40, 863–874. doi:10.1016/j.patcog.2006.07.009

Holben, B.N., 1986. Characteristics of maximum-value composite images from temporal AVHRR data. Int. J. Remote Sens. 7, 1417–1434. doi:10.1080/01431168608948945

Holdaway, D., Yang, Y., 2016. Study of the effect of temporal sampling frequency on DSCOVR observations using the GEOS-5 Nature Run Results (Part I): Earth's radiation budget. Remote Sensing, 8, 98. doi:10.3390/rs8020098

Hoognoed, W.B., Bouma, J., 1980. SIMULATION MODEL FOR PREDICTING INFILTRATION INTO CRACKED CLAY SOIL. Soil Sci. Soc. Am. J. 44, 458–461. doi:10.2136/sssaj1980.03615995004400030003x

Hou, W., Gao, J., 2019. Simulating runoff generation and its spatial correlation with environmental factors in Sancha River Basin: The southern source of the Wujiang River. J. Geogr. Sci. 29, 432–448. doi:10.1007/s11442-019-1608-z

Houghton, J., Ding, Y., Griggs, D., Noguer, M., van der Linden, P., Dai, X., 2001. Climate change 2001: the scientific basis. Cambridge. doi:10.1256/004316502320517344

Hrachowitz, M., Savenije, H.H.G., Blöschl, G., McDonnell, J.J., Sivapalan, M., Pomeroy, J.W., Arheimer, B., Blume, T., Clark, M.P., Ehret, U., Fenicia, F., Freer, J.E., Gelfan, A., Gupta, H. V, Hughes, D.A., Hut, R.W., Montanari, A., Pande, S., Tetzlaff, D., Troch, P.A., Uhlenbrook, S., Wagener, T., Winsemius, H.C., Woods, R.A., Zehe, E., Cudennec, C., Savenije, H.G., 2013. A decade of Predictions in Ungauged Basins (PUB)-a review. Hydrol. Sci. J. 58, 1198–1255. doi:10.1080/02626667.2013.803183

Huang, P., Zhao, W., Li, A., 2017. The preliminary investigation on the uncertainties associated with surface solar radiation estimation in mountainous areas. IEEE Geoscience and Remote Sensing Letters, 14, 1071 – 1075. doi:10.1109/LGRS.2017.2696973

Huang, Q., Long, D., Du, M., Zeng, C., Qiao, G., Li, X., Hou, A., Hong, Y., 2018. Discharge estimation in high-mountain regions with improved methods using multisource remote sensing: A case study of the Upper Brahmaputra River. Remote Sens. Environ. 219, 115–134. doi:10.1016/j.rse.2018.10.008

I. D. Moore, I.D., G. J. Burch, G.J., D. H. Mackenzie, D.H., 1988. Topographic effects on the distribution of surface soil water and the location of ephemeral gullies. Trans. ASAE 31, 1098–1107. doi:10.13031/2013.30829

Ines, A.V.M., Hansen, J.W., 2006. Bias correction of daily GCM rainfall for crop simulation studies. Agric. For. Meteorol. 138, 44–53. doi:10.1016/J.AGRFORMET.2006.03.009

Jackson, R.D., Hatfield, J.L., Reginato, R.J., Idso, S.B. and Pinter Jr, P.J., 1983. Estimation of daily evapotranspiration from one time-of-day measurements. Agricultural Water Management, 7(1-3), 351-362. doi:10.1016/0378-3774(83)90095-1

Jackson, R.D., Hatfield, J.L., Reginato, R.J., Idso, S.B., Pinter, P.J., 1983. Estimation of daily evapotranspiration from one time-of-day measurements. Agric. Water Manag. 7, 351–362. doi:10.1016/0378-3774(83)90095-1

Janzen, D., McDonnell, J.J., 2015. A stochastic approach to modelling and understanding hillslope runoff connectivity dynamics. Ecol. Modell. 298, 64–74. doi:10.1016/J.ECOLMODEL.2014.06.024

Jeong, D.I., St-Hilaire, A., Gratton, Y., Bélanger, C., Saad, C., 2017. A guideline to select an estimation model of daily global solar radiation between geostatistical interpolation and stochastic simulation approaches. Renewable Energy, 103 , 70-80. doi:10.1016/j.renene.2016.11.022

Jia, L, Shang, H., Hu, G., Menenti, M., 2011. Phenological response of vegetation to upstream river flow in the Heihe river basin by time series analysis of MODIS data. Hydrol. Earth Syst. Sci 15, 1047–1064. doi:10.5194/hess-15-1047-2011

Jiang, D., Zhang, H., Zhang, Y., Wang, K., 2014. Interannual variability and correlation of vegetation cover and precipitation in Eastern China. Theor. Appl. Climatol. 118, 93–105. doi:10.1007/s00704-013-1054-2

Jiménez-Muñoz, J.C., Sobrino, J.A., 2003. A generalized single-channel method for retrieving land surface temperature from remote sensing data. J. Geophys. Res. 108, 4688. doi:10.1029/2003JD003480

JIN, X., HU, G., LI, W., 2008. Hysteresis effect of runoff of the Heihe river on vegetation cover in the Ejina Oasis in Northwestern China. Earth Sci. Front. 15, 198–203. doi:10.1016/S1872-5791(08)60054-8

Joiner, J., Yoshida, Y., Anderson, M., Holmes, T., Hain, C., Reichle, R., Koster, R., Middleton, E., Zeng, F.-W., 2018. Global relationships among traditional reflectance vegetation indices (NDVI and NDII), evapotranspiration (ET), and soil moisture variability on weekly timescales. Remote Sens. Environ. 219, 339–352. doi:10.1016/J.RSE.2018.10.020

Jones, M.C., 1990. The performance of kernel density functions in kernel distribution function estimation. Stat. Probab. Lett. 9, 129–132. doi:10.1016/0167-7152(92)90006-Q

Jönsson, P., Eklundh, L., 2004. TIMESAT—a program for analyzing time-series of satellite sensor data. Comput. Geosci. 30, 833–845. doi:10.1016/J.CAGEO.2004.05.006

Julien, Y., Sobrino, J.A., 2010. Comparison of cloud-reconstruction methods for time series of composite NDVI data. Remote Sens. Environ. 114, 618–625. doi:10.1016/J.RSE.2009.11.001

Julien, Y., Sobrino, J.A., 2019. Optimizing and comparing gap-filling techniques using simulated NDVI time series from remotely sensed global data. Int. J. Appl. Earth Obs. Geoinf. 76, 93–111. doi:10.1016/J.JAG.2018.11.008

Jun, W., Zhongbo, S., Yaoming, M., 2009. Reconstruction of a cloud-free vegetation index time series for the Tibetan plateau. doi:10.1659/0276-4741(2004)024[0348:ROACVI]2.0.CO;2

Justice, C.O., Townshend, J.R.G., Holben, B.N., Tucker, C.J., 1985. Analysis of the phenology of global vegetation using meteorological satellite data. Int. J. Remote Sens. 6, 1271–1318. doi:10.1080/01431168508948281

Kamali, M., Ponnambalam, K., Soulis, E.D., 2007. Integration of surrogate optimization and PCA for calibration of hydrologic models, A WATCLASS case study, in: Conference Proceedings - IEEE International Conference on Systems, Man and Cybernetics. 2733–2737. doi:10.1109/ICSMC.2007.4414073

Kang, J., Tan, J., Jin, R., Li, X., Zhang, Y., 2018. Reconstruction of MODIS land surface temperature products based on Multi-Temporal information. Remote Sens. 10, 1112. doi:10.3390/rs10071112

Karlsson, J.M., Lyon, S.W., Destouni, G., 2012. Thermokarst lake, hydrological flow and water balance indicators of permafrost change in Western Siberia. J. Hydrol. 464–465, 459–466. doi:10.1016/j.jhydrol.2012.07.037

Kato, S., Rose, F.G., Sun-Mack, S., Miller, W.F., Chen, Y., Rutan, D.A., Stephens, G.L., Loeb, N.G., Minnis, P., Wielicki, B.A., Winker, D.M., Charlock, T.P., Stackhouse, P.W., Xu, K.-M., Collins, W.D., 2011. Improvements of top-of-atmosphere and surface irradiance computations with CALIPSO-, CloudSat-, and MODIS-derived cloud and aerosol properties. Journal of Geophysical Research: Atmospheres, 116, D19. doi:10.1029/2011JD016050

Katul, G.G., Oren, R., Manzoni, S., Higgins, C., Parlange, M.B., 2012. Evapotranspiration: A process driving mass transport and energy exchange in the soil-plant-atmosphere-climate system. Reviews of Geophysics, 50. doi:10.1029/2011RG000366

Ke, L., Ding, X., Song, C., 2013. Reconstruction of time-series MODIS LST in Central Qinghai-Tibet Plateau using geostatistical approach. IEEE Geosci. Remote Sens. Lett. 10, 1602–1606. doi:10.1109/LGRS.2013.2263553

Kiapasha, K., Darvishsefat, A.A., Julien, Y., Sobrino, J.A., Zargham, N., Attarod, P., Schaepman, M.E., 2017. Trends in phenological parameters and relationship between land surface phenology and climate data in the Hyrcanian forests of Iran. IEEE J. Sel. Top. Appl. Earth Obs. Remote Sens. 10, 4961–4970. doi:10.1109/JSTARS.2017.2736938

Kite, G.W., Droogers, P., 2000. Comparing evapotranspiration estimates from satellites, hydrological models and field data. J. Hydrol. doi:10.1016/S0022-1694(99)00195-X

Kitsara, G., Papaioannou, G., Retalis, A., Paronis, D., Kerkides, P., 2018. Estimation of air temperature and reference evapotranspiration using MODIS land surface temperature over Greece. Int. J. Remote Sens. 39, 924–948. doi:10.1080/01431161.2017.1395965

Kobayashi, H., Dye, D.G., 2005. Atmospheric conditions for monitoring the long-term vegetation dynamics in the Amazon using normalized difference vegetation index. Remote Sens. Environ. 97, 519–525. doi:10.1016/J.RSE.2005.06.007

Kobayashi, S., Ota, Y., Harada, Y., Ebita, A., Moriya, M., Onoda, H., Onogi, K., Kamahori, H., Kobayashi, C., Endo, H., Miyaoka, K., Takahashi, K., 2015. The JRA-55 Reanalysis: General specifications and basic characteristics. Journal of the Meteorological Society of Japan. Ser. II, 93, 5-48. doi:10.2151/jmsj.2015-001

Kou, X., Jiang, L., Bo, Y., Yan, S., Chai, L., Kou, X., Jiang, L., Bo, Y., Yan, S., Chai, L., 2016. Estimation of Land Surface Temperature through Blending MODIS and AMSR-E Data with the Bayesian Maximum Entropy Method. Remote Sens. 8, 105. doi:10.3390/rs8020105

Kouraev, A. V., Zakharova, E.A., Samain, O., Mognard, N.M., Cazenave, A., 2004. Ob' river discharge from TOPEX/Poseidon satellite altimetry (1992-2002). Remote Sens. Environ. 93, 238–245. doi:10.1016/j.rse.2004.07.007

Kouraev, A. V., Zakharova, E.A., Samain, O., Mognard, N.M., Cazenave, A., 2004. Ob' river discharge from TOPEX/Poseidon satellite altimetry (1992-2002). Remote Sens. Environ. 93, 238–245. doi:10.1016/j.rse.2004.07.007

Kouraev, A.V., Zakharova, E.A., Samain, O., Mognard, N.M., Cazenave, A., 2004. Ob' river discharge from TOPEX/Poseidon satellite altimetry (1992–2002). Remote Sensing of Environment, 93, 238-245. doi:10.1016/j.rse.2004.07.007

Kroes, J.G., van Dam, J.C., 2003. Alterra-report 773 1 Reference Manual SWAP version 3.0.3.

Kubota, T., Hashizume, H., Shige, S., Okamoto, K., Aonashi, K., Takahashi, N., Ushio, T., Kachi, M., 2006. Global precipitation map using satelliteborne microwave radiometers by the GSMaP project: Production and validation. Int. Geosci. Remote Sens. Symp. 45, 2584–2587. doi:10.1109/IGARSS.2006.668

Kult, J.M., Fry, L.M., Gronewold, A.D., Choi, W., 2014. Regionalization of hydrologic response in the Great Lakes basin: Considerations of temporal scales of analysis. J. Hydrol. 519, 2224–2237. doi:10.1016/J.JHYDROL.2014.09.083

Kumar, L., Skidmore, A.K., Knowles, E., 1997. Modelling topographic variation in solar radiation in a GIS environment. International Journal of Geographical Information Science, 11, 475-497. doi:10.1080/136588197242266

Kundu, A., Denis, D., Patel, N., Dutta, D., 2018. A Geo-spatial study for analysing temporal responses of NDVI to rainfall. Singap. J. Trop. Geogr. 39, 107–116. doi:10.1111/sjtg.12217

Kundzewicz, Z.W., Mata, L.J., Arnell, N.W., Döll, P., Kabat, P., Jiménez, B., Miller, K.A., Oki, T., Sen, Z., Shiklomanov, I.A., 2007. Freshwater resources and their management. Climate Change 2007: Impacts, Adaptation and Vulnerability. Contribution of Working Group II to the Fourth Assessment Report of the Intergovernmental Panel on Climate Change, Parry, M.L., Canziani, O.F., Palutikof, J.P., van der Linden, P.J., Hanson, C.E., Eds., 173-210, Cambridge University Press, Cambridge, UK.

Kustas, W.P. and Daughtry, C.S., 1990. Estimation of the soil heat flux/net radiation ratio from spectral data. Agricultural and Forest Meteorology, 49(3), 205-223. doi:10.1016/0168-1923(90)90033-3

Labat, D., Goddéris, Y., Probst, J.L., Guyot, J.L., 2004. Evidence for global runoff increase related to climate warming. Adv. Water Resour. 27, 631–642. doi:10.1016/J.ADVWATRES.2004.02.020

L'Ecuyer, T.S., Wood, N.B., Haladay, T., Stephens, G.L., Stackhouse, P.W., 2008. Impact of clouds on atmospheric heating based on the R04 CloudSat fluxes and heating rates data set. Journal of Geophysical Research: Atmospheres, 113, D8. doi:10.1029/2008JD009951

Lhomme, J.P., Monteny, B. and Amadou, M., 1994. Estimating sensible heat flux from radiometric temperature over sparse millet. Agricultural and Forest Meteorology, 68(1-2), 77-91. doi:10.1016/0168-1923(94)90070-1

Li, F., Kustas, W.P., Prueger, J.H., Neale, C.M.U., Jackson, T.J., 2005. Utility of remote-sensing-based two-source energy balance model under low- and high-vegetation cover conditions. J. Hydrometeorol. 6, 878–891. doi:10.1175/JHM464.1

Li, N., Jia, L., Zheng, C., 2014. Evaluation of the harmonic-analysis method for surface soil heat flux estimation: a case study in Heihe river basin, in: Jackson, T.J., Chen, J.M., Gong, P., Liang, S. (Eds.), . International Society for Optics and Photonics, p. 926043. doi:10.1117/12.2069270

Liang, S., 2001. Narrowband to broadband conversions of land surface albedo I: Algorithms. Remote sensing of environment, 76(2), 213-238. doi:10.1016/S0034-4257(00)00205-4

Liang, S.Z., Ma, W.D., Sui, X.Y., Yao, H.M., Li, H.Z., Liu, T., Hou, X.H., Wang, M., 2017. Extracting the spatiotemporal pattern of cropping systems from NDVI time series using a combination of the spline and HANTS Algorithms: A case study for shandong province. Can. J. Remote Sens. 43, 1–15. doi:10.1080/07038992.2017.1252906

Liang, X., Lettenmaier, D.P., Wood, E.F., Burge, S.J., 1994. A simple hydrologically based model of land surface water and energy fluxes for general circulation model. J. Geophys. Res. 99, 14415–14428.

Lin, C.-Y., Lo, H.-M., Chou, W.-C., Lin, W.-T., 2004. Vegetation recovery assessment at the Jou-Jou Mountain landslide area caused by the 921 Earthquake in Central Taiwan. Ecol. Modell. 176, 75–81. doi:10.1016/J.ECOLMODEL.2003.12.037

Liu, D., Tian, F., Lin, M., Sivapalan, M., 2015. A conceptual socio-hydrological model of the co-evolution of humans and water: case study of the Tarim River basin, western China. Hydrol. Earth Syst. Sci 19, 1035–1054. doi:10.5194/hess-19-1035-2015

Liu, J., Zehnder, A.J.B., Yang, H., 2009. Global consumptive water use for crop production: The importance of green water and virtual water. Water Resour. Res. 45. doi:10.1029/2007WR006051

Liu, X., Zhu, X., Zhu, W., Pan, Y., Zhang, C., Zhang, D., Liu, X., Zhu, X., Zhu, W., Pan, Y., Zhang, C., Zhang, D., 2014. Changes in Spring Phenology in the Three-Rivers Headwater Region from 1999 to 2013. Remote Sens. 6, 9130–9144. doi:10.3390/rs6099130

Loeb, N.G., Kato, S., Loukachine, K., Manalo-Smith, N., 2005. Angular distribution models for top-of-atmosphere radiative flux estimation from the Clouds and the Earth's Radiant Energy System Instrument on the Terra Satellite. Part I: Methodology. Journal of Atmospheric and Oceanic Technology, 22, 338-351. doi:10.1175/jtech1712.1

Loeb, N.G., Lyman, J.M., Johnson, G.C., Allan, R.P., Doelling, D.R., Wong, T., Soden, B.J., Stephens, G.L., 2012. Observed changes in top-of-the-atmosphere radiation and upper-ocean heating consistent within uncertainty. Nature Geoscience, 5, 110-113. doi:10.1038/ngeo1375

Lovell, J.L., Graetz, R.D., 2001. Filtering Pathfinder AVHRR Land NDVI data for Australia. Int. J. Remote Sens. 22, 2649–2654. doi:10.1080/01431160116874

Lu, X.L., Liu, R.G., Liu, J.Y., Liang, S.L, 2007. Removal of noise by wavelet method to generate high quality temporal data of terrestrial MODIS products. Photogrammetric Engineering & Remote Sensing 73, 1129–1139. doi:10.14358/PERS.73.10.1129

Luo, W., Grudzinski, B., Pederson, D., 2011. Estimating hydraulic conductivity for the Martian subsurface based on drainage patterns - A case study in the Mare Tyrrhenum Quadrangle. Geomorphology 125, 414–420. doi:10.1016/j.geomorph.2010.10.018

Luo, W., Grudzinski, B.P., Pederson, D., 2010. Estimating hydraulic conductivity from drainage patterns-a case study in the Oregon Cascades. Geology 38, 335–338. doi:10.1130/G30816.1

Luo, X., Wang, K., Jiang, H., Sun, J., Zhu, Q., 2012. Estimation of land surface evapotranspiration over the Heihe River basin based on the revised three-temperature model. Hydrol. Process. 26, 1263–1269. doi:10.1002/hyp.8182

Ma, M., Veroustraete, F., 2006. Reconstructing pathfinder AVHRR land NDVI time-series data for the Northwest of China. Adv. Sp. Res. 37, 835–840. doi:10.1016/J.ASR.2005.08.037

Mayerhofer, C., Meißl, G., Klebinder, K., Kohl, B., Markart, G., 2017. Comparison of the results of a small-plot and a large-plot rainfall simulator – Effects of land use and land cover on surface runoff in Alpine catchments. CATENA 156, 184–196. doi:10.1016/J.CATENA.2017.04.009

McDonnell, J.J., 2014. The two water worlds hypothesis: ecohydrological separation of water between streams and trees? Wiley Interdiscip. Rev. Water 1, 323–329. doi:10.1002/wat2.1027

Menenti, M., Azzali, S., Verhoef, W., van Swol, R., 1993. Mapping agroecological zones and time lag in vegetation growth by means of fourier analysis of time series of NDVI images. Adv. Sp. Res. 13, 233–237. doi:10.1016/0273-1177(93)90550-U

Menichino, G.T., Ward, A.S., Hester, E.T., 2014. Macropores as preferential flow paths in meander bends. Hydrol. Process. 28, 482–495. doi:10.1002/hyp.9573

Merz, J., Dangol, P.M., Dhakal, M.P., Dongol, B. S., Nakarmi, G., Weingartner, R., 2006. Rainfall-runoff events in a middle mountain catchment of Nepal. Journal of Hydrology, 33, 446-458. doi: 10.1016/j.jhydrol.2006.05.030

Molina-Carpio, J., Espinoza, J.C., Vauchel, P., Ronchail, J., Gutierrez Caloir, B., Guyot, J.-L., Noriega, L., 2017. Hydroclimatology of the Upper Madeira River basin: spatio-temporal variability and trends. Hydrol. Sci. J. 62, 911–927. doi:10.1080/02626667.2016.1267861

Monteith, J.L., 1973. Principles of environmental physics Edward Arnold. London, 214p.

Morton, D.C., DeFries, R.S., Shimabukuro, Y.E., Anderson, L.O., Arai, E., del Bon Espirito-Santo, F., Freitas, R., Morisette, J., 2006. Cropland expansion changes deforestation dynamics in the southern Brazilian Amazon. Proc. Natl. Acad. Sci. U. S. A. 103, 14637–41. doi:10.1073/pnas.0606377103

Mu, Q., Heinsch, F.A., Zhao, M., Running, S.W., 2007. Development of a global evapotranspiration algorithm based on MODIS and global meteorology data. Remote Sens. Environ. 111, 519–536. doi:10.1016/j.rse.2007.04.015

Muro, J., Strauch, A., Heinemann, S., Steinbach, S., Thonfeld, F., Waske, B., Diekkrüger, B., 2018. Land surface temperature trends as indicator of land use changes in wetlands. Int. J. Appl. Earth Obs. Geoinf. 70, 62–71. doi:10.1016/J.JAG.2018.02.002

Musial, J.P., Verstraete, M.M., Gobron, N., 2011. Technical Note: Comparing the effectiveness of recent algorithms to fill and smooth incomplete and noisy time series. Atmos. Chem. Phys. 11, 7905–7923. doi:10.5194/acp-11-7905-2011

Mutti, P.R., da Silva, L.L., Medeiros, S. de S., Dubreuil, V., Mendes, K.R., Marques, T. V., Lúcio, P.S., Santos e Silva, C.M., Bezerra, B.G., 2019. Basin scale rainfall-evapotranspiration dynamics in a tropical semiarid environment during dry and wet years. Int. J. Appl. Earth Obs. Geoinf. 75, 29–43. doi:10.1016/J.JAG.2018.10.007

Nahry, A.H.E., Ali, R.R., Baroudy, A.A.E., 2011. An approach for precision farming under pivot irrigation system using remote sensing and GIS techniques. Agric. Water Manag. 98, 517–531. doi:10.1016/j.agwat.2010.09.012

Nemani, R., White, M., Thornton, P., Nishida, K., Reddy, S., Jenkins, J., Running, S., 2002. Recent trends in hydrologic balance have enhanced the terrestrial carbon sink in the United States. Geophys. Res. Lett. 29, 106-1-106–4. doi:10.1029/2002gl014867

Neteler, M., Neteler, Markus, 2010. Estimating daily land surface temperatures in mountainous environments by reconstructed MODIS LST data. Remote Sens. 2, 333–351. doi:10.3390/rs1020333

Niehoff, D., Fritsch, U., Bronstert, A., 2002. Land-use impacts on storm-runoff generation: Scenarios of land-use change and simulation of hydrological response in a meso-scale catchment in SW-Germany. J. Hydrol. 267, 80–93. doi:10.1016/S0022-1694(02)00142-7

Niemelä, S., Räisänen, P., Savijärvi, H., 2001. Comparison of surface radiative flux parameterizations: Part I: Longwave radiation. Atmos. Res. 58, 1–18. doi:10.1016/S0169-8095(01)00084-9

Ogden, F.L., Crouch, T.D., Stallard, R.F., Hall, J.S., 2013. Effect of land cover and use on dry season river runoff, runoff efficiency, and peak storm runoff in the seasonal tropics of Central Panama. Water Resour. Res. 49, 8443–8462. doi:10.1002/2013WR013956

Padhee, S.K., Ramachandra Nikam, B., Dutta, S., Prasad Aggarwal, S., 2017. Using satellite-based soil moisture to detect and monitor spatiotemporal traces of agricultural drought

over Bundelkhand region of India. GIScience Remote Sens. 54, 144–166. doi:10.1080/15481603.2017.1286725

Panda, S.S., Ames, D.P., Panigrahi, S., Panda, S.S., Ames, D.P., Panigrahi, S., 2010. Application of Vegetation Indices for Agricultural Crop Yield Prediction Using Neural Network Techniques. Remote Sens. 2, 673–696. doi:10.3390/rs2030673

Park, J.-G., Tateishi, R., Matsuoka, M., 1999. A proposal of the Temporal Window Operation(TWO) method to remove high-frequency noises in AVHRR NDVI time series data. J. Japan Soc. Photogramm. Remote Sens. 38, 36–47. doi:10.4287/jsprs.38.5_36

Pelletier, J.D., Swetnam, T.L., 2017. Asymmetry of weathering-limited hillslopes: the importance of diurnal covariation in solar insolation and temperature. Earth Surface Processes and Landforms, 42, 1408-1418. doi:10.1002/esp.4136

Penna, D., Tromp-van Meerveld, H.J., Gobbi, A., Borga, M., Dalla Fontana, G., 2011. The influence of soil moisture on threshold runoff generation processes in an alpine headwater catchment. Hydrol. Earth Syst. Sci. 15, 689–702. doi:10.5194/hess-15-689-2011

Piani, C., Haerter, J.O., Coppola, E., 2010a. Statistical bias correction for daily precipitation in regional climate models over Europe. Theor. Appl. Climatol. 99, 187–192. doi:10.1007/s00704-009-0134-9

Piani, C., Weedon, G.P., Best, M., Gomes, S.M., Viterbo, P., Hagemann, S., Haerter, J.O., 2010b. Statistical bias correction of global simulated daily precipitation and temperature for the application of hydrological models. J. Hydrol. 395, 199–215. doi:10.1016/J.JHYDROL.2010.10.024

Probst, J.L., Tardy, Y., 1987. Long range streamflow and world continental runoff fluctuations since the beginning of this century. J. Hydrol. 94, 289–311. doi:10.1016/0022-1694(87)90057-6

QIU, G.Y., Momii, K. and Yano, T., 1996. Estimation of plant transpiration by imitation leaf temperature. Transactions of the Japanese society of irrigation, Drainage and Reclamation Engineering, 1996(183), 401-410. doi:10.11408/jsidre1965.1996.401

Qiu, G.Y., Momii, K., Yano, T. and Lascano, R.J., 1999. Experimental verification of a mechanistic model to partition evapotranspiration into soil water and plant evaporation. Agricultural and Forest Meteorology, 93(2), 79-93. doi:10.1016/S0168-1923(98)00115-4

Qiu, G.Y., Momii, K., Yano, T., 1996. Estimation of plant transpiration by imitation leaf temperature - theoretical consideration and field verification (I). Trans of JSDIRE 183, 47–56.

Qiu, G.Y., Yano, T. and Momii, K., 1998. An improved methodology to measure evaporation from bare soil based on comparison of surface temperature with a dry soil surface. Journal of Hydrology, 210(1-4), 93-105. doi:10.1016/S0022-1694(98)00174-7

Qiu, G.Y., Yano, T., Momii, K., 1998. An improved methodology to measure evaporation from bare soil based on comparison of surface temperature with a dry soil surface. J. Hydrol. 210, 93–105. doi:10.1016/S0022-1694(98)00174-7

Rafiei Emam, A., Kappas, M., Linh, N., Renchin, T., 2017. Hydrological modeling and runoff mitigation in an ungauged basin of Central Vietnam using SWAT Model. Hydrology 4, 16. doi:10.3390/hydrology4010016

Razagui, A., Bachari, N.I., Bouchouicha, K., Hadj Arab, A., 2017. Modeling the global solar radiation under cloudy sky using Meteosat second generation high resolution visible raw data. Journal of the Indian Society of Remote Sensing, 45, 725-732. doi:10.1007/s12524-016-0628-8

Reichle, R.H., 2008. Data assimilation methods in the Earth sciences. Adv. Water Resour. 31, 1411–1418. doi:10.1016/J.ADVWATRES.2008.01.001

Reigber, C., Balmino, G., Schwintzer, P., Biancale, R., Bode, A., Lemoine, J.-M., König, R., Loyer, S., Neumayer, H., Marty, J.-C., Barthelmes, F., Perosanz, F., Zhu, S.Y., 2002. A high-quality global gravity field model from CHAMP GPS tracking data and accelerometry (EIGEN-1S). Geophys. Res. Lett. 29, 37-1-37–4. doi:10.1029/2002GL015064

Ren, J., Chen, Z., Zhou, Q., Tang, H., 2008. Regional yield estimation for winter wheat with MODIS-NDVI data in Shandong, China. Int. J. Appl. Earth Obs. Geoinf. 10, 403–413. doi:10.1016/J.JAG.2007.11.003

Renée Brooks, J., Barnard, H.R., Coulombe, R., McDonnell, J.J., 2010. Ecohydrologic separation of water between trees and streams in a Mediterranean climate. Nat. Geosci. 3, 100–104. doi:10.1038/ngeo722

Reynolds, S.G., 1970. The gravimetric method of soil moisture determination Part I A study of equipment, and methodological problems. J. Hydrol. 11, 258–273. doi:10.1016/0022-1694(70)90066-1

Rodell, M., Houser, P.R., Jambor, U., Gottschalck, J., Mitchell, K., Meng, C.-J., Arsenault, K., Cosgrove, B., Radakovich, J., Bosilovich, M., Entin, J.K., Walker, J.P., Lohmann, D., Toll, D., 2004. The Global Land Data Assimilation System. Bull. Am. Meteorol. Soc. 85, 381–394. doi:10.1175/BAMS-85-3-381

Rodríguez-Amigo, M.C., Díez-Mediavilla, M., González-Peña, D., Pérez-Burgos, A., Alonso-Tristán, C., 2017. Mathematical interpolation methods for spatial estimation of global

horizontal irradiation in Castilla-León, Spain: A case study. Solar Energy, 151, 14-21. doi:10.1016/j.solener.2017.05.024

Roerink, G J, Menenti, M., Verhoef, & W., 2000. Reconstructing cloudfree NDVI composites using Fourier analysis of time series. Int. J. Remote Sens. 21, 1911–1917. doi:10.1080/014311600209814

Roerink, G. J., Menenti, M., Verhoef, W., 2000. Reconstructing cloudfree NDVI composites using Fourier analysis of time series. Int. J. Remote Sens. 21, 1911–1917. doi:10.1080/014311600209814

Roerink, G.J., Menenti, M., Soepboer, W., Su, Z., 2003. Assessment of climate impact on vegetation dynamics by using remote sensing. Phys. Chem. Earth, Parts A/B/C 28, 103–109. doi:10.1016/S1474-7065(03)00011-1

Rosenberg, N.J., Blaine, L., Shashi, B.V., 1983. Microclimate: The biological environment. 2. Wiley, New York.

Runkle, B.R.K., Wille, C., Gažovič ,M., Wilmking, M., Kutzbach, L., 2014. The surface energy balance and its drivers in a boreal peatland fen of northwestern Russia. Journal of Hydrology, 511, 359-373. doi: 10.1016/j.jhydrol.2014.01.056

Samani, Z., Nolin, S., Bleiweiss, M., Skaggs, R., 2005. Discussion of "Predicting daily net radiation using minimum climatological data" by S. Irmak, A. Irmak, J. W. Jones, T. A. Howell, J. M. Jacobs, R. G. Allen, and G. Hoogenboom. J. Irrig. Drain. Eng. 9437, 2–13. doi:10.1061/(ASCE)0733-9437(2005)131

Sarkar, R., Dutta, S., Dubey, A.K., 2015. An insight into the runoff generation processes in wet sub-tropics: Field evidences from a vegetated hillslope plot. CATENA 128, 31–43. doi:10.1016/J.CATENA.2015.01.006

Savitzky, A., Golay, M.J.E., 1964. Smoothing and differentiation of data by simplified least squares procedures. Anal. Chem. 36, 1627–1639. doi:10.1021/ac60214a047

Scanlon, B.R., Zhang, Z., Rateb, A., Sun, A., Wiese, D., Save, H., Beaudoing, H., Lo, M.H., Müller-Schmied, H., Döll, P., Beek, R., Swenson, S., Lawrence, D., Croteau, M., Reedy, R.C., 2019. Tracking seasonal fluctuations in land water storage using global models and GRACE satellites. Geophys. Res. Lett. 46, 2018GL081836. doi:10.1029/2018GL081836

Shafer, S.L., Bartlein, P.J., Whitlock, C., 2005. Understanding the spatial heterogeneity of global environmental change in mountain regions. In: Global change and mountain regions: An overview of current knowledge. Springer, Dordrecht. doi:10.1007/1-4020-3508-x_3

Shangguan, W., Hengl, T., Mendes de Jesus, J., Yuan, H., Dai, Y., 2017. Mapping the global depth to bedrock for land surface modeling. J. Adv. Model. Earth Syst. 9, 65–88.

doi:10.1002/2016MS000686

Sharma, A., Kumar, K., Laskar, A., Singh, S.K., Mehta, P., 2017. Oxygen, deuterium, and strontium isotope characteristics of the Indus River water system. Geomorphology 284, 5–16. doi:10.1016/j.geomorph.2016.12.014

Sharma, R.D., Sarkar, R., Dutta, S., 2013. Run-off generation from fields with different land use and land covers under extreme storm events. Curr. Sci. 104, 1046–1053.

Shen, J., Huete, A., Tran, N.N., Devadas, R., Ma, X., Eamus, D., Yu, Q., 2018. Diverse sensitivity of winter crops over the growing season to climate and land surface temperature across the rainfed cropland-belt of eastern Australia. Agric. Ecosyst. Environ. 254, 99–110. doi:10.1016/J.AGEE.2017.11.023

Shougrakpam, S., Sarkar, R., Dutta, S., 2010. An experimental investigation to characterise soil macroporosity under different land use and land covers of northeast India. J. Earth Syst. Sci. 119, 655–674. doi:10.1007/s12040-010-0042-5

Shougrakpam, S., Sarkar, R., Dutta, S., 2010. An experimental investigation to characterise soil macroporosity under different land use and land covers of northeast India. J. Earth Syst. Sci. 119, 655–674. doi:10.1007/s12040-010-0042-5

Sivapalan, M., 2003. Process complexity at hillslope scale, process simplicity at the watershed scale: is there a connection? Hydrol. Process. 17, 1037–1041. doi:10.1002/hyp.5109

Sivapalan, M., Takeuchi, K., Franks, S.W., Gupta, V.K., Karambiri, H., Lakshmi, V., Liang, X., Mcdonnell, J.J., Mendiondo, E.M., O'connell, P.E., Oki, T., Pomeroy, J.W., Schertzer, D., Uhlenbrook, S., Zehe, E., 2003. 2003-2012: Shaping an exciting future for the hydrological sciences. Hydrol. Sci. J. 48, 857–880. doi:10.1623/hysj.48.6.857.51421

Sobrino, J.A., Jimenez-Munoz, J.C. and Paolini, L., 2004. Land surface temperature retrieval from LANDSAT TM 5. Remote Sensing of environment, 90(4), 434-440. doi:10.1016/j.rse.2004.02.003

Sobrino, J.A., Jiménez-Muñoz, J.C., Paolini, L., 2004. Land surface temperature retrieval from LANDSAT TM 5. Remote Sens. Environ. 90, 434–440. doi:10.1016/J.RSE.2004.02.003

Sood, A., Smakhtin, V., 2015. Global hydrological models: a review. Hydrol. Sci. J. 60, 549–565. doi:10.1080/02626667.2014.950580

Sprenger, M., Llorens, P., Cayuela, C., Gallart, F., Latron, J., 2019. Mechanisms of consistently disjunct soil water pools over (pore) space and time. Hydrol. Earth Syst. Sci. 23, 2751–2762. doi:10.5194/hess-23-2751-2019

Stökler, S., Schillings, C., Kraas, B., 2016. Solar resource assessment study for Pakistan. Renewable and Sustainable Energy Reviews, 58, 1184-1188. doi:10.1016/j.rser.2015.12.298

Stubenrauch, C.J., Rossow, W.B., Kinne, S., Ackerman, S., Cesana, G., Chepfer, H., Girolamo, L.D., Getzewich, B., Guignard, A., Heidinger, A., Maddux, B.C., Menzel, W.P., Minnis, P., Pearl, C., Platnick, S., Poulsen, C., Riedi, J., Sun-Mack, S., Walther, A., Winker, D., Zeng, S., Zhao, G., 2013. Assessment of global cloud datasets from satellites: Project and database initiated by the GEWEX Radiation Panel. Bulletin of the American Meteorological Society, 94, 1031-1049. doi:10.1175/bams-d-12-00117.1

Su, Z., 2002. The Surface Energy Balance System (SEBS) for estimation of turbulent heat fluxes. Hydrology and earth system sciences, 6(1), 85-100. doi:10.5194/hess-6-85-2002

Sun, L., Chen, Z., Gao, F., Anderson, M., Song, L., Wang, L., Hu, B., Yang, Y., 2017. Reconstructing daily clear-sky land surface temperature for cloudy regions from MODIS data. Comput. Geosci. 105, 10–20. doi:10.1016/J.CAGEO.2017.04.007

Sun, Q., Miao, C., Duan, Q., Ashouri, H., Sorooshian, S., Hsu, K., 2018. A review of global precipitation data sets: Data sources, estimation, and intercomparisons. Rev. Geophys. 56, 79–107. doi:10.1002/2017RG000574

Swift, L.W., Knoerr, K.R., 1973. Estimating solar radiation on mountain slopes. Agricultural Meteorology, 12, 329-336. doi:10.1016/0002-1571(73)90029-0

Swinbank, W.C., 1963. Long-wave radiation from clear skies. Q. J. R. Meteorol. Soc. 89, 339–348. doi:10.1002/qj.49708938105

Swinbank, W.C., 1963. Long-wave radiation from clear skies. Quarterly Journal of the Royal Meteorological Society, 89(381), 339-348. doi:10.1002/qj.49708938105

Szabó, S., Elemér, L., Kovács, Z., Püspöki, Z., Kertész, Á., Kumar Singh, S., Balázs, B., 2018. GIScience & Remote Sensing NDVI dynamics as reflected in climatic variables: spatial and temporal trends-a case study of Hungary. doi:10.1080/15481603.2018.1560686

Tapley, B.D., Bettadpur, S., Watkins, M., Reigber, C., 2004. The gravity recovery and climate experiment: Mission overview and early results. Geophys. Res. Lett. 31, n/a-n/a. doi:10.1029/2004GL019920

Testa, S., Soudani, K., Boschetti, L., Borgogno Mondino, E., 2018. MODIS-derived EVI, NDVI and WDRVI time series to estimate phenological metrics in French deciduous forests. Int. J. Appl. Earth Obs. Geoinf. 64, 132–144. doi:10.1016/J.JAG.2017.08.006

Tian, F., Qiu, G.Y., Yang, Y.H., Lü, Y.H., Xiong, Y., 2013. Estimation of evapotranspiration and its partition based on an extended three-temperature model and MODIS products. J. Hydrol. 498, 210–220. doi:10.1016/j.jhydrol.2013.06.038

Torres, R., Dietrich, W.E., Montgomery, D.R., Anderson, S.P., Loague, K., 1998. Unsaturated zone processes and the hydrologic response of a steep, unchanneled catchment. Water Resour. Res. 34, 1865–1879. doi:10.1029/98WR01140

Tovar-Pescador, J., Pozo-Vázquez, D., Ruiz-Arias, J.A., Batlles, J., López, G., Bosch, J.L., 2006. On the use of the digital elevation model to estimate the solar radiation in areas of complex topography. Meteorological Applications, 13, 279-287. doi:10.1017/S1350482706002258

Tran, Hoa Thi, Campbell, J.B., Tran, T.D., Tran, Ha Thanh, 2017. Monitoring drought vulnerability using multispectral indices observed from sequential remote sensing (Case Study: Tuy Phong, Binh Thuan, Vietnam). GIScience Remote Sens. 54, 167–184. doi:10.1080/15481603.2017.1287838

Tromp Van Meerveld, I., McDonnell, J.J., 2005. Comment to "Spatial correlation of soil moisture in small catchments and its relationship to dominant spatial hydrological processes, Journal of Hydrology 286: 113–134. J. Hydrol. doi:10.1016/j.jhydrol.2004.09.002

Tucker, C.J., 1979. Red and photographic infrared linear combinations for monitoring vegetation. Remote Sens. Environ. 8, 127–150. doi:10.1016/0034-4257(79)90013-0

Van Dam, J.C., Groenendijk, P., Hendriks, R.F.A., Kroes, J.G., 2008. Advances of modeling water flow in variably saturated soils with SWAP. Vadose Zone J., 7, 640–653. doi:10.2136/vzj2007.0060

Van Stiphout, T.P.J., Van Lanen, H.A.J., Boersma, O.H., Bouma, J., 1987. The effect of bypass flow and internal catchment of rain on the water regime in a clay loam grassland soil. J. Hydrol. 95, 1–11. doi:10.1016/0022-1694(87)90111-9

Verbesselt, J., Hyndman, R., Newnham, G., Culvenor, D., 2010. Detecting trend and seasonal changes in satellite image time series. Remote Sens. Environ. 114, 106–115. doi:10.1016/j.rse.2009.08.014

Verdhen, A., Chahar, B.R., Sharma, O.P., 2014. Snowmelt modelling approaches in watershed models: Computation and comparison of efficiencies under varying climatic conditions. Water Resources Management, 28, 3439-3453. doi:10.1007/s11269-014-0662-7

Verhegghen, A., Bontemps, S., Defourny, P., 2014. A global NDVI and EVI reference data set for land-surface phenology using 13 years of daily SPOT-VEGETATION observations. Int. J. Remote Sens. 35, 2440–2471. doi:10.1080/01431161.2014.883105

Verhoef, W., Menenti, M., Azzali, S., 1996. Cover A colour composite of NOAA-AVHRR-NDVI based on time series analysis (1981-1992). Int. J. Remote Sens. 17, 231–235. doi:10.1080/01431169608949001

Verma, R., Dutta, S., 2013. Vegetation dynamics from denoised NDVI using empirical mode decomposition. J. Indian Soc. Remote Sens. 41, 555–566. doi:10.1007/s12524-012-0246-z

Viovy, N., Arino, O., Belward, A.S., 1992. The Best Index Slope Extraction (BISE): A method for reducing noise in NDVI time-series. Int. J. Remote Sens. 13, 1585–1590. doi:10.1080/01431169208904212

Vourlitis, G.L., de Souza Nogueira, J., de Almeida Lobo, F., Pinto, O.B., 2015. Variations in evapotranspiration and climate for an Amazonian semi-deciduous forest over seasonal, annual, and El Niño cycles. International Journal of Biometeorology, 59, 217-230. doi:10.1007/s00484-014-0837-1

Vyas, S.S., Nigam, R., Bhattacharya, B.K., Kumar, P., 2016. Development of real-time reference evapotranspiration at the regional scale using satellite-based observations. International Journal of Remote Sensing, 37, 6108-6126. doi:10.1080/01431161.2016.1253895

Walthall, C., Dulaney, W., Anderson, M., Norman, J., Fang, H. and Liang, S., 2004. A comparison of empirical and neural network approaches for estimating corn and soybean leaf area index from Landsat ETM+ imagery. Remote Sensing of Environment, 92(4), 465-474. doi:10.1016/j.rse.2004.06.003

Wan, Z., 2014. New refinements and validation of the collection-6 MODIS land-surface temperature/emissivity product. Remote Sens. Environ. 140, 36–45. doi:10.1016/J.RSE.2013.08.027

Wang, J., Zhou, Y., Zhu, L., Gao, M., Li, Y., Wang, J., Zhou, Y., Zhu, L., Gao, M., Li, Y., 2014. Cultivated land information extraction and gradient analysis for a North-South transect in Northeast Asia between 2000 and 2010. Remote Sens. 6, 11708–11730. doi:10.3390/rs61211708

Wang, K., Dickinson, R.R.E., 2012. A review of global terrestrial evapotranspiration : Observation, modelling, climatology, and climatic variability. Rev. Geophys. 50, 1–54. doi:10.1029/2011RG000373.1.INTRODUCTION

Wei, P., Pan, X., Xu, L., Hu, Q., Zhang, X., Guo, Y., Shao, C., Wang, C., Li, Q., yin, Z., 2019. The effects of topography on aboveground biomass and soil moisture at local scale in dryland grassland ecosystem, China. Ecol. Indic. 105, 107–115. doi:10.1016/J.ECOLIND.2019.05.002

Weiler, M., 2017. Macropores and preferential flow—a love-hate relationship. Hydrol. Process. 31, 15–19. doi:10.1002/hyp.11074

Wen, J., Su, Z., 2004. An analytical algorithm for the determination of vegetation Leaf Area Index from TRMM/TMI data. Int. J. Remote Sens. 25, 1223–1234. doi:10.1080/01431160310001598962

Wen, Q., Zhang, Z., Liu, S., Wang, X., Wang, C., 2010. Classification of grassland types by MODIS time-series images in Tibet, China. IEEE J. Sel. Top. Appl. Earth Obs. Remote Sens. 3, 404–409. doi:10.1109/JSTARS.2010.2049001

Western, A.W., Grayson, R.B., Blöschl, G., Willgoose, G.R., McMahon, T.A., Bschl, G., Willgoose, G.R., 1999. Observed spatial organization of soil moisture inand its relation to terrain indices. Water Resour. Res. 35, 797–810. doi:10.1029/1998WR900065

Williams, J. R., Arnold, J. G. & Srinivasan, R. (2002) The APEX model, BRC Report No. 00–06. 121, Texas Agricultural Experiment Station, Blackland Research Centre, Texas A&M University, USA.

Xiao, X., Zhang, J., Yan, H., Wu, W., Biradar, C., 2009. Land surface phenology, in: Phenology of ecosystem processes. Springer New York, New York, NY, 247–270. doi:10.1007/978-1-4419-0026-5_11

Xiong, Y. jiu, Qiu, G. yu, 2011. Estimation of evapotranspiration using remotely sensed land surface temperature and the revised three-temperature model. Int. J. Remote Sens. 32, 5853–5874. doi:10.1080/01431161.2010.507791

Xiong, Y.J. and Qiu, G.Y., 2011. Estimation of evapotranspiration using remotely sensed land surface temperature and the revised three-temperature model. International Journal of Remote Sensing, 32(20), 5853-5874. doi:10.1080/01431161.2010.507791

Xu, L., Li, B., Yuan, Y., Gao, X., Zhang, T., Xu, L., Li, B., Yuan, Y., Gao, X., Zhang, T., 2015. A temporal-spatial iteration method to reconstruct NDVI time series datasets. Remote Sens. 7, 8906–8924. doi:10.3390/rs70708906

Xu, Y., Shen, Y., 2013. Reconstruction of the land surface temperature time series using harmonic analysis. Comput. Geosci. 61, 126–132. doi:10.1016/J.CAGEO.2013.08.009

Yang, J., Pan, S., Dangal, S., Zhang, B., Wang, S., Tian, H., 2017. Continental-scale quantification of post-fire vegetation greenness recovery in temperate and boreal North America. Remote Sens. Environ. 199, 277–290. doi:10.1016/J.RSE.2017.07.022

Yu, W., Nan, Z., Wang, Z., Chen, H., Wu, T., Zhao, L., 2015. An effective interpolation method for MODIS land surface temperature on the Qinghai–Tibet plateau. IEEE J. Sel. Top. Appl. Earth Obs. Remote Sens. 8, 4539–4550. doi:10.1109/JSTARS.2015.2464094

Zeng, Q., Wang, Y., Chen, L., Wang, Z., Zhu, H., Li, B., 2018. Inter-Comparison and evaluation of remote sensing precipitation products over China from 2005 to 2013. Remote Sens. 10, 168. doi:10.3390/rs10020168

Zhao, S., Yang, Y., Qiu, G., Qin, Q., Yao, Y., Xiong, Y. and Li, C., 2010. Remote detection of bare soil moisture using a surface-temperature-based soil evaporation transfer coefficient. International Journal of Applied Earth Observation and Geoinformation, 12(5), 351-358. doi:10.1016/j.jag.2010.04.007

Zhou, J., Jia, L., Menenti, M., 2015. Reconstruction of global MODIS NDVI time series: performance of harmonic analysis of time series (HANTS). Remote Sens. Environ. 163, 217–228. doi:10.1016/j.rse.2015.03.018

Zhou, J., Jia, L., Menenti, M., Gorte, B., 2016. On the performance of remote sensing time series reconstruction methods – A spatial comparison. Remote Sens. Environ. 187, 367–384. doi:10.1016/j.rse.2016.10.025

Zhou, W., Peng, B., Shi, J., 2017. Reconstructing spatial–temporal continuous MODIS land surface temperature using the DINEOF method. J. Appl. Remote Sens. 11, 1. doi:10.1117/1.JRS.11.046016

Zhu, W., Pan, Y., He, H., Wang, L., Mou, M., Liu, J., 2012. A Changing-Weight filter method for reconstructing a high-quality NDVI time series to preserve the integrity of vegetation phenology. IEEE Trans. Geosci. Remote Sens. 50, 1085–1094. doi:10.1109/TGRS.2011.2166965

Horton, R.E., 1932. Drainage basin characteristics. Am. Geophys.Union, Trans. 13, 348–352.

Horton, R.E., 1945. Erosional development of streams and their drainage basins; hydrophysical approach to quantitative morphology. Geol. Soc. Am. Bull. 56, 275–370.

Martinec, J., Rango, A., Roberts, R., 2008. WinSRM 1.11—snowmelt runoffmodel user's manual. ABD, Editörler: Gomez-Landesa E. ve Bleiweiss, PM, New Mexico State University, Las Cruces, New Mexico, USA.

Appendix

A1. Parameter setting for HANTS

Many studies have been conducted to analyse the properties of parameters of HANTS (Azzali and Menenti, 2000; Geerken et al., 2005; Verhegghen et al., 2014). HANTS parameters need to be set on the basis of experience for different time-series (Roerink et al., 2000). The implementation of HANTS includes fitting parameters to be set carefully when the algorithm is applied on different time-series and regions. There are seven basic user-defined parameters of HANTS for a reliable fitting curve:

(1) Number of time samples corresponding to predefined frequencies (nb) – it controls the temporal length of each term in the Fourier series;
(2) Number of Frequencies (nf) – the number of harmonic terms. Complex time arrangement information might require higher order for the Fourier fit to replicate the annual NDVI curves;
(3) Valid data range (low and high thresholds) – the range of the input variables values;
(4) Fit error tolerance (fet) – it is the value which controls the iterations according to whether observations in the times series are within a tolerable distance from the fitting curve;
(5) Degree of overdeterminedness (dod) – it specifies the extra data points for a reliable fit more than the minimum points needed (ideally, $2 \times nf - 1$);
(6) Damping factor (delta) – it is a small positive number to suppress high amplitudes which might be caused due to atmospheric disturbances;
(7) Flag direction of outliers (Hi/Lo/HiLo) – it is used to indicate the direction of unreasonable values "outliers" with respect to the curve.

The best time sample (nb) for the study area was found as "45" by trial attempts and number of frequencies (nf) was set to a high number of 4^{th} harmonics. Targeting on vegetated areas, low value of "0" and high value of "1" were set. Other parameters were set in accordance with works of Zhou et al. (2015) as shown in Table A1.1.

Table A1.1. HANTS parameter settings applied in this study.

Parameter	Notation	Value
Number of time samples corresponding to predefined frequencies	nb	45
Number of frequencies considered in curve fitting	nf	4
Low threshold	low	0
High threshold	high	1
Fit error tolerance	fet	0.05
Degree of overdeterminedness	dod	5
Damping factor	delta	0.5
Flag to indicate the direction of outliers with respect to curve	HiLo	none

A2. Search and fill algorithm (SFA)

In this work, for a pixel with static LULC, we had only 16 observations to find one value for $NDVI_{ref}$ and 23 such values on temporal positions represent its annual curve. There are chances of unavailability of NDVI data to compute complete $NDVI_{ref}$ for many pixels with this limitation. It could lead to faulty representation of $SNDVI_{ref}$ in later stages. The availability of correct $SNDVI_{ref}$ for each pixel is important for implementation of the proposed pre-filling method (section 3.4.2). Moreover, total NDVI observations at a pixel is supposed to get divided to produce more than one $NDVI_{ref}$ curves with dynamic LULC. It further reduces the NDVI observations for preparation of $NDVI_{ref}$ in pixels with dynamic LULC. Therefore, pixels having $NDVI_{ref}$ affected with null values was a major problem and required to be restored.

Yang et al. (2017) has reported that vegetation in same ecoregion faces similar climate and human conditions. It can cause similar phenology of vegetation if their conditions are similar. So, extraction of the phenological pattern is often used as a key feature in LULC classification methods (Friedl et al., 2002; Padhee et al., 2017). These hints were used to restore the affected $NDVI_{ref}$ curves by a recursive SFA with a moving window of user-defined size (W). Flow diagram of recursive SFA to restore affected $NDVI_{ref}$ curves. The algorithm uses additional physical evidences drawn from similarity in $NDVI_{ref}$ of another pixel with same LULC within the window having adequate valid values on its curve (or reference pixel). Since, $NDVI_{ref}$ is a curve by nature, the similarity in phenological traits of two pixels could be indicated by their

linear relationship. This relationship is represented mathematically by coefficient of correlation (R) between their $NDVI_{ref}$ curves.

Certain selection conditions are defined in the algorithm to search for nominee pixels to become a reference pixel, i.e. $NDVI_{ref}$ at a pixel (*a, b*) with valid values to restore affected $NDVI_{ref}$ at the target pixel, i.e. $NDVI_{ref}$ at (*i, j*). The selection conditions for nominee pixels are listed as follows.

(1) LULC of target and nominee pixel must be same.

(2) Coefficient of correlation between target and nominee pixels within the window must be more than limit ($L \geq 0.9$).

(3) Percentage of valid data at nominee pixel must be more than that of target pixel.

(4) There must not be null data in both the target and nominee pixel at same temporal position, *k*.

Out of all nominee pixels listed within the window, pixel having highest R value with the target pixel is finalized as the reference pixel (pixel with most similar conditions). Later, $NDVI_{ref}$ curves from reference and target pixels are used in Eq. 6 to draw out coefficients of their linear regression and utilized to restore $NDVI_{ref}$ curve in target pixel as shown in Eq. A2.1 and A2.2.

$$\mathrm{NDVI}_{ref}^{i,j} = m\mathrm{NDVI}_{ref}^{a,b} + \mathrm{C} \tag{A2.1}$$

$$\mathrm{NDVI}_{ref,k}^{i,j} = m\mathrm{NDVI}_{ref,k}^{a,b} + C \tag{A2.2}$$

where, (*i,j*) is spatial location of target pixel, (*a,b*) is the spatial location of reference pixel within the window, *m* and *c* are the slope and the intercept for the linear regression between target and reference pixel, and *k* is the temporal position of target pixel affected with null data. Since, linear regression is used to restore $NDVI_{ref}$ at target pixel, the restored value might exceed the maximum value of 1 due to which reference pixel is selected which yields a value between 0 and 1. Also, an additional constraint as threshold ($T \geq 50\%$) is considered below which $NDVI_{ref}$ having percentage of valid values is rejected as target and skipped due to weak statistics. A typical demonstration of restoration of $NDVI_{ref}$ is presented in Fig. A2.1. Restoration of affected $NDVI_{ref}$ curves throughout the study area was achieved in two stages

depending upon static and dynamic LULC in 16 years (2001 – 2016). In SFA, the window with target pixel at its centre is moved in a recursive manner throughout the study area. Its recursion starts by restoring affected $NDVI_{ref}$ at pixels over 95% valid data and stepping down to 5% with each recursion till pixels with $NDVI_{ref}$ over 50% valid data is reached. The number of recursions and pixels required for $NDVI_{ref}$ depends upon the severity of temporal and spatial NDVI data deficiency respectively. The recursive SFA is shown as a part of methodology for NDVI time-series reconstruction in Fig.3.2 and its detailed flowchart is given in Fig.A2.2.

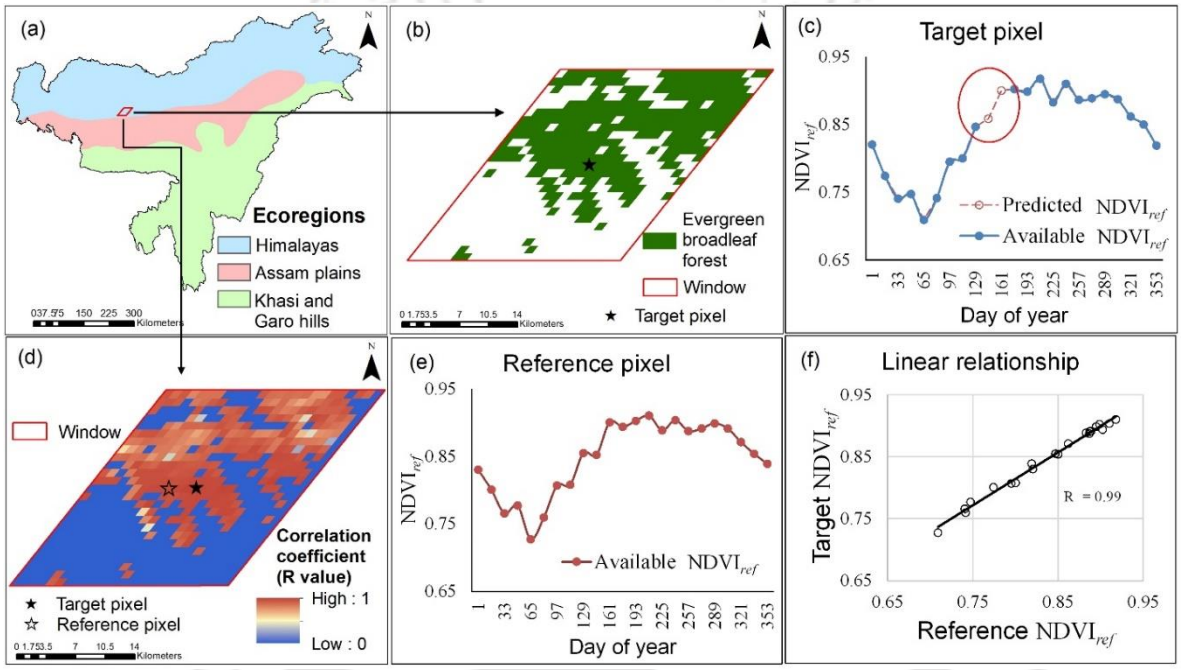

Figure. A2.1. Restoration of affected $NDVI_{ref}$ for the pixels with static LULC was achieved in the first stage.

It was followed by second stage where pixels with dynamic LULC were targeted. In the second stage, pixels with more than four LULC in 16 years were not considered as target pixels due to insufficient NDVI observations to begin with. During the process of restoration, newly produced synthetic values in restored $NDVI_{ref}$ at any pixel were made accessible for being a nominee in the restoration of other affected pixels. The recursive search and fill process ensures equitable availability of valid values in $NDVI_{ref}$. However, definition of *W*, *T* and *L* is dependent upon availability of NDVI data, and hence it is customized as user-defined variables.

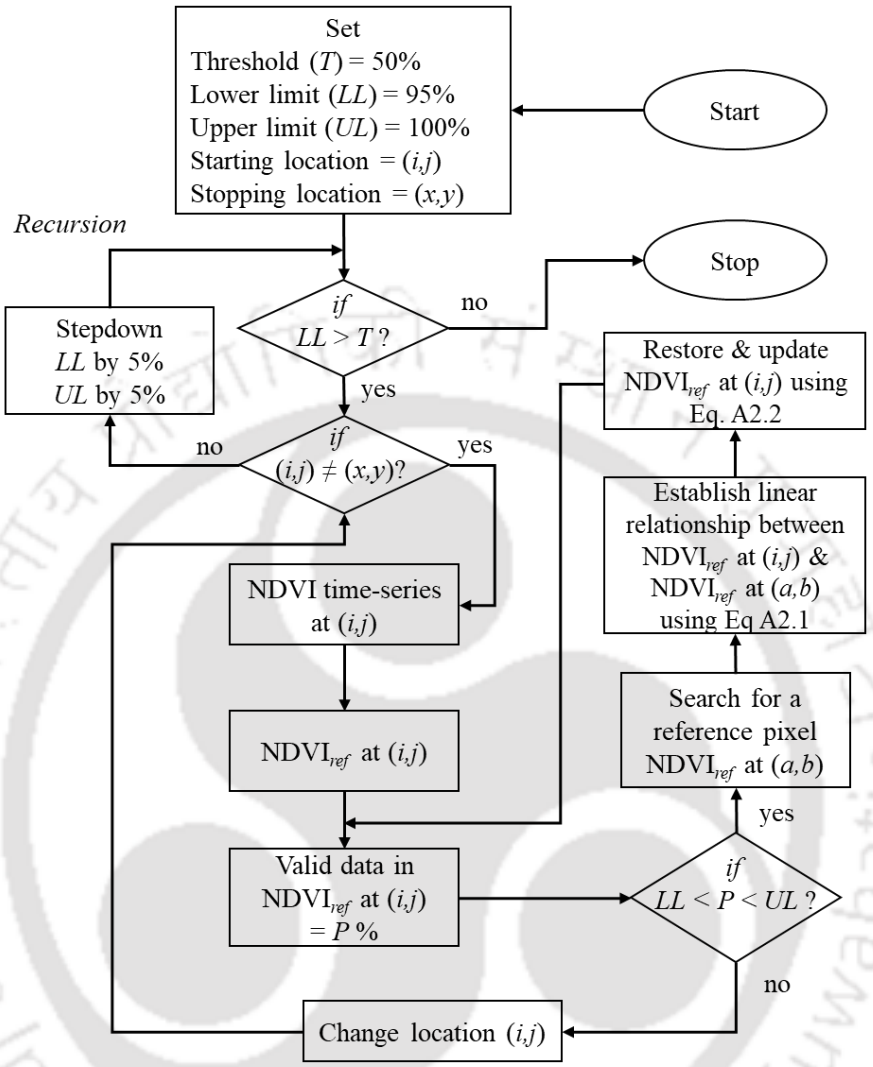

Fig. A2.2. Flow chart of recursive search and fill algorithm used for restoration of reference phenology curve ($NDVI_{ref}$).

A3. Three-Temperature Model

The basic concept for 3T model is surface energy balance. It is assumed for this model that the land cover consists of three groups which are bare soil, vegetation and a mixture of both soil and vegetation. Algorithms have been established by Qui et al. (1996) and Qui et al. (1998) to calculate ET for areas having bare soil and vegetation respectively. Also, algorithm to calculate ET for mixture of both soil and vegetation has been established by Xiong et al. (2011) using fractional vegetation cover which quantifies the presence of vegetation cover.

According to the general energy balance equation, energy exchange on earth surface can be express as:

$$LE = R_n - G - H \tag{A3.1}$$

where L is the latent heat of vaporization with value 2.49×10^6 $W/(m^2 mm)$; LE is the latent heat flux; and E is the soil evaporation in mm; R_n is the net radiation at the soil surface; G is soil heat flux. Units of LE, R_n and G are in W/m^2. H is the sensible heat flux between land and atmosphere in W/m^2 which can be derived from the following equation as:

$$H = \frac{\rho C_p (T_s - T_a)}{r_a} \tag{A3.2}$$

where ρ is the air density in kg/m^3, C_P is the specific heat at constant pressure in $MJ/(kg\,°C)$; T_s and T_a are soil surface temperature and air temperature respectively in °C; r_a is the aerodynamic resistance in s/m, the diffusion resistance of the air layer. In presence of a reference surface of dry soil with no significant modification in atmospheric conditions around it, the r_a of the dry soil and the r_a of the drying soil are approximately equal to each other; such conditions implies no water is in the dry soil and LE is negligible, hence the r_a can be evaluated by combining Eq.A3.1 and Eq.A3.2 as Qui et al. (1999):

$$r_a = \frac{\rho C_p (T_{sd} - T_a)}{R_{n,d} - G_d} \tag{A3.3}$$

where T_{sd} is the reference dry soil temperature, and $R_{n,d}$ and G_d are the net radiation and soil heat flux respectively for the reference dry soil. Thus, by combining Eq.A3.1, Eq.A3.2 and Eq.A3.3, soil evaporation (LE_s) can be estimated for pixels having pure soil as:

$$LE_s = R_{n,sm} - G - (R_{n,d} - G_d)\frac{(T_s - T_a)}{(T_{sd} - T_a)} \tag{A3.4}$$

where T_s is the temperature and $R_{n,sm}$ is the net radiation of the soil. Similarly, by introduction of a canopy without transpiration (imitation canopy), r_a of the vegetation could be estimated using the formula:

$$r_a = \frac{\rho C_p (T_{sd} - T_a)}{R_{n,cp}} \quad \text{(A3.5)}$$

where T_{cp} is the temperature and $R_{n,cp}$ is net radiation of the imitation canopy. Thus, by combining Eq.A3.1, Eq. A3.2 and Eq.A3.5, vegetation transpiration (LE_c) can be estimated for pixels having pure vegetation:

$$LE_c = R_{n,sm} - R_{n,cp} \frac{(T_c - T_a)}{(T_{cp} - T_a)} \quad \text{(A3.6)}$$

where T_c is the temperature and $R_{n,cm}$ is the net radiation of the vegetation canopy. Eq.A3.4 - A3.6 are the basic equations for computation of evaporation and transpiration and can only be used in case of pure pixels. The computation of evapotranspiration for the mixed region of soil and vegetation can be done by using fractional canopy coverage factor. Evapotranspiration in mixed pixels can be considered as:

$$LET = (1-f)\, LE_s + f\, LE_c \quad \text{(A3.7)}$$

where f is the fractional canopy coverage factor and can be calculated by the equation established by Carlson et al. (1995) as:

$$f = \frac{(NDVI - NDVI_{min})}{(NDVI_{max} - NDVI_{max})} \quad \text{(A3.8)}$$

NDVI is the Normalized Difference Vegetation Index. Agam et al. (2007) have established the thresholds $NDVI_{max}$ and $NDVI_{min}$ selection method, in which these can be calculated from the lower and upper 3% tails of the NDVI distribution within the scene.

The dominance of a pixel going for only soil evaporation, only vegetation transpiration or evapotranspiration at a pixel depends upon category of the particular pixel. The category of pixels can be distinguished into pure or mixed pixel by using NDVI. Pixels with an NDVI larger

than the $NDVI_{max}$ are assumed to be pixel definitely containing pure vegetation cover; pixels with an NDVI less than the $NDVI_{min}$ can be assumed to be covered by bare soil; pixels with a NDVI lying between $NDVI_{min}$ and $NDVI_{max}$ are assumed to be mixed pixels Carlson et al. (1995).

In Eq.A3.1, R_n and G are the two parts which need to be estimated in order to compute LE. Eq.A3.1 is modified to Eq.A3.4 for soil and Eq.A3.6 for vegetation, out of which Eq.A3.4 requires estimation of R_n and G. Unlike Eq.A3.4, G is not required to be estimated in Eq.A3.6. However to compute Eq.A3.4 or Eq.A3.6, the land surface temperature needs to be separated for soil and vegetation. The entire procedure to calculate LE_s and LE_c can be listed as follows.

Net radiation

The net radiation (R_n) can be expressed as:

$$R_n = (R_{swd} - R_{swu}) + (R_{lwd} - R_{lwu}) \quad \text{(A3.9)}$$

where R_{swd} and R_{swu} represents the incoming and outgoing shortwave radiation respectively; R_{lwd} and R_{lwu} represents the incoming and outgoing longwave radiation respectively. Using the estimated R_{swd} from GLDAS downscaled product (section 5.2.1), the net shortwave radiation can be calculated as:

$$R_{swd} - R_{swu} = (1-\alpha) R_{swd} \quad \text{(A3.10)}$$

$$\alpha = 0.160\alpha_1 + 0.291\alpha_2 + .243\alpha_3 + 0.116\alpha_4 + 0.112\alpha_5 + 0.081\alpha_6 - 0.0015 \quad \text{(A3.11)}$$

where α is the surface albedo that can be calculated as Eq.A3.11, Liang (2001). $\alpha_1, \alpha_2, \alpha_3, \alpha_4, \alpha_5$ and α_7 are the reflectance of bands 1, 2, 3, 4, 5 and 7 respectively. The net longwave radiation can be expressed as:

$$R_{lwd} - R_{lwu} = \sigma\varepsilon_o\varepsilon_a (T_a + 273.15)^4 - \sigma\varepsilon_o T_s^4 \quad \text{(A3.12)}$$

$$\varepsilon_a = 9.2\times10^{-6}\,(T_a + 273.15)^2 \qquad \text{(A3.13)}$$

$$\begin{cases} \begin{cases} \varepsilon_o = 0.9832 - 0.058\rho_1 \\ \Delta\varepsilon_o = 0.0018 - 0.060\rho_1 \end{cases} & \text{NDVI} < 0.2 \\ \begin{cases} \varepsilon_o = 0.9710 - 0.018\,f \\ \Delta\varepsilon_o = -0.006\,(1-f) \end{cases} & 0.2 < \text{NDVI} < 0.5 \\ \begin{cases} \varepsilon_o = 0.9900 \\ \Delta\varepsilon_o = 0 \end{cases} & \text{NDVI} < 0.5 \end{cases} \qquad \text{(A3.14)}$$

where σ is the Stefan–Boltzmann constant with a value of (5.67×10^{-8} W/m^2); ε_a is the atmospheric emissivity and can be calculated from Eq.A3.13, Swinbank (1963); ε_0 is the surface emissivity that can be calculated depending upon the NDVI value, Eq. A3.14, Sobrino et al. (2004); and ρ_1 is the reflectivity acquired from band 1 (red band region) of MODIS.

The estimated R_n is the overall absorbed net radiation. For mixed pixels R_n needs to be separated in terms of net radiation absorbed by soil surface and vegetation canopy as:

$$R_{n,sm} = R_n \exp(-0.45LAI) \qquad \text{(A3.15)}$$

$$R_{n,cm} = R_n\,[1 - \exp(-0.45LAI)] \qquad \text{(A3.16)}$$

$$LAI = -2\ln(1-f) \qquad \text{(A3.17)}$$

where R_n is the mixed net radiation absorbed by features in the pixel; $R_{n,sm}$ is the net radiation absorbed by soil surface; $R_{n,cm}$ is the net radiation absorbed by vegetation canopy; LAI is the leaf area index. The LAI can be derived from f as shown in Eq.A3.17, Walthall et al. (2004). $R_{n,sm}$ and $R_{n,cm}$ can be further implemented in Eq.A3.4 and Eq.A3.6. Net radiation for the reference surfaces i.e. reference dry soil ($R_{n,d}$) and imitation canopy ($R_{n,cp}$) can be expressed as:

$$R_{n,d} = (1-\alpha_{r,d})\,R_{swd} + \varepsilon_{0,d}\varepsilon_a\sigma T_a^{\,4} - \sigma\varepsilon_{0r}T_s^{\,4} \qquad \text{(A3.18)}$$

$$R_{n,cp} = (1-\alpha_{r,cp})\, R_{swd} + \varepsilon_{0\,r,cp}\, \varepsilon_a \sigma T_a^{\,4} - \sigma \varepsilon_{0r} T_s^{\,4} \quad \text{(A3.19)}$$

where empirical coefficients $\alpha_{r,d} = 0.275$, Qui et al. (1998); $\alpha_{r,cp} = 0.225$, Qui et al. (1996); $\varepsilon_{0r,d} = 0.970$ and $\varepsilon_{0r,cp} = 0.99$, Sobrino et al. (2004). $R_{n,d}$ and $R_{n,cp}$ can be further implemented in Eq.A3.4 and Eq.A3.6.

Soil heat flux

The soil heat flux (G) can be estimated as per the established equation in the work by Su (2002):

$$G = R_n .[\Gamma_c + (1-f).(\Gamma_s - \Gamma_c) \quad \text{(A3.20)}$$

where the empirical coefficients $\Gamma_c = 0.05$, Monteith (1973) and $\Gamma_s = 0.315$, Kustas and Daughtry (1990). And the soil heat flux for reference dry soil (G_d) can be expressed as:

$$G_d = 0.315 R_{n,d} \quad \text{(A3.21)}$$

G and G_d can be further implemented in Eq.A3.4 to calculate soil evaporation (LE_s).

Land surface temperature separation

The estimation of LE_s and LE_c requires the separation of the land surface temperature which represents mixed temperature. The components of (T_s) are temperature of soil (T_{sm}) and vegetation (T_{cm}) to be implemented in Eq.A3.4 and Eq.A3.6 respectively. It can be sepsrated by solving the following set of equations suggested by Lhomme et al. (1994), which are:

$$fT_{cm} + (1-f)T_{sm} = T_s \quad \text{(A3.22)}$$

$$T_{sm} - T_{cm} = a(T_s - T_a)^m \quad \text{(A3.23)}$$

where T_s is the mixed land surface temperature; $a = 0.1$ and $m = 2$ are the empirical coefficients, Lhomme et al. (1994). The temperature for reference dry soil (T_{sd}) for Eq.A3.4 and imitation canopy (T_{cp}) for Eq.A3.6, can be allocated as the maximum temperatures of soil

and vegetation obtained respectively from Eq.A3.22 and Eq.A3.23 as proposed by Zhao et al. (2010).

A4. Macropore geometry computation

The macropore geometry is computed by three properties viz. continuity, persistency and horizontal distribution. Continuity controls of water flow entering the macropores along the vertical and horizontal directions. Persistency defines static and dynamic macropore volume. However, for a largescale model, only static macropores are considered. Horizontal distribution in the horizontal plane describes the distribution of macropore volume over horizontal plane.

Continuity

The macropore volumetric proportion of the two domains, main bypass (V_{mb}) and internal catchments (V_{ic}) are functions of depth as represented in Eq. 6.1 and the detailed description of parameters required for its computation (shown in Table 6.2).

$$P_{mb} = 1 - P_{ic} \tag{A4.1}$$

$$R = R_{zAh} * \left(\frac{Z}{Z_{Ah}} \right) \qquad \text{for } 0 \geq z \geq Z_{Ah} \tag{A4.2}$$

$$R = R_{Zah} + \left(1 - R_{Zah}\right) \left[\left\{ \left(Z_{Ah} - Z \right) / \left(Z_{Ah} - Z_{ic} \right) \right\}^{m} \right] \qquad \text{for } Z_{Ah} \geq z \geq Z_{ic} \tag{A4.3}$$

Here, the depths z, Z_{Ah} and Z_{ic} are defined as active depth, depth of A-horizon and depth of active IC domain respectively. The power m is a shape-factor where (m < 1), (m > 1), and (m = 1) represents shallow, deep and intermediate IC system as a decline of functional IC macropores with depth. R_{ZAh} is a parameter with which increase of the volumetric distribution curve (R) over the thickness of the A-horizon can be described. Curve (F) represents the fraction of IC macropores (Eq. 6.4) that is functional at that depth z, the complement of R curve in general. The volumetric proportion of IC macropore volume as a function of depth can be written in terms of the constant $P_{ic,0}$ and the function F as shown in Eq. 6.5 and 6.6. P_{ic0} represents volumetric proportion of IC at soil surface (cm^3/cm^3). The volumetric proportion of

MB macropore volume as a function of depth is calculated from function P_{ic} with Eq. 6.1. This results in a proportion P of 1 for depths below Z_{ic} where IC macropore volume is absent and all macropore volume is MB volume.

$$F = 1 - R \tag{A4.4}$$

$$P_{ic} = \frac{F}{\left[\left(\frac{1}{P_{ic0}}\right) + F - 1\right]} \qquad \text{for } 0 \geq z \geq Z_{ic} \text{ and } 0 \leq P_{ic0} \leq 1 \tag{A4.5}$$

$$P_{ic} = 0 \qquad \text{for } z \leq Z_{ic} \text{ and/or for } P_{ic0} = 0 \tag{A4.6}$$

Persistency

Static macropore volume is permanent the permanent MB and IC. It is expressed as volume fraction V_{st} (cm^3/cm^3). The static volume as a function of depth is constant in time and it is calculated as shown in Eq. 6.7 to 6.11.

$$V_{stmb} = V_{stmb0} \qquad \text{for } 0 \geq z \geq Z_{ic} \tag{A4.7}$$

$$V_{stmb} = V_{stmb0}\left[\left(Z - Z_{st}\right)/\left(Z_{ic} - Z_{st}\right)\right] \qquad \text{for } Z_{ic} \geq z \geq Z_{st} \tag{A4.8}$$

$$V_{stic} = F * V_{stic0} \qquad \text{for } 0 \geq z \geq Z_{ic} \tag{A4.9}$$

$$V_{stic} = 0 \qquad \text{for } Z_{ic} \geq z \geq Z_{st} \tag{A4.10}$$

$$V_{mb} = V_{stmb} \tag{A4.11}$$

$$V_{ic} = V_{stic} \tag{A4.12}$$

$$V_{mb} = V_{st} = V_{simb} + V_{stic} \qquad \text{for } 0 \geq z \geq Z_{st} \tag{A4.13}$$

where, V_{mb} is volume fraction of MB flow domain, V_{ic} is volume fraction of IC domain V_{stmb} is static macropore volume fraction of MB flow domain, V_{stic} is Static macropore volume fraction of IC domain, V_{stmb0} is static macropore volume fraction of MB flow domain at top, V_{stic0} is static macropore volume fraction of IC domain at top, V_{st} is total static macropore

volume, V_{mp} is total macropore volume fraction. When these are cumulated from depth 0 to z_{st}, the total volume fractions are obtained.

Horizontal distribution

In the horizontal plane the distribution of macropore determines the functional horizontal shape of the macropores, which forms the basis of the calculation of several important parameters. It is determined by effective matrix polygon diameter (d_{pol}).

$$d_{pol} = d_{p\min} + \left[\left(d_{p\max} - d_{p\min}\right)\left(1-M\right)\right] \quad \text{(A4.14)}$$

$$M = \left(V_{st} / V_{st0}\right) \qquad \text{for } V_{st0} > 0 \quad \text{(A4.15)}$$

$$M = \left(P_{ic} / P_{ic0}\right) \qquad \text{for } V_{st0} = 0 \text{ and } P_{ic0} > 0 \quad \text{(A4.16)}$$

$$M = 1-\left(Z / Z_{dp\max}\right) \qquad \text{if } 1-\left(z/Z_{dp\max}\right) > 0 \quad \text{(A4.17)}$$

$$M = 0 \qquad \text{otherwise}$$

$$d_{pol} = d_{p\max} \qquad \text{for } V_{st0} = 0 \text{ and } P_{ic0} = 0 \quad \text{(A4.18)}$$

where, M is relative macropore density, d_{pmin} is minimum polygon diameter, d_{pmax} is maximum polygon diameter, and Z_{dpmax} is depth of effective maximum polygon diameter. These parameters are obtained by dye tracer experiments on vertical soil columns. In this work, these parameters are picked up from the work of Das et al. (2014) which conducted dye tracer experiments in several sites in Northeast Indian region (Table 6.1).

A5. Preparation of saturated hydraulic conductivity map

Hydraulic conductivity (K) is defined as the ability of the water to pass through the pores of an aquifer. It is a governing factor in the sub-surface flow contribution in hilly watersheds. Back tracing K by the separation of surface runoff and sub-surface flow is a difficult task at watershed scale. Therefore, theoretical K map was derived from a conceptual method developed by Luo et al. (2010). The application of this method has also been extended for mapping of hypothetical K on the Martian surface (Luo et al., 2011). It derives the K as

$$K = (p \times i) \Big/ \left[D^2 (T^2 - (T-d)^2 \right] \quad \text{(A5.1)}$$

where, *p* and *i* are mean annual precipitation and infiltration proportion respectively, *D* is the drainage density, *T* is the perched aquifer thickness above the datum and *d* is the valley depth.

The rescaled SRTM DEM at 1 km was used for spatial scale compatibility of the model. However, average elevation (E_{avg}), minimum elevation (E_{min}), and total length of streams (L_T) within each micro-watershed were obtained from DEM at 90 m. For each micro-watershed, L_T was used with area (A=1km^2) in Eq.A5.2 (Horton,1932; 1945) to calculate *D* and the difference between E_{avg} and E_{min} produced *d* (Eq.A5.3). The conceptual diagram for the preparation of these maps is given in Fig. A5.1.

$$D = L_T / A \quad \text{(A5.2)}$$

$$d = E_{avg} - E_{min} \quad \text{(A5.3)}$$

Since, there is no information of aquifer thickness, a hypothetical value of T = 1m above (E_{avg} – soil matrix depth) was assumed from datum as E_{min} for each 1 km grid. Luo et al. (2010) used long-term mean annual precipitation data for *p* and observed *i* for derivation of *K*. But, the demand of this hydrological model is saturated hydraulic conductivity (K_{sat}) rather than a general *K* to calculate decay of the flow with time (Eq.6.5). It is assumed that the aquifers are close to saturated state in the rainy seasons having the value of *K* close to K_{sat} in the near-peak period of the season. Henceforth, long-term mean of daily precipitation intensity from GsMap data for the peak monsoon period (July – August) over 16 years (2001 – 2016) was used for calculating *p* in the study area.

The map of *i* for hillslopes should be inserted as a fraction of *p* to calculate *K* (Luo et al., 2010). Hence, the experimental work of Sarkar et al. (2015) which conducted hillslope experiments at 20% surface slope, sandy loam soil texture, and 37–70 mm/h of *K*, was used for defining spatial distribution of *i* (Fig. A5.1). Another experimental study conducted by Chen and Young (2006) concluded that the effect of slope on infiltration rate is applicable to a small time and this effect vanishes at prolonged time thereby making gravity as the dominant control mechanism. Since, the model resolution with daily scale intensity is much larger than what

most of the hillslope studies are focused on, the latter part of conclusion from Chen and Young (2006) is considered where effect of slope is negligible at large time. Consequently, observations from Sarkar et al. (2015) was used to characterize *i* according to a 2nd order polynomial fitted curve as shown in Fig. A5.1. All these modifications were incorporated into Eq. 6.1 to give it a final form (Eq. A5.3) and used for mapping the K_{sat}.

$$K_{sat} = \left(p_{\text{JUL-AUG}} \times i_F \right) \Big/ \left[D^2 \left(T^2 - (T-d)^2 \right) \right] \tag{A5.4}$$

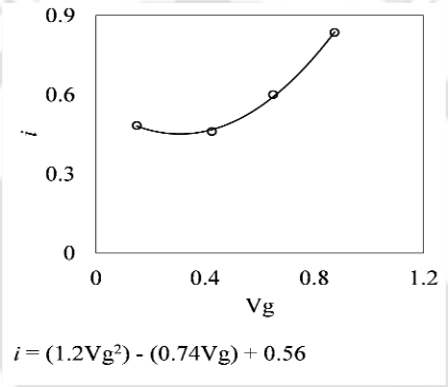

Figure A5.1. Spatial variation of infiltration proportion according to vegetation fraction modified from Sarkar et. al (2015).

List of publications from this thesis

List of Publications in Journals

1. Padhee, S.K., and Dutta, S., 2019, "Spatio-Temporal Reconstruction of MODIS NDVI by Regional Land Surface Phenology and Harmonic Analysis of Time-series", *GIScience & Remote Sensing*, 56(8), 1261-1288.

2. Padhee, S.K., and Dutta, S., 2020, "Spatiotemporal reconstruction of MODIS land surface temperature with the help of GLDAS product using kernel-based nonparametric data assimilation", *Journal of Applied Remote Sensing*, 14(1), 14520.

List of Publications in Conference Proceedings

1. Padhee, S.K., and Dutta, S., Estimation of evapotranspiration based on an extended three-temperature model and MODIS products in Arunachal Pradesh, India. National Conference on Emerging Technology Trends in Agricultural Engineering, *ETTAE 2014*, NERIST, Nirjuli (Itanagar), November 07 – 09, 2014.

2. Padhee, S.K., and Dutta, S., Estimation of evapotranspiration based on an Extended Three-Temperature Model and MODIS products in ecosystems of Northeast India. *HYDRO 2015 INTERNATIONAL*, 20th International Conference on Hydraulics, Water Resources and River Engineering, IIT Roorkee, India, December 17 – 19, 2015.

3. Padhee, S.K., and Dutta, S., Performance of 3T model to estimate Evapotranspiration after time and terrain correction in the Eastern Himalayas. National Symposium on Recent Advances in Remote Sensing and GIS with Special Emphasis on Mountain Ecosystems, *ISRS-2016*, Dehradun, India, December 7 – 9, 2016.

4. Padhee, S.K., and Dutta, S., Impact of terrain complexity on coarse solar radiation derivatives in Himalayan mountains: A hydrological perspective. *AGU Fall Meeting*, Washington DC, USA, December 10–14, 2018.

5. Padhee, S.K., and Dutta, S., Consistent Accessibility of Satellite-based Evapotranspiration Estimates in Himalayan Catchments. 16th Annual Meeting, *AOGS-2019*, Singapore, July 28 – August 3, 2019.

6. Padhee, S.K., and Dutta, S., Use of high-resolution satellite-based surface water budget for indications of preferential flow in the Eastern Himalayan Stretch. *AGU Fall Meeting*, San Fransisco, USA, December 07–11, 2020.